

Lappeenranta-Lahti University of Technology LUT  
School of Engineering Science  
Computational Engineering and Technical Physics  
Technical Physics

**Ha Ngan Ta**

**PROPERTIES OF Ni-Mn-Ga MAGNETIC SHAPE MEMORY ALLOY  
MANUFACTURED BY LASER POWDER BED FUSION**

Master's Thesis

Supervisors: Professor Kari Ullakko

Junior researcher Ville Laitinen

## **ABSTRACT**

Lappeenranta-Lahti University of Technology LUT  
School of Engineering Science  
Computational Engineering and Technical Physics  
Technical Physics

Ha Ngan Ta

### **Properties of Ni-Mn-Ga magnetic shape memory alloy manufactured by laser powder bed fusion**

Master's thesis

2021

64 pages, 38 figures, 4 tables and 2 appendices

Examiners: Professor Kari Ullakko  
Junior researcher Ville Laitinen

Keywords: Ni-Mn-Ga, magnetic shape memory, magnetically induced deformation, additive manufacturing, 4D printing, laser power bed fusion

In the category of smart materials, the magnetic shape memory alloy (MSMA) Ni-Mn-Ga has gained traction due to its giant strains of 6-10% when exposed to a magnetic field. This property makes the material a potential candidate for small-sized motion-producing devices in which conventional mechanisms fail to perform. Additive manufacturing (AM) has demonstrated novel ways of engineering with its ability to produce high-complexity shapes. Laser power bed fusion (L-PBF) is an AM method that bases on layer-by-layer melting of powder feedstock using a focused laser beam. Recently, this process has gained interest as a promising approach to manufacture Ni-Mn-Ga-based MSMA. The overall results from this process have been positive, although the built material requires considerable amount of post-processing, for example, by heat treatments. This thesis aimed to study the properties of the samples fabricated from Ni-Mn-Ga alloy by L-PBF. A set of Ni-Mn-Ga samples with slightly different compositions were built using L-PBF and subsequently heat treated. Several characterization methods were utilized to study the micro-structure and the MSM-related properties of the produced samples in both, as-built and heat-treated, conditions. The results confirmed what was already stated in the scientific literature; the built samples exhibited homogeneous chemical compositions, modulated martensitic crystal structures, and fully reversible martensitic transformations typical for the Ni-Mn-Ga alloys fabricated by L-PBF. Internal stresses, compositional variation, local variations of lattice parameters, and disordering were suggested as the reasons of low-quality properties in as-built samples. Heat treatment homogenized and stabilized the crystal structure as well as reduced internal stresses. Heat-treated samples possessed high-quality magnetic properties and diffraction spectrums; the grains appeared larger with long-range order. EDS experiment did not reveal composition gradients in the material. It was concluded that L-PBF was a reliable and repeatable manufacturing method for Ni-Mn-Ga MSMA.

## ACKNOWLEDGEMENTS

First, I would like to thank Professor Kari Ullakko for providing me this fascinating thesis topic about an interesting effect that he discovered with his colleagues. I express my deepest gratitude to Junior researcher Ville Laitinen, for the thorough guidance through the whole thesis work process. Ville's explanation is always easy to understand, and he is extremely patient with my rough schedule. I would also like to extend my thanks to Dr. Oleksii Sozinov, who demonstrated the operation of X-ray diffractometer, and to laboratory technician Toni Väkiparta for explaining and helping with SEM/EDS measurements. I am grateful to be friends with Veenavee and Mahsa, they have helped me a great deal academically and personally during the master's studies.

I have been working full-time alongside my master's studies and it would not be possible without the support from my colleagues. I thank Harri - my manager, and Danfoss Editron's large machine R&D team for providing an excellent working condition and all the needed arrangements to complete my studies as well as thesis work.

I would not be in this position today without my family and friends. My parents and brother have sacrificed tremendously and never stopped believing in me. My friends have made my life much easier with immense care and best advices. I am forever thankful for them.

Lastly, a massive appreciation goes to Dania, for being *simply the best* companion on this journey.

*Ha Ngan Ta*

Lappeenranta, December 2021

## TABLE OF CONTENTS

### ABSTRACT

### ACKNOWLEDGEMENTS

### TABLE OF CONTENTS

### LIST OF SYMBOLS AND ABBREVIATIONS

<b>1</b>	<b>INTRODUCTION .....</b>	<b>8</b>
1.1	Objectives and limitations .....	9
1.2	Research methods .....	9
<b>2</b>	<b>MAGNETIC SHAPE MEMORY ALLOYS AND NI-MN-GA.....</b>	<b>10</b>
2.1	History of Ni-Mn-Ga .....	10
2.2	Crystal structure of Ni-Mn-Ga.....	11
2.3	Magnetic shape memory effect and twinning.....	13
2.4	Applications .....	15
<b>3</b>	<b>LASER POWDER BED FUSION.....</b>	<b>16</b>
3.1	Workflow and working principle.....	16
3.2	Microstructure characteristics and defects.....	18
3.3	Main processing parameters .....	20
<b>4</b>	<b>ADDITIVE MANUFACTURING OF MAGNETIC SHAPE MEMORY ALLOYS</b>	
	<b>21</b>	
4.1	Latest results in AM of Ni-Mn-Ga .....	21
4.2	Material challenges .....	23
<b>5</b>	<b>METROLOGY.....</b>	<b>24</b>
5.1	Particle characterization.....	24
5.2	X-ray fluorescence .....	26
5.3	Low-field magnetic susceptibility .....	28
5.4	X-ray diffraction .....	28
5.5	Scanning electron microscopy .....	30
5.6	Energy-dispersive spectroscopy .....	33
<b>6</b>	<b>SAMPLE PREPARATION .....</b>	<b>34</b>
6.1	Ni-Mn-Ga powder.....	34
6.2	Manufacturing process.....	35

6.3	Surface finishing .....	39
6.4	Heat treatment .....	41
<b>7</b>	<b>RESULTS AND DISCUSSION .....</b>	<b>44</b>
7.1	XRF .....	44
7.2	LFMS .....	46
7.3	XRD .....	49
7.4	SEM .....	52
7.5	EDS .....	55
<b>8</b>	<b>CONCLUSIONS .....</b>	<b>57</b>
	<b>LIST OF REFERENCES .....</b>	<b>59</b>

#### **APPENDICES**

Appendix I: SEM images

Appendix II: EDS images

## LIST OF SYMBOLS AND ABBREVIATIONS

a, b, c	Lattice parameter ( $\text{\AA}$ , $1 \text{\AA} = 10^{-10} \text{ m}$ )
$\varepsilon$	Strain
AB	As-built
AM	Additive manufacturing
a.u.	Arbitrary unit
BE	Backscattered electron
CAD	Computer-aided design
CE	Circle equivalent
EDS	Energy-dispersive X-ray spectroscopy
Ga	Gallium
HT	Heat-treated
LFMS	Low-field magnetic susceptibility
L-PBF	Laser powder bed fusion
LUT	Lappeenranta-Lahti University of Technology
MFIS	Magnetic field induced strain
MIR	Magnetically induced reorientation
Mn	Manganese
MSM	Magnetic shape memory
MSMA	Magnetic shape memory alloy
Ni	Nickel
NM	Non-modulated
PE	Primary electron
PBF	Powder bed fusion
SE	Secondary electron
SEM	Scanning electron microscope
SMA	Shape memory alloy
S1	Sample 1 (corresponding to piece A1)
S2	Sample 2 (corresponding to piece A2)
S3	Sample 3 (corresponding to piece B3)
TB	Twin boundary

TEM	Transmission electron microscope
XRD	X-ray diffraction
XRF	X-ray fluorescence
2D	Two-dimensional
3D	Three-dimensional
4D	Four-dimensional
10M	Five-layered modulated martensite
14M	Seven-layered modulated martensite

## 1 INTRODUCTION

Ni-Mn-Ga-based magnetic shape memory alloys (MSMAs) produce strain when exposed to a magnetic field. This magnetic field-induced strain (MFIS) happens when sections of material in the martensitic phase are reoriented to minimize the stress induced by the magnetic field (Ullakko *et al.*, 1996). The strain is kept afterward even when the applied magnetic field is removed. The strain is reversed either when brought into another magnetic field perpendicular to the initial one, or by mechanical stress. With this characteristic, Ni-Mn-Ga is a promising material for actuating applications. Large MFIS has been observed mainly in single crystals; in polycrystals the strain is much lower. The reasons are weak texture (having crystals in different orientations), and that the aligning motion of small areas is inhibited by grain boundaries (Gaitzsch *et al.*, 2007) (Pötschke *et al.*, 2007). Improving the crystalline texture and reducing grain boundary restrictions allow polycrystalline Ni-Mn-Ga to exhibit MFIS of up to 4% in thermo-mechanically treated Ni-Mn-Ga alloy (Ullakko *et al.*, 2001), and 8.7% in polycrystalline Ni-Mn-Ga foams (Chmielus *et al.*, 2009).

Producing single crystals or polycrystalline Ni-Mn-Ga using the conventional methods is expensive and slow while having potential risks of elemental variation along the crystal axis and chemical segregation (Schlagel *et al.*, 2000). Hence, conventional manufacturing methods of polycrystalline Ni-Mn-Ga restricts the design freedom, which hinders the development of functional devices which employ the MSMAs. Contrarily, additive manufacturing (AM) is well known for its ability to build complex components at a relatively low cost, making it a promising approach to produce polycrystalline Ni-Mn-Ga MSMAs. Recent development of Ni-Mn-Ga built by AM reveals a giant fully reversible MFIS of 5.8% (Laitinen *et al.*, 2022). This strain is significantly larger than the previously reported strain of 0.01%, which could have been restricted by internal defects from the fabrication process, grain boundary limitations, and random orientations of crystals (Caputo, Matthew P. *et al.*, 2018).

### 1.1 Objectives and limitations

This thesis aimed to examine the properties of some MSMA Ni-Mn-Ga samples, which had been fabricated by L-PBF at LUT University. The goal was to provide information about the samples' compositions and corresponding mappings, microstructural features, and magnetic properties. Half of the specimens would be heat-treated, and their properties should be compared to the samples prior heat treatment. The study focused primarily on the chemical composition and microstructure.

The research questions were:

- What is the current research stage of Ni-Mn-Ga in general and regarding production by AM?
- What are the main elements and their amount presented in the manufactured samples?
- How were the alloying elements distributed?
- What are the magnetic properties of the specimens?
- What are the main differences in between the studied properties of as-built and heat-treated samples?

### 1.2 Research methods

The thesis contains two principal sections: literature review and experimental part. The literature review concentrates on introducing the basics of Ni-Mn-Ga and L-PBF as well as other AM methods for MSMA. The information is gathered from previous studies published in scientific articles and textbooks, provides necessary knowledge and supports the analyses of the experiments. The references are suggested by the supervisors, also from the university's library and other trusted databases. The reliability of the sources is taken into consideration.

The experiments may be conducted in no specific order due to the differences between surface quality and preparation requirements for each method, and the possibility of a sample getting damaged in any procedure should be considered when designing the experiments. Outputs of measurements are then collected and processed. Comparison, calculations may be employed to analyze the results and come to conclusions.

## 2 MAGNETIC SHAPE MEMORY ALLOYS AND NI-MN-GA

MSMAs belong to a group of smart materials. They are “smart” not in the sense that a material could gain intelligence, but rather exhibits changes in their properties in response to external stimulation. Smart materials can be utilized in some application to provide active feedback and increase its functionalities as well as capabilities, which cannot be achieved if made from normal materials. There are four categories of responses to external stimuli for smart materials:

- Actuator materials: produce strain upon applied stimuli.
- Energy conversion materials: convert external stimuli to another form of energy, such as a voltage, magnetic field or alter their temperature.
- Optical materials: change their optical properties or emit light when stimulated.
- State-changing materials: shift their physical characteristics as a response. (Laitinen *et al.*, 2020)

Shape memory alloys (SMAs) and MSMAs produce strain or motion in response to changes in temperature and magnetic field, respectively. The motion is mostly created by the material itself without other additional components as in a traditional mechanical system, making it a potential replacement in future application, where the number of components and friction are critical. These alloys are also capable of working in micro scale, such as in microelectromechanical systems, where conventional systems are not feasible or struggle to operate. SMAs and MSMAs are being actively investigated and developed, certain realizations have been achieved in term of properties and production.

### 2.1 History of Ni-Mn-Ga

Among MSMAs, Ni-Mn-Ga is the most investigated alloy, which is a composition of three elements Nickel, Manganese and Gallium. Kari Ullakko and colleagues observed the first MFIS (0.2%) in an Ni<sub>2</sub>MnGa sample in 1996, along the [001] plane while it was placed in a magnetic field of 8 kOe at -8°C (Ullakko *et al.*, 1996). 0.2% strain is the percentage of deformation to initial length. Figure 1 demonstrates the strain measurement, in which  $e_{\perp}$  and  $e_{\parallel}$  were the strain induced by the magnetic field when it was perpendicular and parallel to [001], respectively. The strain difference was calculated as  $e_{\perp} - e_{\parallel} \approx 0.2 \cdot 10^{-3}$ .

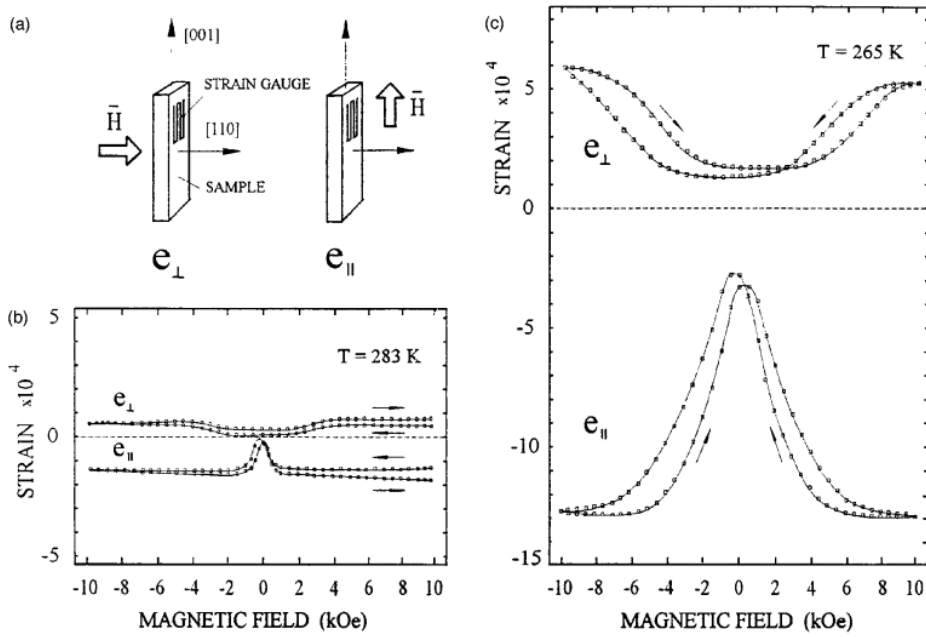


**Figure 1.** (a) Strain gauge and magnetic field in relative orientation to the sample, (b) the measurement results at the temperature of 283K, (c) measurement results at 265K (Ullakko *et al.*, 1996).

Since then, the straining effect, or magnetic shape memory (MSM) effect has gained certain interest and attention, especially in Ni-Mn-Ga alloys. Studies and research have been conducted to optimize its crystal structure to achieve maximum strain. Large MFIS of 6% has been observed in 10M martensitic structure of pure Ni-Mn-Ga (Murray *et al.*, 2000), and 9.5% in 14M martensitic structure (Sozinov *et al.*, 2002). These strains outdo values produced by other materials in the same class by approximately a hundred times, for example, up to 0.17% strain in Terfenol-D (Engdahl, 2000). Actuator application has shown no significant fatigue after  $200 \times 10^6$  cycles while providing a high efficiency of 95% (ratio of mechanical output to applied magnetic field energy) (Tellinen *et al.*, 2002). From a MFIS of 0.2% at  $-8^{\circ}\text{C}$  in the beginning, 9.5% has been reached at ambient temperature, suggesting a better possibility to integrate the material to normal systems.

## 2.2 Crystal structure of Ni-Mn-Ga

Ni-Mn-Ga is a Heusler magnetic intermetallic compound with a composition in the form of  $X_2YZ$  corresponding to full-Heusler, where elements X and Y represent transition metals

and element Z is in the groups 13 to 18 of the periodic table. In liquid state, stoichiometric (having exact element proportions) Ni<sub>2</sub>MnGa presents in a disordered cubic B2' structure (Overholser, Wuttig and Neumann, 1999). When cooling to room temperature, it undergoes phase transition to a highly ordered cubic L2<sub>1</sub> structure (austenite) (figure 2) (Webster *et al.*, 1984). The lattice constant of a unit cell in this phase is approximately 5.82 Å, all three parameters a, b, and c are equal due to cubic form. Atoms of Ga (green) locate at the corners of the cell and the center of each face, atoms of Mn (pink) situate at the center of the cell as well as each edge. This arrangement divides the cell into eight sub-cells, of which centers are Ni atoms (orange).

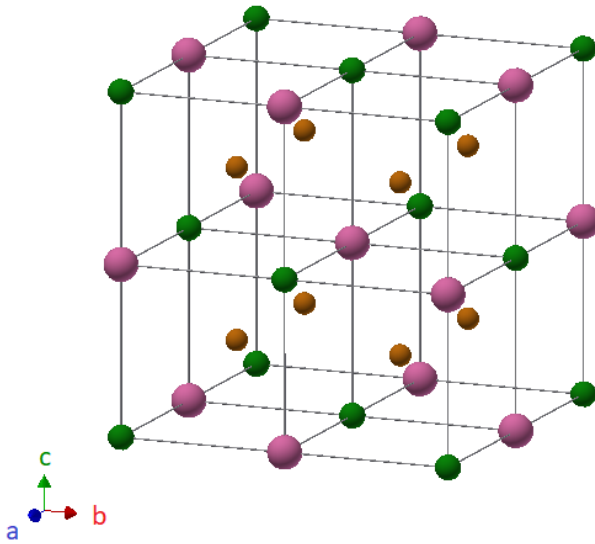


**Figure 2.** Face-centered cubic structure of Ni-Mn-Ga in austenitic phase, green – Ga, pink – Mn, orange - Ni.

With further cooling, the structure transforms to martensite phase and the cubic cell structure's symmetry decreases by changes in lattice parameters (Webster *et al.*, 1984). Martensitic phase is where the MSM effect is observed and thus the focus to this material. Chemical composition heavily influences the material's phase transformation temperature and crystal structure. Slightly off stoichiometric element proportion leads to martensitic transformation happening at -113°C to 177°C, including ambient temperature which is desirable for potential applications to operate (Vasil'ev *et al.*, 1999). Ni-Mn-Ga with different compositions in martensitic phases have been observed in three general crystal structures (Pons *et al.*, 2000) (Aaltio *et al.*, 2016). They are non-modulated martensite - NM, five-layered modulated martensite - 5M (or 10M), and seven-layered modulated martensite - 7M (or 14M). Their crystallographic structure parameters are often interpreted according

to the coordinate system of the austenitic phase. All martensitic structures were studied by (Martynov, 1995) regarding crystal arrangement, lattice parameters and modulation type. In (Martynov and Kokorin, 1992) the crystal structures were depicted as repetition of atomic positions. In this thesis work, the modulation structure is viewed as repeated arrangement of tightly packed planes: five-layered modulated martensite is denoted as 10M and seven-layered modulated martensite is denoted as 14M (Pons *et al.*, 2000). Figure 3 shows the crystal systems for three martensitic structures. NM Ni-Mn-Ga has a tetragonal cell structure without modulation and  $a = b, c > a$ . 10M structure is monoclinic with  $a \approx b, c < a, \gamma > 90^\circ$ , and 14M structure is orthorhombic with  $a > b > c, \gamma > 90^\circ$ .

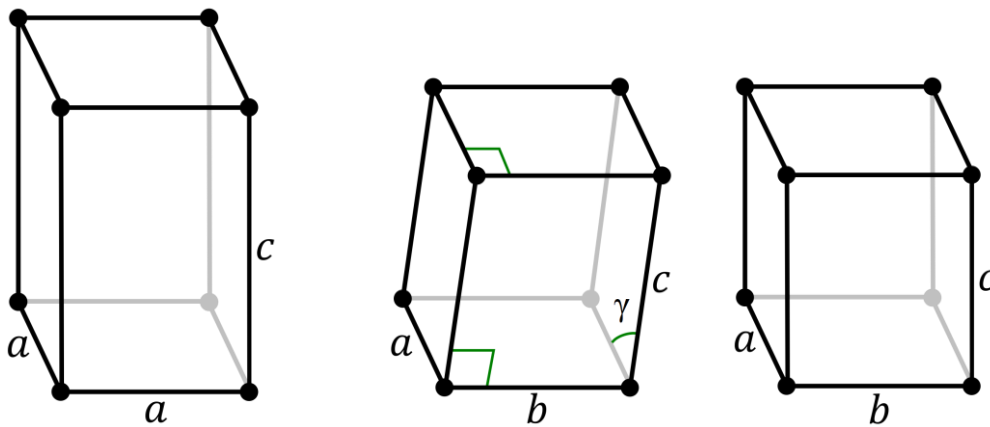


**Figure 3.** Crystal systems. From left to right: tetragonal, monoclinic, orthorhombic. (Mayer Daniel, 2007)

Upon heating, Ni-Mn-Ga's phase transforms in reverse, from martensite to austenite. Its cell structure converts to cubic form and the material's overall shape changes so technically, this alloy is also a thermally activated shape memory alloy. However, this effect is not the focus of the thesis thus not discussed further.

### 2.3 Magnetic shape memory effect and twinning

MSM effect works based on the magnetically induced reorientation (MIR) mechanism, which rearranges crystal lattices by moving twin boundaries (TBs) (Ullakko *et al.*, 1996) (Likhachev and Ullakko, 2000). The MSM material is made up of small patches with different structure and magnetic orientation, represented in gray and purple areas in figure 4. Crystal twinning is the situation when two separate crystals, called twin variants, share some atoms and appear highly symmetrical around those atoms. The boundary between them is TB. Individual atoms can move a distance which is smaller than the space between atoms

in the crystal structure. When a magnetic field  $H$  is introduced, one twin with preferred orientation grows to match the field direction, oppresses the other twin and causes TB to move. This TB motion changes the overall shape of the specimen. When the sample is saturated with the magnetic field, all preferably oriented twins align with the direction of the magnetic field, the force exerted on TBs is maximized and maximum strain is reached (Saren *et al.*, 2016).

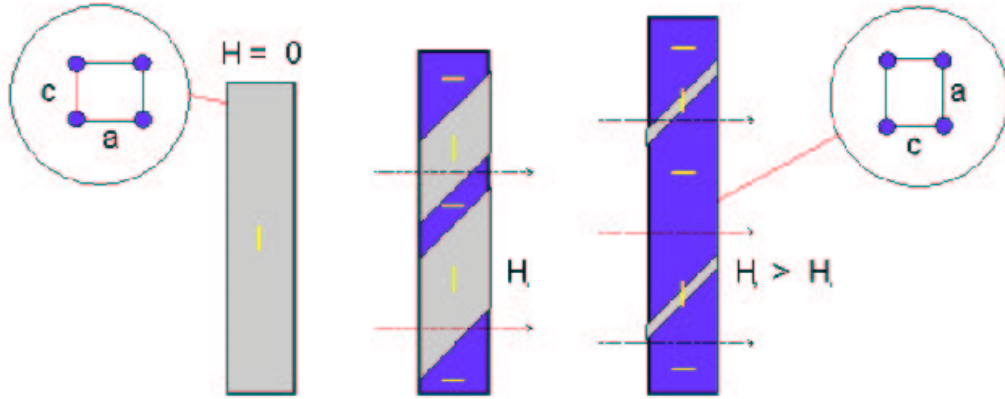


**Figure 4.** Schematic presentation of MIR mechanism. (Tellinen *et al.*, 2002)

The insets in figure 4 illustrate one unit cell of the twin variants. The left one has the shorter side  $c$  parallel to the specimen's elongating direction, and the right one has  $c$ -axis placed perpendicularly.  $c$ -axis is the easy side to align with magnetization direction, as shown with the purple variant. The maximum strain  $\varepsilon$  that could be theoretically obtained from a martensitic crystal structure is calculated as:

$$\varepsilon = 1 - \frac{c}{a} \quad (1)$$

In which  $c$  and  $a$  are the cell's lattice constraints in martensitic structure (Söderberg *et al.*, 2005). For a Ni-Mn-Ga alloy to exhibit MFIS, there are two main requirements. First, at operating temperature, the material must be in martensitic structure and exhibit microstructural twins (Ullakko *et al.*, 1996) (Straka *et al.*, 2011). Second, the alloy's magnetic anisotropy must be greater than the energy necessary to move the TB (Ullakko, 1996).

## 2.4 Applications

MSMAs are beneficial in applications which traditional machinery would be impossible to service:

- Micro-pump delivering micro-liter of medicine: this takes advantage of the alloy's size adaptability and the ability to operate without electricity nor the conventional motor unit (*Boise State Micro-Pump Aids Neurological Research*. 2014).
- Actuator, which takes advantage of the MSMA's potential to work with high frequency (rise time less than 0.2 ms) driven by magnetic field while experiencing low fatigue (no considerable change even after  $200 \times 10^6$  cycles). A relatively large force can be generated from this actuator as well. (Tellinen *et al.*, 2002)
- Strain sensor, which employs the magnetization-strain ratio of Ni-Mn-Ga. Reversible strains can be induced in the material while causing minimal stress, making it a potential mechanism for sensing application. (Stephan *et al.*, 2011) (Hobza *et al.*, 2018)
- Energy harvester, which converts strain to voltage to power a small load (Suorsa *et al.*, 2004) (Karaman *et al.*, 2007).
- Vibration energy harvester using vibration to produce a small amount of electrical energy (Saren *et al.*, 2015).

### 3 LASER POWDER BED FUSION

Additive manufacturing (AM) is a manufacturing method in which an object is created from the base upward by adding layers of material, as opposed to other subtractive or formative processes in which material is removed or deformed to create a part. Because of the layering principle, AM is commercially known as three-dimensional (3D) printing. AM provides tremendous advantages in prototyping and customization, as it can deal with models of high complexity and containing interlocking components while producing less waste and decreasing costs. AM has grown rapidly since its first concept and is now a powerful tool in different industries. A wide range of materials is compatible with this manufacturing method, from plastics to metals, concrete, or wood-based composites. The resolution scope is also broad, making AM suitable for many application sizes, for example, machine components or building houses. Due to these strengths, AM is certainly an essential part of developing smart materials and their applications. In addition to the three dimensions of printing environment, smart materials have their own transitional dimension when stimulated, thus AM of this material group is sometimes referred as 4D printing.

Power bed fusion (PBF) is an AM process in which material powders are spread on a bed and selective regions are fused by a focused energy source. Laser powder bed fusion (L-PBF), also known as selective laser melting, utilize high-power laser as the energy source. In this chapter, L-PBF is discussed in regard to the production of metal parts; other powder materials are not focused.

#### 3.1 Workflow and working principle

An AM workflow generally consists of three steps, described in figure 5. First, the 3D model of the to-be-printed part is constructed in a computer-aided design (CAD) program. Then, the model is sliced into layers with optimum thickness. Support structures for overhang details are generated if certain angle is exceeded (figure 6). Finally, the AM system fabricates the part layer by layer according to the layer specification in step 2. The built object can be further processed to achieve final shape by cleaning or polishing, for example, to remove support elements or to get precise dimensions.



**Figure 5.** Three main steps of an AM workflow (*3D Printing: The Internal Process and Development*. 2019).

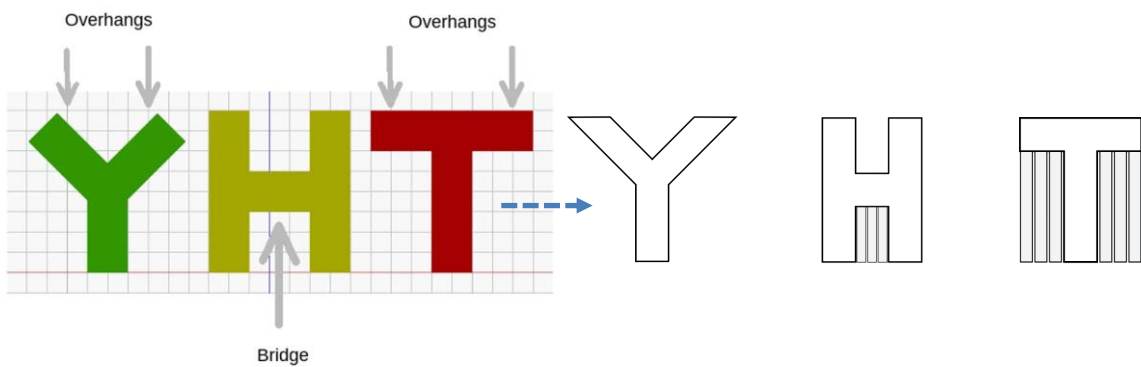


**Figure 6.** Schematic illustrations of overhangs and support structures in AM (*Supports in 3D Printing: A technology overview*. ).

Figure 7 presents the main components of a L-PBF system, in which a laser beam is used as the thermal energy source to fuse the powder material. Both the powder supply base and the build platform are adjustable in vertical direction, the same direction which the object is built along. The build chamber is shielded with a constant flow of an inert gas (argon or nitrogen) to prevent the oxidation of melted metal material and aid its vaporization. Raw powder is stored in the new powder stock cavity on the left. For each layer, the build platform moves downward a distance which is the same as layer thickness, and the supply cavity raises to provide powder. This amount of powder builds up in front of the coater, which then moves toward the build chamber and spread the new powder evenly on the top of the build chamber. Laser is then focused onto this layer and scans the cross section determined by the slicing program. The powder in the scanned track is fused together as well as merged to the previous

layer. Here one layer is completed. The process repeats for the next layers, fabricating the component from the bottom up.

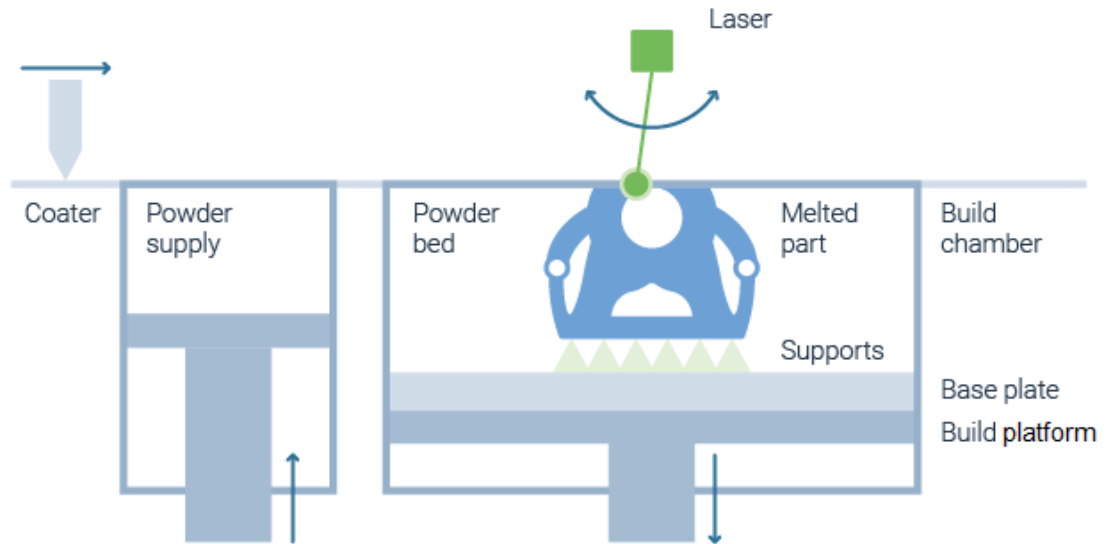


**Figure 7.** Main components of a PBF system (*Laser Beam Powder Bed Fusion - AMPOWER Report. 2019*).

When finished, the part is completely buried in the powders, thus after being removed from the powder bed it needs to be cleaned off excess powder. The remaining powder, which is unaffected by laser's heat, is reusable after filtering.

### 3.2 Microstructure characteristics and defects

Columnar grains are long and thin rod-like structures. When melted material is deposited on the previous layer which gets partly melted again, the grain grows along the direction of cooling and solidification (Thijs *et al.*, 2013). In a layer-by-layer AM process, heat from the melt pool is mainly transferred to the layers underneath and then to the build platform (Roberts *et al.*, 2009). This vertical heat transfer makes parts manufactured by L-PBF exhibit a texture of columnar grain structure roughly along the build direction. Figure 8 demonstrates the columnar structure in Inconel alloy 718 built by L-PBF.

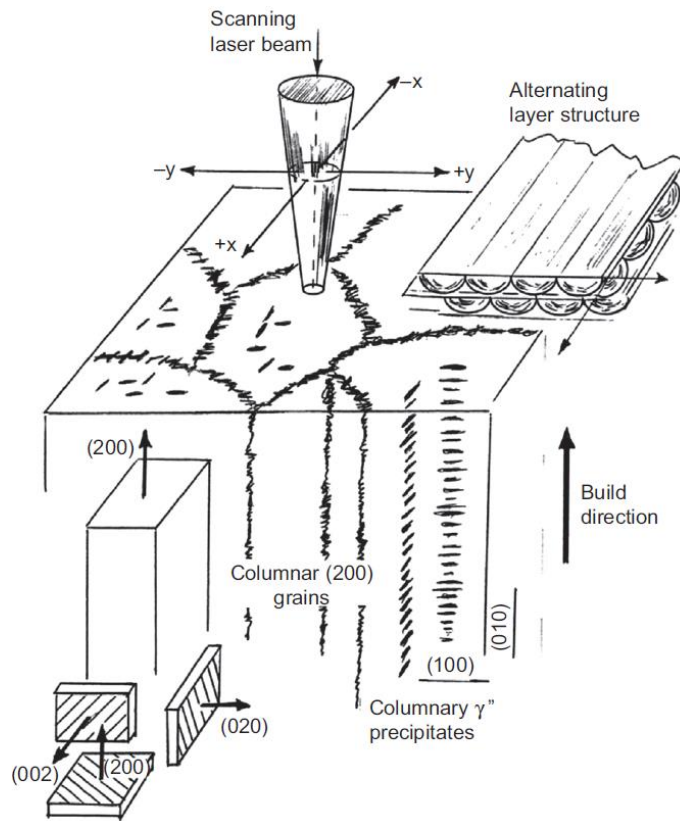


**Figure 8.** Columnar grain structure in Inconel 718 alloy manufactured by selective laser melting (Amato *et al.*, 2012).

Defects are often generated in components manufactured by L-PBF from various sources present in the fabricating setup, they affect the shape and properties of the result. Due to the typical working principle of L-PBF, residual stress is formed in the built part by large thermal gradient under directed thermal source and frequent thermal expansion and contraction from repeated heating and cooling (Merzelis and Kruth, 2006). Expansion and contraction of the melt pool restricted by the solidified layers onto which they are deposited are another contribution to residual stress (Vrancken *et al.*, 2014). Residual stresses lead to structural problems in the finished part, such as cracking and delamination (Kempen *et al.*, 2014). Part's overall shape can also be deviated from original design when experienced residual stresses (Li, Liu and Guo, 2016). Presence of oxygen in the build chamber causes oxidation of melted metals forming regions of oxide which induce defect and porosity (Louvis, Fox and Sutcliffe, 2011).

### 3.3 Main processing parameters

Figure 9 lists the processing parameters in L-PBF according to groups. Processing parameters play significant roles in manipulating properties of fabricated parts. Undesirable defects are minimized by optimizing one or several variables. Lower scanning speed and preheated build platform decrease cracking (Sonawane *et al.*, 2021). Residual stress can be decreased by employing checkerboard scanning style or homogenized by applying a rotating scanning pattern (Kruth *et al.*, 2012) (Vrancken *et al.*, 2014). Laser scanning speed influences the porosity of the built part, which is inverse to the part's density (Qiu, Adkins and Attallah, 2013). Furthermore, parameters such as laser power and laser exposure time affect the heat dissipation and grain growth (Vecchiato *et al.*, 2020).

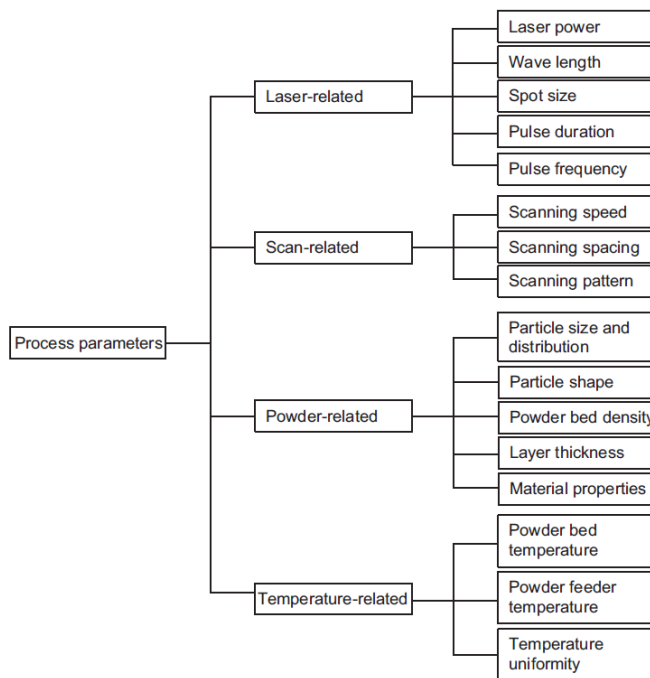


**Figure 9.** Categorized process parameters of L-PBF (Aboulkhair *et al.*, 2014).

In addition, characteristics of initial powder have important effect on the manufacturability. Spherical particles are beneficial for the powder spreading by re-coater between layers. Spherical shape makes flowability better while non-spherical shape impedes the flow by mechanical locking between particles and high friction. A range of particle sizes is preferred over homogeneous morphology, the gaps between large particles can be filled with smaller one, creating a denser packed and even powder layer. Evenly distributed powder layer is favorable for uniform heat conduction.

## 4 ADDITIVE MANUFACTURING OF MAGNETIC SHAPE MEMORY ALLOYS

AM is categorized into seven methods, of which four have been used for metal based SMAs and MSMAs. The processes and their definitions, according to the standard SFS-EN ISO/ASTM 52900:2017, are:

- Binder jetting: An AM process in which specific regions of powder material are glued together by liquid bonding agent.
- Directed energy deposition: An AM process in which a high thermal energy source, such as plasma arc or electron beam is used to fuse material as it is simultaneously fed into the melting pool, similar to arc welding.
- Material extrusion: An AM process in which molten material is deposited onto the substrates through a nozzle, similar to piping a cake.
- Powder bed fusion (PBF): An AM process in which material powders are spread on a bed and selective regions are fused by a focused energy source. This process is described in detail in the previous chapter.

Conventionally, monocrystalline Ni-Mn-Ga is grown by crystal growth techniques such as Bridgman–Stockbarger or Czochralski. These techniques are time-consuming and inefficient. Hence, polycrystalline Ni-Mn-Ga rose in popularity because it is technologically easier to fabricate. Additive manufacturing alternatives have attracted interest for building the polycrystals due to being cost-effective while enabling high geometrical freedom. 3D ink-printing (material extrusion with additional binder) and binder jetting methods have proved feasibility to fabricate these alloys (Taylor, Shah and Dunand, 2017) (Mostafaei *et al.*, 2017). Additionally, directed energy deposition has shown potential in fusing Ni-Co-Mn-Sn, a magnetocaloric material (Stevens *et al.*, 2016). L-PBF was a possible approach, although literature regarding this process has been limited. Since 2018, laser powder bed fusion (L-PBF) has been investigated at LUT University for possibility of printing polycrystalline Ni-Mn-Ga.

### 4.1 Latest results in AM of Ni-Mn-Ga

Ni-Mn-Ga has been manufactured using binder jetting method (Caputo, Matthew and Solomon, 2017). Pore density and distribution are reduced as sintering time increases.

Elemental proportions appear to vary in different sintering time settings. It proves that the chemical composition and porosity can be controlled by the process parameters. However, sintering regimes cause Mn to evaporate and oxidation to the elements. Additionally, it is difficult to consistently remove the binder from the built part. These challenges deviate the overall composition as well as microstructure of the material. A reversible MFIS of merely 0.01% was observed in sintered Ni-Mn-Ga, it is insignificant compared to the recently achieved strain in L-PBF manufactured Ni-Mn-Ga, but anyhow addressed the obstacles with AM and demonstrated that AM is a viable technique (Caputo *et al.*, 2018) (Laitinen *et al.*, 2022).

Another notable AM process for Ni-Mn-Ga manufacture is 3D ink printing. 3D ink printing was done in the material extrusion system, with the different of extruded material. Elemental powders were mixed with binder into a slurry ink form; then after building, the binder was burned off, and elements were diffused and homogenized. Micro-trusses have been fabricated using 3D-printing of liquid ink containing three elemental powders and binder (Taylor, Shah and Dunand, 2017). Similar to binder jetting, it is possible to control porosity in the created samples. Large grain growth was realized after sintering for 12 hours, and first-order phase transformation happened between 45°C and 90°C.

By eliminating the use of binder and reducing effects of remarked constraints, novel investigation in manufacture by L-PBF has demonstrated a giant fully reversible MFIS of 5.8% in 10M polycrystalline Ni-Mn-Ga at room temperature (Laitinen *et al.*, 2022). Evaporation of Mn was precisely manipulated by process parameters during the build process, which in turn affected the chemical composition and microstructure of the built material. Mn loss was also considered when preparing the pre-alloyed powder. The samples were built in thin wall-like shape to minimize residual stresses. Heat treatment improved the compositional homogeneity and further lowered residual stresses. A large single grain of sizes in millimeters was separated from the sample, which demonstrated a MFIS of 5.8%, comparable with strain achieved in monocrystalline 10M Ni-Mn-Ga grown by a conventional technique (Murray *et al.*, 2000). Without grain boundary restriction, the TBs could move freely and subsequently exhibit a large strain. The outcome was promising for future development of functional Ni-Mn-Ga-based MSM devices manufactured by AM.

#### 4.2 Material challenges

MFIS in Ni-Mn-Ga MSMA is heavily dependent on the chemical composition and crystal structure (Lanska *et al.*, 2004) (Jin *et al.*, 2002) (Overholser, Wuttig and Neumann, 1999). Loss of Mn is expected in L-PBF process because Mn has low boiling temperature and high vapor pressure, making it evaporate more easily than the other two elements. Mn loss has been observed in earlier processes, which was affected by process parameters (Laitinen, Salminen and Ullakko, 2019) (Laitinen *et al.*, 2019). Testing of initial composition and calculations of processing parameters are needed to take Mn losses into account. Oxidation and potential contamination in the build space could generate defects into the built part, thus should be minimized.

## 5 METROLOGY

To examine the samples' properties, several measurement methods have been utilized, which are:

- X-ray fluorescence (XRF)
- Low-field magnetic susceptibility (LFMS)
- X-ray diffraction (XRD)
- Scanning electron microscopy (SEM)
- Energy-dispersive spectroscopy (EDS)

In this chapter, each method's working principle and usage are explained briefly. Material properties which were studied include chemical composition and distribution, crystallographic information, phase transformation and micro images of twin boundaries.

### 5.1 Particle characterization

Particle characterization is the determination of a particle's morphological parameters, including circle equivalent (CE) diameter, circularity, elongation, and both volume and number particle size distributions. A three-dimensional sample is placed on a microscope cell in the XY plane and scanned to a two-dimensional digital image in a static image analysis technique. The digitized image is then processed by algorithms, which are capable of recognizing thousands of particles' perimeters within minutes. The perimeters are useful for calculating different size and shape parameters, and further classifying the particles' shape characteristics.

A particle's two-dimensional (2D) perimeter is used to integrate its area, then convert to an equivalent circle of the same area. CE diameter is defined as the diameter of the converted circle (figure 10). It is practical that the particle is represented by a single CE value in further processes such as counting and categorizing.

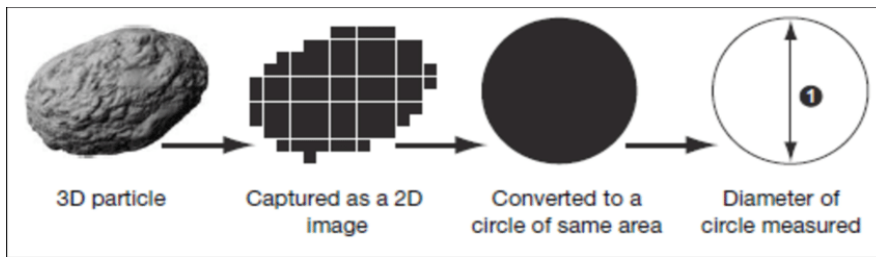


**Figure 10.** Definition of a CE diameter (Luke and Silva, January 1, 2013).

When a sample contains a statistically significant quantity (tens of thousands) of particles, statistical methods are applied to evaluate the particle size distribution. Statistics of the distribution are represented by derived diameter  $D[m,n]$ , in which  $m$  is the number of distribution and  $n$  stands for a certain percentile. The standard percentiles read from a characterization software are  $D[v, 0.1]$ ,  $D[v, 0.5]$ , and  $D[v, 0.9]$ . The percentile value 0.1 refers to a percentage of 10%, meaning that 10% of the observations in the distribution fall below the corresponding diameter. The similar explanations to 0.5 and 0.9 percentiles. Particle size distribution is calculated based on either number basis or volume basis. In the former, each particle's contribution is considered the same in the statistics regardless of its size. This method presents particle size information with higher resolution, especially with finer particles. Volume basis, on the other hand, weighs in the individual's size by a factor, meaning that the larger a particle is, the more it contributes to the statistics. Figure 11 illustrates the difference of the distribution graph between number based and volume-based consideration. It could be observed that the number-based distribution demonstrates all sizes equally while the volume-based distribution is biased toward larger particle sizes.

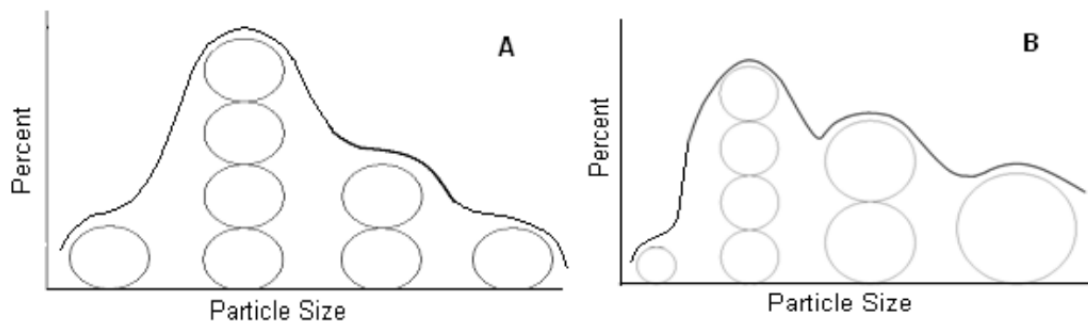
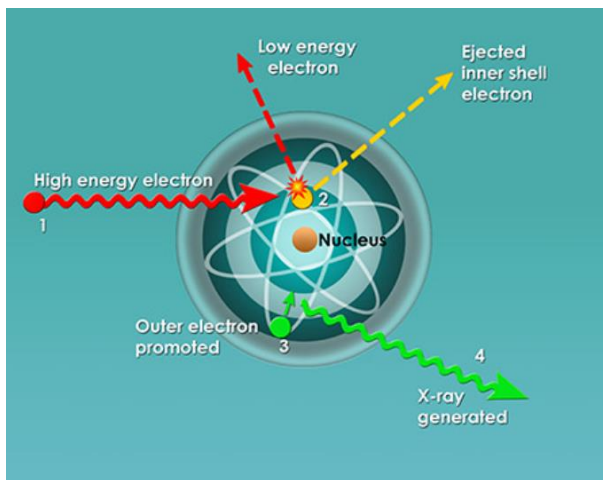


**Figure 11.** Difference of number-based distribution (A) and volume-based distribution (B) statistics (Luke and Silva, January 1, 2013).

Circularity shows how close a particle's 2D shape is to a circle. It is defined as the ratio of the equivalent circle's perimeter to the actual 2D shape's perimeter. Circularity values range from 0 to 1, with 1 as perfectly spherical and 0 as rough shape. Elongation measures how long a particle is in comparison with its width. It ranges from 0 to 1, with a sphere having a value of 0 while a slender shape has value closer to 1.

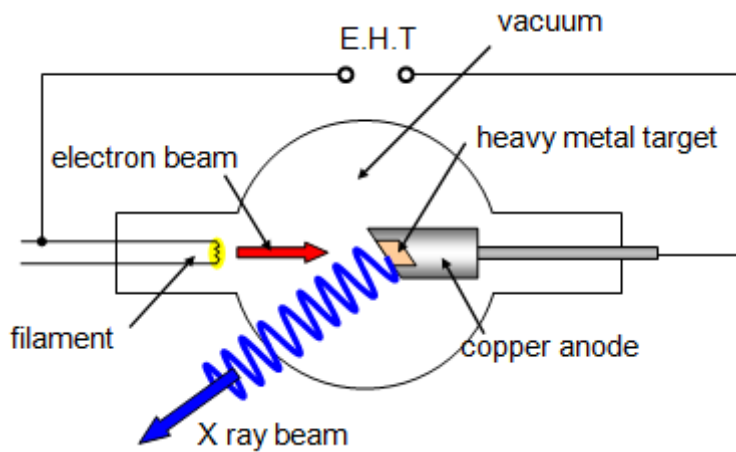
## 5.2 X-ray fluorescence

Fluorescent (or secondary) X-rays are emitted during ionization by a material when it is bombarded with high-energy short-wavelength X-rays or gamma rays. Figure 12 describes the emission of fluorescent X-ray from an atom. Incoming x-rays or gamma rays carry high energy, expel an electron located in the atom's inner shell, leaving a hole behind. The atom's electronic structure becomes unstable, so another electron in outer shell falls into the inner shell and fills the left hole. Because the lower orbitals have lower energy than higher ones, when falling, the electron releases a photon which carries an energy equal to the orbitals' gap. This emitted radiation represents the atom's characteristics and by collecting it, the material's chemical composition can be analyzed with high precision.



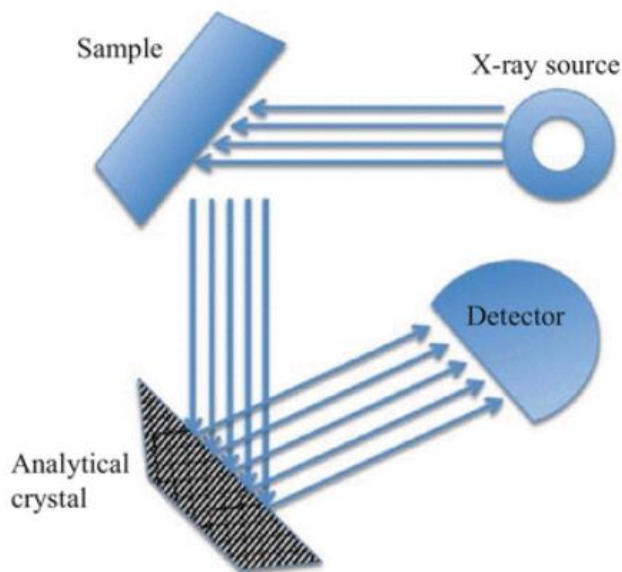
**Figure 12.** X-ray generation (Lloyd-Jones Graham, 2016).

Figure 13 presents the main components of an X-ray tube, where the X-rays are produced for an X-ray fluorescence spectrometer. A high-speed electron beam is ejected from the high temperature filament within a vacuum and travels toward the positive anode. A heavy metal target, usually tungsten, is mounted in the middle of the anode. When being struck by the electron beam, it emits an x-ray beam, which is then directed to the specimen.



**Figure 13.** Main components of an X-ray tube (*X-Ray Generator*2017).

Before reaching the detector, the radiation spectrum is improved by an integrated analytical crystal (figure 14). The crystal diffracts emitted X-rays following Bragg model of diffraction (equation 2), facilitating differentiation of the rays which improves the accuracy of the spectrum's peak.



**Figure 14.** XRF spectrometer's simplified structure (Nasrazadani and Hassani,2016).

Brag's equation:

$$n\lambda = 2d_{hkl}\sin\theta \quad (2)$$

In which:

- n: order of diffraction
- $\lambda$ : wavelength of the X-ray source

- $d$ : distance between planes in the crystal, with subscripts  $h, k, l$  representing their orientation according to Miller indices.
- $\theta$ : a half of the angle formed between the incidence beam and the diffraction beam.

Plane spacing  $d$  and diffraction angle  $\theta$  vary among different crystal materials, allowing detection and measurement of all materials at any concentration. Thus, contained elements in the material, even ones with low concentrations, can be quantified with high accuracy. After diffraction, the rays are collected at the detector for further process. A wavelength dispersive spectrometer handles the X-rays' wavelengths and can be set up to analyze certain elements' emission of interest.

At LUT University's Material Physics Laboratory, an Oxford Instruments X-Strata 960 XRF spectrometer with a 300- $\mu\text{m}$  collimator was utilized to determine the composition of both initial powder and as-built samples. It provides an accuracy of  $\pm 0.3$  atomic%. Before each measurement session, a Ni-Mn-Ga reference piece with determined composition was used to calibrate the device.

### 5.3 Low-field magnetic susceptibility

In LFMS experiment, a sample is heated up with controlled temperature and its phase is recorded in an in-house developed system. The values could be plotted and the phase transformation as well as Curie temperature could be observed from the plot.

### 5.4 X-ray diffraction

X-ray diffractometer is a robust and flexible device to study materials. It analyzes different properties of the material, such as physical properties, chemical contents, or crystallographic information (crystal orientations, defects, etc.). In this thesis work, an x-ray diffractometer was used mainly to identify phases presented in each sample.

A system of periodically arranged atoms form a crystal. At the center of an atom is a nucleus, which is surrounded by a cloud of electrons. Due to elastic scattering, when an atom is shot by an X-ray, it emits another X-ray carrying the same energy, only the direction is different. A crystal's arranged atom pattern makes it possible to work as a diffraction grating for electromagnetic radiation of a wavelength comparable to the distance between atoms, which

makes X-ray a good fit to observe this small spacing. Distinct planes of atoms can be observed due to the atoms' periodic pattern. Figure 15 demonstrates the cross-sections of two planes, whose distance is  $d$ . At a certain angle  $\theta$ , the reflected X-rays from those planes form constructive interference, strongly amplify the rays' intensity and fulfil Bragg's equation (equation 2). The atomic structure of a crystal can be calculated by detecting the emitted X-ray and measuring the incidence angle with the original wavelength. The intensity of the diffracted X-rays is measured, as well as the incident angle, to determine the atomic structure of a crystal.

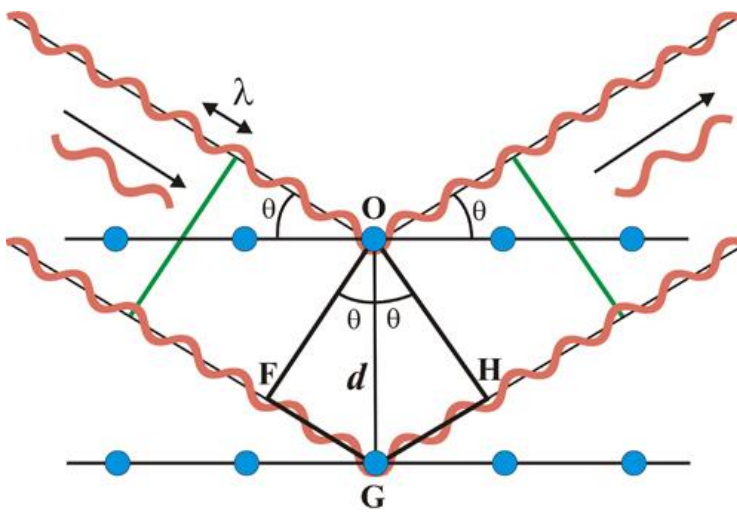


**Figure 15.** Constructive interference (Ripoll Martín Martínez, ).

From the Bragg's equation, a crystal can be studied in different ways by varying one of the variables and fixing the rest. In this thesis,  $n$ ,  $\lambda$ , and  $d$  are given while  $\theta$  varies. The examined crystal is fixed on the stage and targeted by a monochromatic X-ray. The focus remains at one spot while the beam rotates on a plane perpendicular to the crystal's surface. At certain  $\theta$  value which satisfies equation 1, scattering can be observed, visually by a spike in intensity. After the spectrum is recorded at pre-set  $\theta$  angles, combining with phase calculations, Miller indices  $h, k, l$  can be assigned to peaks.

Figure 16 describes the main components of an X-ray diffractometer. At LUT's material physics laboratory, a PANalytical Empyrean 3 multipurpose diffractometer is put to work with poly-capillary optics, a Cu tube generating a 0.15406-nm X-ray and a PIXcel3D-Medipix3 detector. The studied crystal is mounted on a non-diffraction single crystal Si-510 zero background holder. The generator is supplied with a 40-kV voltage and a 30-mA

current.  $2\theta$  angle varies from  $20^\circ$  to  $100^\circ$ . Each sample was scanned twice: the first test run with 2 seconds per step to confirm that the measurement happens as expected, and the precise run with much longer time per step (120 seconds) to minimize noise in the collected spectrum.

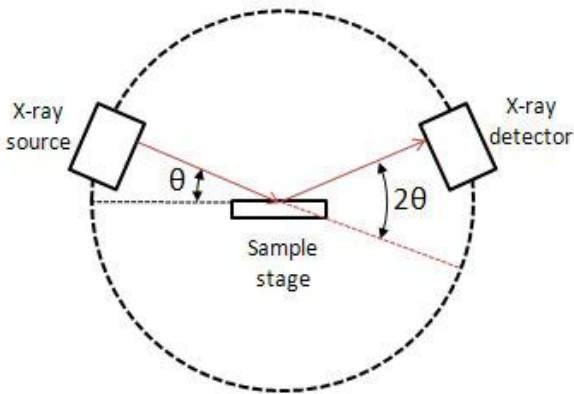


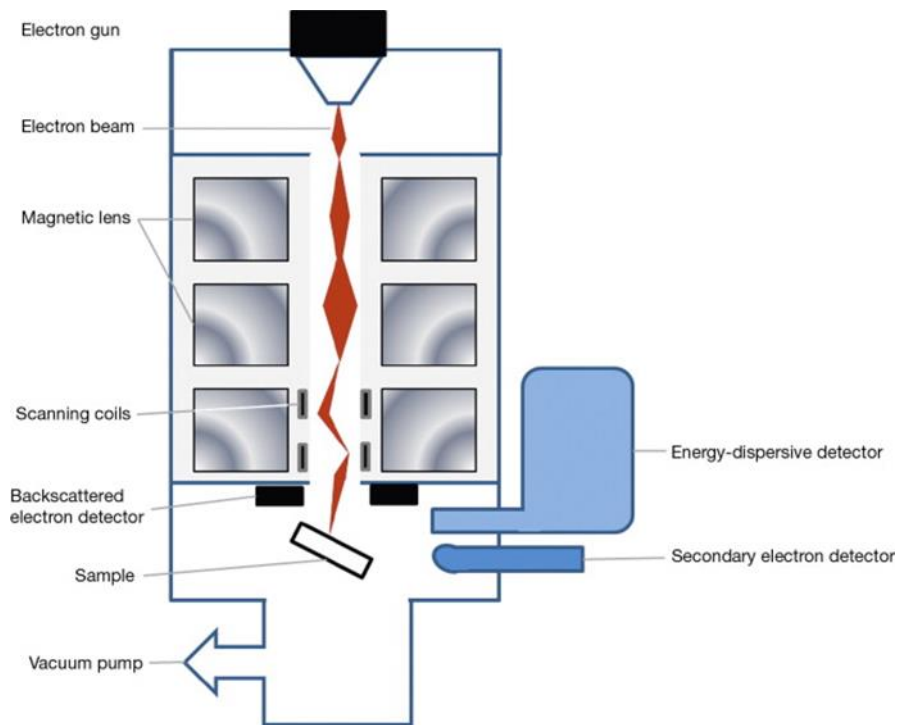
**Figure 16.** Schematic construction of an X-ray diffractometer ('X-Ray diffractometer and its various component parts for X-Ray studies', 2016).

### 5.5 Scanning electron microscopy

Electron microscopy magnifies sample by utilizing an electron beam. The beam travels across the sample's surface then creates an enhanced image from the scan. SEM offers many advantages including high magnification – 500 000 times and a resolving power of down to 1nm because the electron has much shorter wavelength than of visible light photons. The microscope can also be equipped with various attachment for analytical imaging or detecting chemical composition.

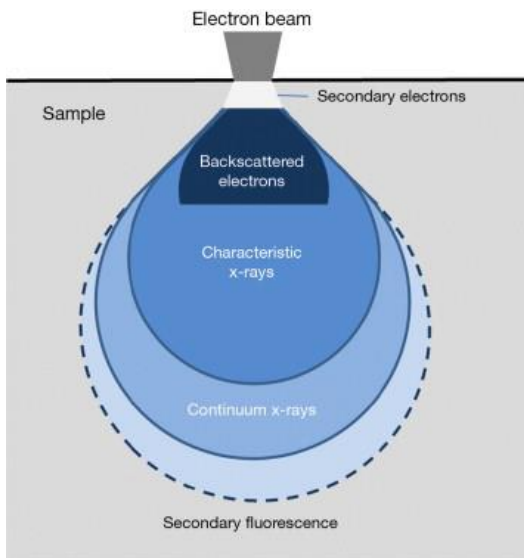
The electron beam is generated by applying a high voltage (up to 300kV) to heat up a filament, which is usually made of tungsten due to its high melting point. Electrons are emitted from the filament when the thermal energy exceeds the work function of the material. Magnetic lenses are then used to form the electrons into a beam before it is guided to the sample surface. The electrons are negatively charged and can build up on the sample's surface affecting the scanning results, so the sample must be conductive or grounded properly. Air molecules can deflect electrons, so the experiment must be set in vacuum. Unlike visible-light microscopy, SEM images are grayscale.

Figure 17 illustrates the components of a typical SEM setup and the electron beam's path. The condenser lenses focus the electron beam to a spot of size in nanometers on the sample's surface. The beam scans the surface in a raster by using scanning coils to deflect the beam. Both the diameter of the focus spot and the scanning rate are controlled by a computer and adjustable.



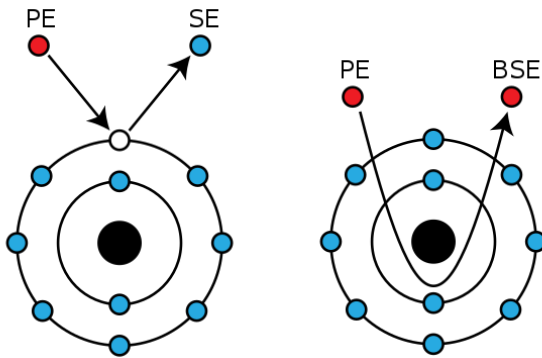
**Figure 17.** Components in SEM (Houck, 2013) .

Figure 18 presents the interaction volume of an electron beam with an object, which ranges from 100 nm deep to micrometers and results in different phenomena.



**Figure 18.** The interaction depth of an electron beam with a specimen, and corresponding phenomena (Houck, 2013).

Secondary electron (SE) detector and backscattered electron (BE) detector (in Figure 17) collect the corresponding electrons. These data are processed to reconstruct the examined surface. In SE imaging mode, the primary electron (PE) in the electron beam hits the atom and knocks another electron out by inelastic scattering (figure 19), the expelled electron carries a relatively low energy. A perfectly even surface would be captured as uniformly grey because all the escaped electrons have the same axis. However, defects on the surface increase the incidence angle of the electron beam and the interaction volume becomes larger, more electrons can be reached by PE and thus more SE are expelled. The shade of grey depends on the electron saturation, the more collected SE, the brighter the area is, making the processed image appear 3D. 0.5 nm resolution is possible to achieve. BE on the other hand, is the same PE which deflects around the nucleus due to elastic scattering. These electrons have higher energy than of secondary electrons. Backscattered electrons are used to map out the regions' difference in chemical compositions because each element scatters electrons uniquely: light elements show up in dark shades and heavy elements appear brighter.



**Figure 19.** Emissions of SE and BSE due to inelastic scattering and elastic scattering, respectively (Houck, 2013).

### 5.6 Energy-dispersive spectroscopy

Spectroscopy measures and investigates the spectrum which is formed when a material emits or interacts with electromagnetic radiation. The concerned spectrum is of characteristic (secondary) X-rays, which is from the deepest interaction volume when measuring with electron beam (figure 18) or XRF (chapter 5.2). EDS is often equipped in a SEM (figure 17) or XRF system because of these two excitation methods, so EDS can be carried out simultaneously in the same experiment. The characteristic X-ray's energy spectrum is separated by EDS and then the system software determines the abundance of specific elements based on that energy spectrum.

EDS can be used to identify roughly the chemical characterization; the detecting ability depends largely on surface's condition so it is usually not favored in highly accurate elemental composition measurements, but other methods would be utilized, such as XRF. EDS' abilities also include mapping elemental distribution, which would be employed in this thesis together with SEM in a Hitachi SU3500 scanning electron microscope.

## 6 SAMPLE PREPARATION

A predetermined powder of Ni-Mn-Ga with specific composition was prepared and nine samples were then manufactured by L-PBF by the second supervisor. After that, the chemical compositions were measured by XRF and three samples were selected for further studies. Each of these was cut into two parts, one went through heat treatment and one remained as built. Their surfaces were cleaned, and the rest of measurement methods was performed: LFMS, XRD, SEM, EDS.

### 6.1 Ni-Mn-Ga powder

Three elements in powder form were blended to a nominal composition of  $\text{Ni}_{48.7}\text{Mn}_{30.7}\text{Ga}_{20.6}$  in an argon gas atomization process. Mn was expected to evaporate during L-PBF process so its proportion in the pre-alloy powder was higher than expected. The nominal composition of the powder was calculated as an average of 15 XRF measurements at different spots. The powder was then mechanically sieved to select particles of diameter 80  $\mu\text{m}$  or smaller. 202107 particles were analyzed in a Malvern Panalytical Morphologi G3S automated optical particle analyzer. Figure 20 presents the plotted results, in which CE diameter in the horizontal axis is scaled in logarithmic order.

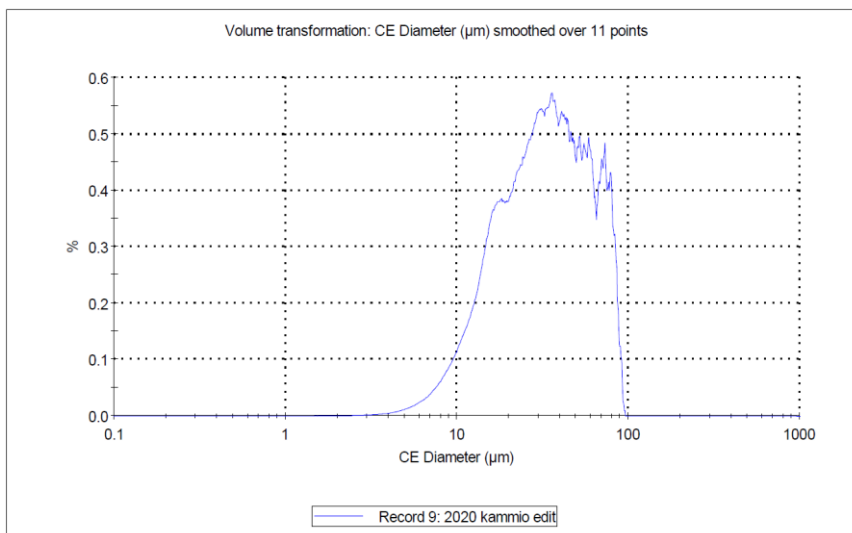


**Figure 20.** Particle size distribution based on volume calculation of the initial Ni-Mn-Ga powder (© Laitinen Ville, 2020).

The diameter value of the lowest decile is  $D[v, 0.1] = 13.67 \mu\text{m}$ , of the median is  $D[v, 0.5] = 32.8 \mu\text{m}$ , and of the highest decile is  $D[v, 0.9] = 69.5 \mu\text{m}$ . Varying particle diameters was desired as it would improve fill rate during layer coating, resulting in more even thickness. Volume-weighted circularity and elongation distribution medians are 0.94 and 0.13 respectively, suggesting highly spherical morphology. This is also supported visually by SEM image of the powder (figure 21); the majority appears round, and only a minority possesses irregular shapes.

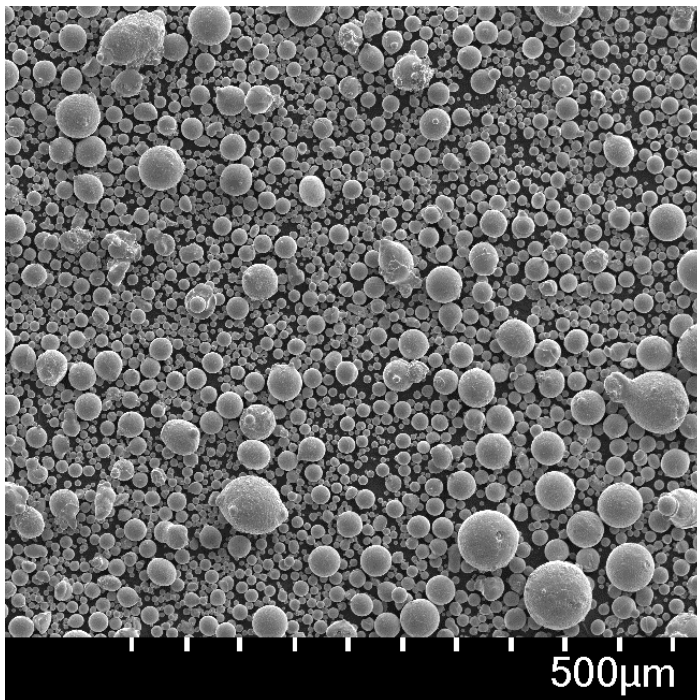


**Figure 21.** SEM image of the analyzed powder batch (© Laitinen Ville, 2020).

To remove possible excessive moisture, the powders were dried at approximately  $80^{\circ}\text{C}$  in 3 hours. Moisture on the powder particle could contribute to the generation of gas pores.

## 6.2 Manufacturing process

Although unfused powder is reusable, the dimensions of the build chamber in the existing PBF system at LUT University requires substantial volume of initial fill powder which is impractical for Ni-Mn-Ga. Pre-alloy Ni-Mn-Ga powder is expensive and difficult to prepare, only a small amount is acquired for these experiments. Thus, a L-PBF system has been developed in-house to facilitate the manufacturing of Ni-Mn-Ga samples (figure 22). It uses approximately 25 g of fill powder instead of 10 kg in the normal system.

The laser beam is produced by an IPG YLS-200-SM-WC laser, whose core is ytterbium fiber and operates with continuous wave and single mode. The laser has a wavelength of 1075 nm, and a power of 200 W. The laser beam was measured at focal point with a Primes MicroSpotMonitor, its power forms a near-Gaussian distribution (figure 22). The beam focal point's diameter is approximately 82  $\mu\text{m}$ , the beam's Rayleigh length is 3.24, and the beam parameter product is 0.53 mm $\times$ mrad. SCAPS SAMLight scanner software with 3D function were utilized to control the laser and the SCANLAB intelliSCAN 10 galvanometer scan head (a) at the same time.

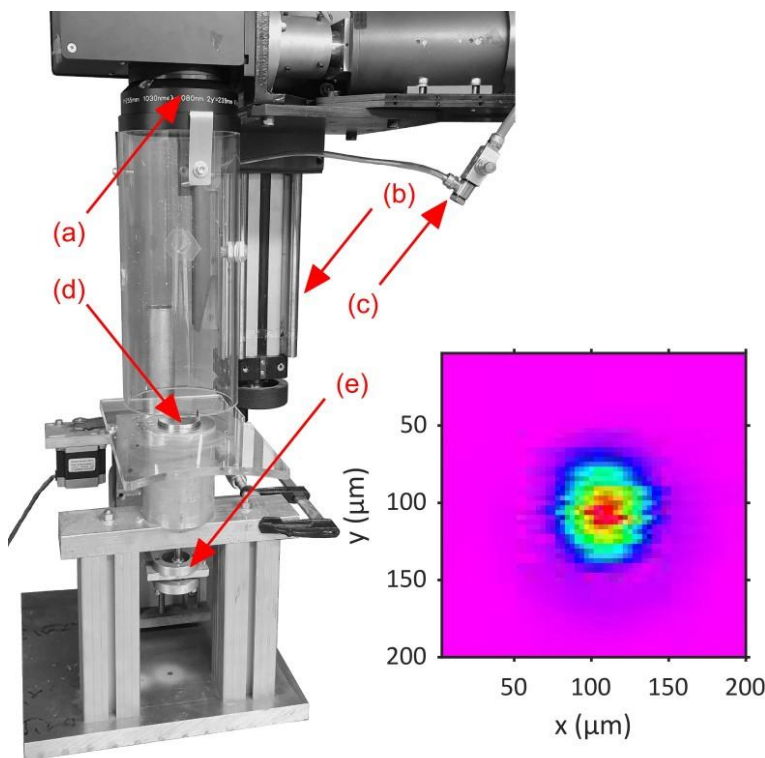


**Figure 22.** The L-PBF system without the re-coater used to manufacture the samples. (a) galvanometer scan head and focusing optics, (b) guide to adjust the focal point along z-axis (perpendicular to the build platform), (c) argon supply, (d) build platform and a pure Ni build base mounted to its slot, and (e) step motor to adjust the position of the substrate in the z-direction. The inserted graph shows the laser beam's measurement result. (Laitinen, 2021)

The build platform (d) was mounted onto a step motor (e), which could be remotely controlled with high precision and directly affected the distributed powder layer thickness. The top of the build platform had a slot, into which substrate pieces were fixed as the base for building. Bases were removable and made from different materials for various experiment designs; maximum dimensions for substrate pieces were 46 mm for diameter and 10 mm for thickness. To ensure the same powder layer thickness is repeated from patch

to patch, the semi-automated re-coater blade (not presented in figure 22) was mechanically calibrated before the powder is heated. The build chamber was formed by 5-mm plexiglass rolled into a  $\varnothing 120$  mm tube bolted to the focusing optics (a). High-purity argon shield gas was pumped into the chamber through the tube (c) at a flow rate of 3l/min.

A batch of samples was manufactured with the pre-alloyed powder composition in the in-house built testbed system. Figure 23 demonstrates the built patch. All samples were built on a base made of Ni substrates of diameter 45 mm. Ni substrates of high purity ( $>99.5\%$ ) were selected to reduce the possibility of elemental contamination to the Ni-Mn-Ga samples, and to make sure the base and the samples are chemically compatible. Previously, stainless steel substrate was used for cost reason, but EDS inspection of the substrate-sample interface revealed that the substrate had been melted and compositionally mixed into the deposited samples (Laitinen *et al.*, 2019). Nine samples of the size  $5 \times 5 \times 5$  mm<sup>3</sup> were arranged in a 3x3 position with 5 mm gap between them in each direction to prevent thermal interaction during the building process. The samples are oriented at an angle of  $45^\circ$  relative to the system's x-y hatch directions. These placements were selected to allow the re-coater blade to operate smoothly along the platform's x-direction, as well as decrease the risk of the re-coater colliding with the built cuboids.

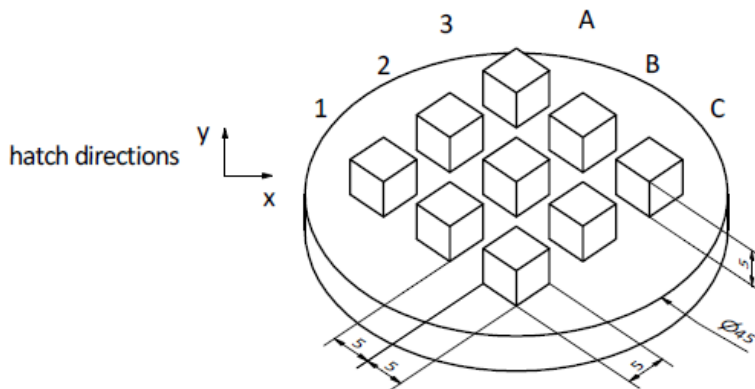


**Figure 23.** Samples' built dimensions.

Three parameter sets were chosen based on previously optimized processes (Laitinen *et al.*, 2019). Each set was applied to a column of three cuboids (1, 2, and 3 in figure 23), the values are listed in table 1. The volume energy density (VED) is calculated as:

$$VED = \frac{P}{v \cdot h \cdot t} \quad (3)$$

Table 1. L-PBF process parameters used for each set of samples.

Parameter \ Column	1	2	3
Laser power P (W)	200	200	200
Scanning speed v (mm/s)	1000	750	500
Hatch distance h ( $\mu\text{m}$ )	100	100	100
Powder layer thickness t ( $\mu\text{m}$ )	60	60	60
VED ( $\text{J}/\text{mm}^3$ )	33.3	44.4	66.7

The samples were scanned on the substrates at ambient temperature in an atmosphere of pure inert argon to minimize oxidation. The substrates were not preheated. The laser beam was utilized for both hatching and contouring processes; it was focused on the powder bed's surface during the printing procedures. Figure 24 presents the scanning strategies for the samples. The cuboids were hatched by a bidirectional scanning method, the scanning direction rotates  $60^\circ$  from one layer to the next. The hatched regions, in square shape, were enclosed by a single continuous contour scan, which overlaps roughly 90% of the inner hatches. Both hatching and contouring employ the same set of parameters specified for the samples.



**Figure 24.** Schematic scanning strategies for the samples, viewed from the top. Orange line represents hatching and blue line represents contouring. Modified, (Biffi *et al.*, September 11, 2019)

### 6.3 Surface finishing

The as-built surfaces were rough and porous, which negatively affect results of measurements taken on them. Cleaning and polishing were applied to ensure accurate evaluation. All nine samples remain on the base for the first round of surface finishing. This round consists of grinding all samples' top surfaces with SiC abrasives then diamond paste for XRF composition determination.

Figure 25 demonstrates the polishing procedure. SiC foil was attached to the turn table, abrasive side facing up. The foil rotates with speeds up to 500 rpm, adjusted from the control panel. Its face was constantly wetted (a). The workpiece, held downward, was lightly pressed on the abrasive while it rotates (c), the workpieces was moved in circular motion around itself (b) so that the polishing grooves from SiC grains would not systematically align. Foils of different grain sizes were used in increment order, while the turntable's speed varied from 250 rpm (middle) to 500 rpm (maximum). The workpiece was ground with each abrasive foil continuously for 30 seconds to 1 minute, then dried completely from water using a napless cloth before moving on to the next foil. At the end of the SiC polishing sequence, the turntable was stopped, and the workpiece was gently circulated a few times to remove visible scratches. The last SiC foil was then removed, and diamond paste was spread onto the turntable. The workpiece was ground starting from the middle of the pad at very low rotational speed and then speed is slowly increased.



**Figure 25.** Surface polishing process. (a) water source, (b) workpiece in face-down position and rotated around its center axis, (c) SiC abrasive foil, rotates around its center axis with adjustable speed.

Finally, the ground surface was cleaned with ethanol, blow-dried, rinsed with water, and blow-dried again. Figure 26 presents the polished surfaces free from observable scratches.



**Figure 26.** The samples with their top surfaces polished.

All samples were ready for the first XRF measurement. Based on the compositional results, three samples were selected from total nine for further investigations. The results would be discussed in detail in the result chapter. All pieces were detached from the base by a Princeton Scientific Corporation WS2 high-precision wire saw, which introduced minimum strain into the crystal structures compared to other cutting methods. These three samples were then electropolished in a nitric acid and ethanol mixture with 6-4 ratio. The polishing setup is presented in figure 27. A 600-rpm vortex was form in the liquid to rinse the sample's surface while it was being polished in the pool. The mixture was constantly cooled at 20°C by ethanol supply. The sample is clamped to the positive (red) cable and the negative (black) clamp was attached to the liquid. Voltage was applied in the range of 0.5 to 1.5 V and current was in the 0.6 to 0.8 A range. Each sample was dipped for approximately 20 seconds, rinsed with water and dried on a napkin, then repeated one more time. At the end, the samples were cleaned with acetone to remove possible contaminants from the surfaces.

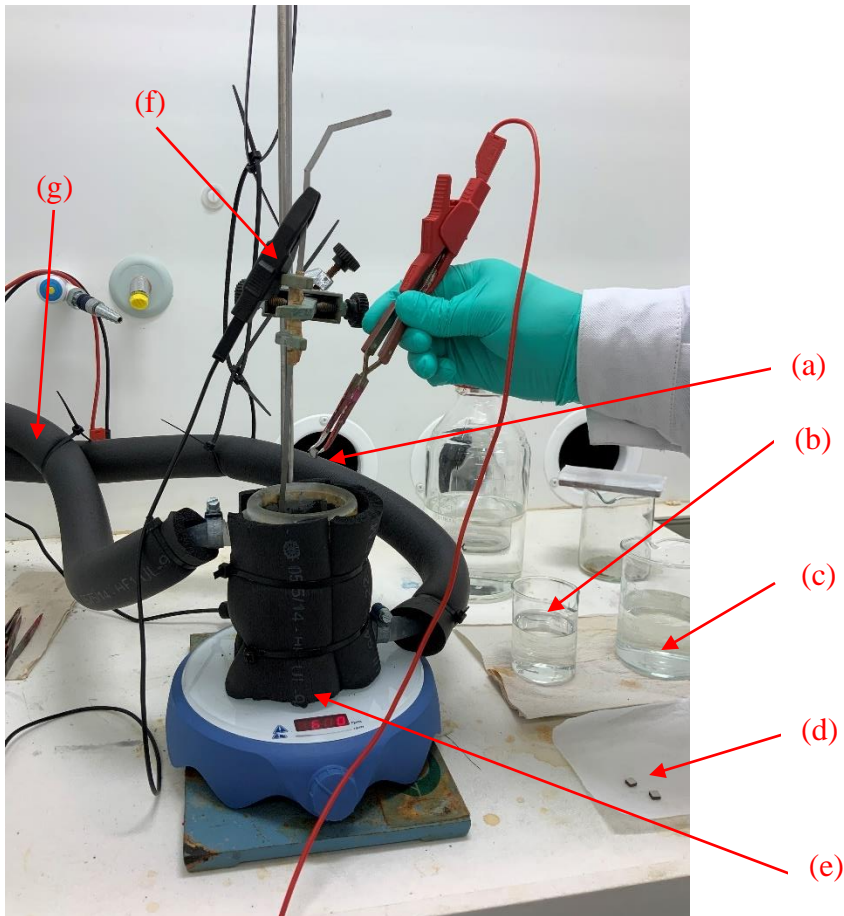


**Figure 27.** Electropolishing setup. (a) sample and positive clamp, (b) water, (c) acetone, (d) damping napkin and other waiting samples, (e) polishing mixture container, (f) negative clamp, (g) coolant pipes.

XRD and LFMS measurements were performed on these three as-built samples. Each sample was subsequently sawed in two halves by the same high-precision wire saw. Bigger half went on to the heat treatment process and the other one stayed as built.

Each sample going through SEM and EDS measurements was also cleaned with CO<sub>2</sub> ice spray (80°C) to remove dirt and contaminants on the surface, and subsequently blown with dry air to warm up the sample and to prevent water condensation on the cold sample surface.

#### 6.4 Heat treatment

Three halves intended for heat treatment, now called samples, were electropolished one more round before being placed on a high-purity alumina holder in the shape of a boat. A small piece of titanium was placed into the same boat, acting as an oxygen-getter. Figure 28 shows the heat treatment system, which was developed in-house. The boat with the samples and

titanium oxygen-getter was laid in the middle tube of the furnace (d) and the furnace was closed tightly. It was possible to observe the boat through a vacuum window at the other end of the tube on the outside. The pressure in the furnace tube was depleted until high pressure was obtained using a Pfeiffer vacuum HiCube 80 Eco turbopump (b), which switched on at 0.2 kPa, and a Pfeiffer vacuum MVP 015-4 diaphragm pump. The pressure could be monitored by the Oerlikon Leybold Vacuum PTR 90 N vacuum meter (c). High-purity argon (a) was pumped into the chamber and maintained at 30 kPa at ambient temperature, which helped to minimize Mn evaporation when the temperature raised in vacuum. This argon pressure was selected with expectation of the gas' thermal expansion and consequently increased pressure during heat treatment.

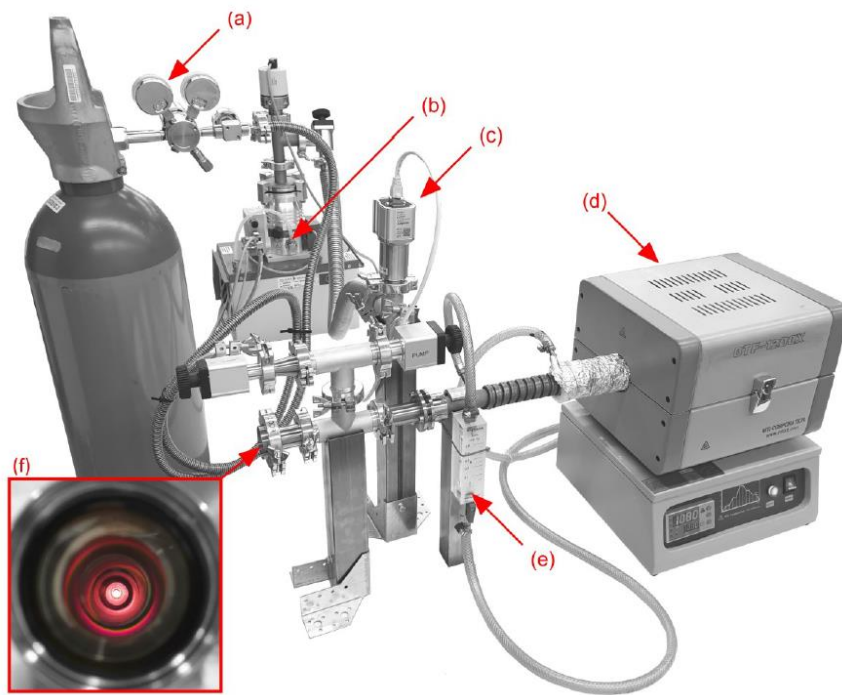


**Figure 28.** Heat treatment system. (a) high-purity argon supply, (b) vacuum turbopump, (c) vacuum meter, (d) furnace, (e) coolant flow meter, (f) sample observation window. (Laitinen, 2021)

The parameters for the heat treatment process are presented in table 2.

Table 2. Heat treatment parameters.

Parameter (unit)	Value
Heating rate from ambient temperature to homogenization temperature ( $^{\circ}\text{C}/\text{h}$ )	250
Homogenization temperature ( $^{\circ}\text{C}$ )	1080

Homogenization time (h)	24
Cooling rate from homogenization temperature to ordering temperature (°C/h)	100
Ordering temperature (°C)	800
Ordering time (h)	4
Cooling rate from ordering temperature to ambient temperature (°C/h)	Furnace cooling

The solidus temperature (at which a material is completely solid) and the transition temperature of  $L2_1 \rightarrow B2'$  ordering for the material composition used in this thesis were estimated based on ready literature (Schlagel *et al.*, 2000) (Aaltio *et al.*, 2009) as 1110°C and 765°C, respectively. These values were used to set the important temperatures used in the heat treatment process. Initially, the pieces were homogenized at high  $T_h$  temperatures in corresponding durations. After that, the temperature was lowered to facilitate ordering transition, and then finally cooled to ambient temperature by furnace cooling. The boat came out of the furnace with the titanium oxygen-getter shiny, indicating that the heat treatment had gone well and there was no noticeable oxidation. Quick check by XRF (three points for each sample) to confirm the compositions correspondence to markings revealed that significant amount of Mn evaporation did not occur.

## 7 RESULTS AND DISCUSSION

The samples went through the measurements in the following order:

- XRF of nine as-built samples on the base after first round of surface polishing.
- XRD of three selected as-built samples after first round of electropolishing.
- LFMS of three selected as-built samples after first round of electropolishing.
- LFMS of three selected heat-treated samples.
- SEM and EDS of three selected heat-treated samples.
- SEM and EDS of three selected as-built samples.
- XRD of three selected heat-treated samples.

The results would be presented in pairs of the same measurement type for as-built and heat-treated samples. Grinding, electropolishing or gas cleaning was repeated as much as necessary before each measurement.

### 7.1 XRF

All nine as-built samples on the base were placed into the Oxford Instruments X-Strata 960 XRF spectrometer after spectrum calibration. 5x5 grid measurement path was pre-programmed for each sample. Thus, each sample would have 25 values for the calculations of average and standard deviation values. Figure 29 demonstrates how the paths were setup.

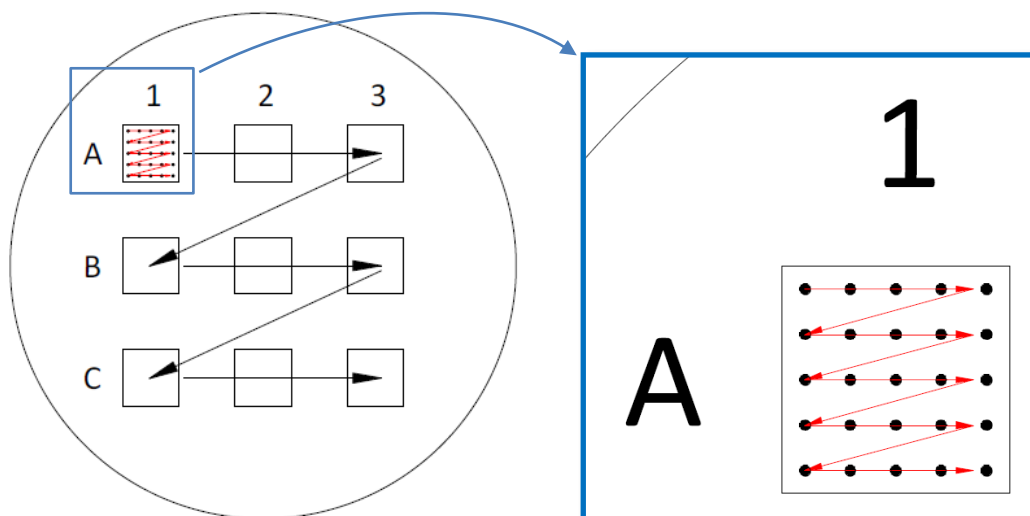


**Figure 29.** XRF measurement paths.

The weight percentages of three elements Ni, Mn, Ga were recorded for each location and they were converted to atomic percentages by formula 3 (for Ni, Mn and Ga could be done by using their corresponding atomic masses). The atomic masses for Ni, Mn, Ga are 58.6934, 54.938, 69.723 respectively.

$$at.\%Ni = \frac{\frac{wt.\%Ni}{58.6934}}{\frac{wt.\%Ni}{58.6934} + \frac{wt.\%Mn}{54.938} + \frac{wt.\%Ga}{69.723}} \cdot 100 \quad (4)$$

The average and standard deviation of each element's atomic contribution are presented in table 3.

Table 3. Atomic compositions of nine as-built samples.

Sample	Composition		
	Ni (at.%)	Mn (at.%)	Ga (at.%)
<b>A1</b>	<b>49.81 ±0.20</b>	<b>29.23 ±0.24</b>	<b>20.96 ±0.08</b>
<b>A2</b>	<b>50.21 ±0.18</b>	<b>28.81 ±0.20</b>	<b>20.97 ±0.06</b>
A3	50.45 ±0.31	28.64 ±0.31	20.91 ±0.08
B1	49.94 ±0.21	29.11 ±0.24	20.95 ±0.07
B2	50.30 ±0.24	28.74 ±0.25	20.97 ±0.05
<b>B3</b>	<b>50.44 ±0.21</b>	<b>28.64 ±0.24</b>	<b>20.92 ±0.06</b>
C1	49.78 ±0.17	29.41 ±0.24	20.81 ±0.10
C2	50.28 ±0.25	28.84 ±0.29	20.88 ±0.07
C3	50.44 ±0.25	28.61 ±0.24	20.95 ±0.07

It could be seen that the standard deviations are generally within the 0.3% accuracy of the XRF instrument, meaning that the samples were highly homogenous, and the elements were distributed evenly. Porosity or cracking influence the quality of the measured surface locally, which may occasionally result in small errors in the obtained readings. Samples A1, A2, B3 had the most minimal deviations and represented three different processing parameters (table 1) so they were selected for further investigations. These three samples and their composition were in bold format in table 3 to highlight the selection. The distribution of Ni on the surfaces of the selected samples is plotted in figure 30. Sample name and atomic percentage of each element were mentioned in each plot's title.

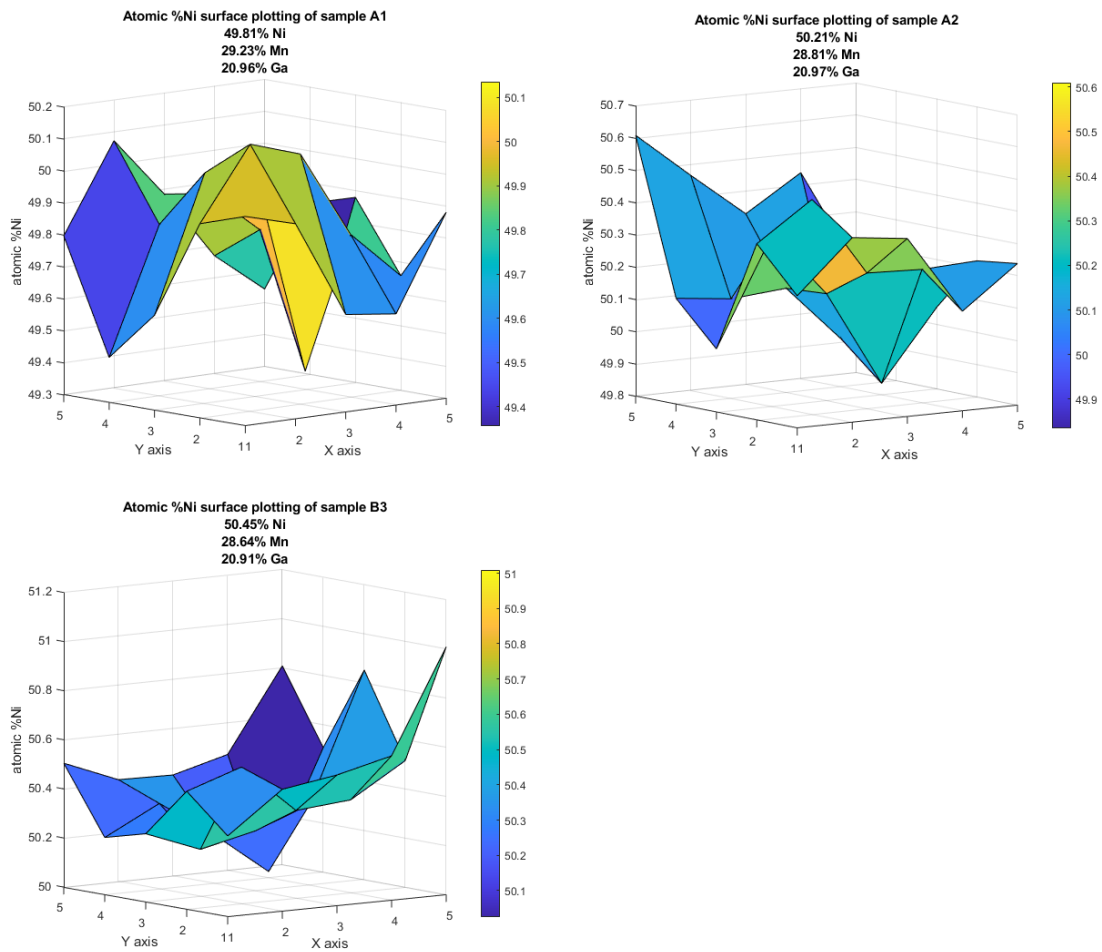


**Figure 30.** At.%Ni surface plotting of chosen samples A1, A2, B3.

For simplicity, from here on, sample names are changed to S1, S2, S3 respectively, with AB and HT suffixes standing for as-built and heat-treated.

## 7.2 LFMS

The phase transformation during heating of the selected samples, both as-built and after heat treatment, was recorded from the LFMS experiment and plotted. During heating, the first-order structural transformation from martensite to cubic and the second-order phase transformation from ferromagnetic to paramagnetic were observed, and the reversed was followed during cooling. Figure 31 shows the transformations of as-built samples with Curie temperatures illustrated as opaque red regions. Magnetization values have been normalized with arbitrary unit (a.u.).

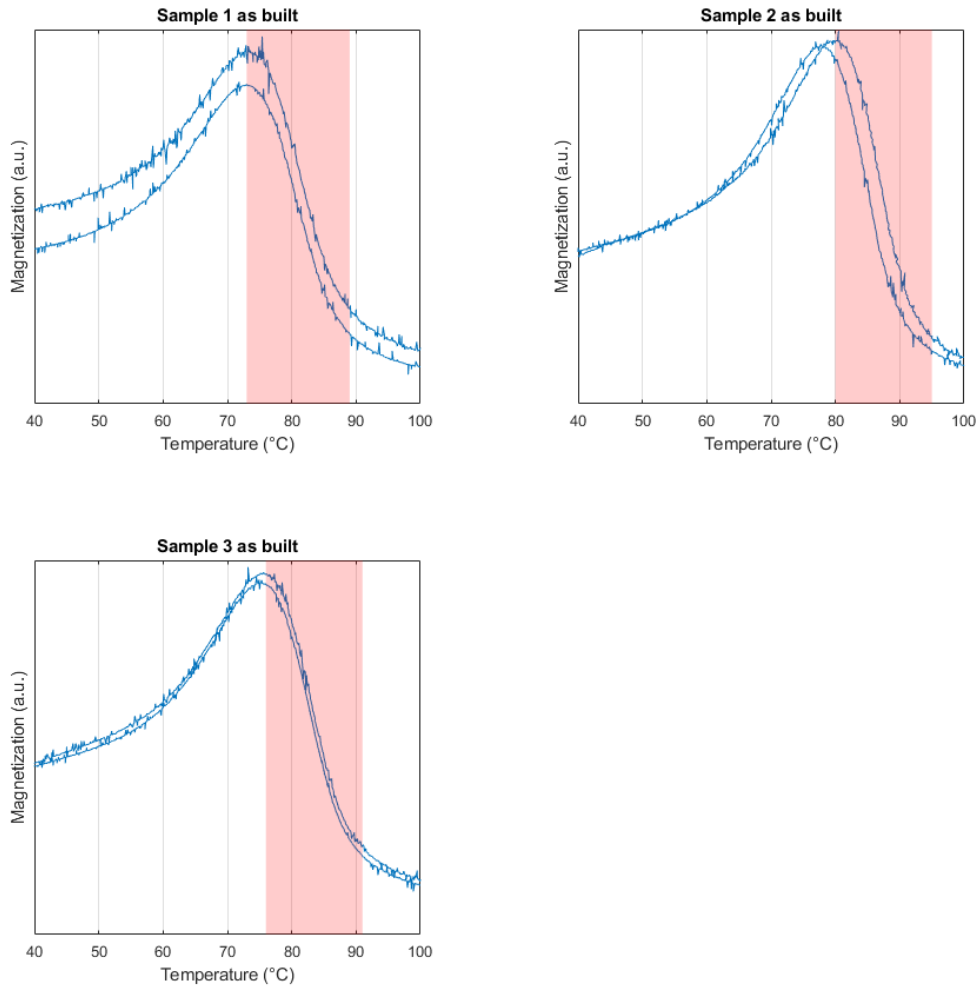


**Figure 31.** Magnetization plotted against temperature change for as-built samples. Red region in each subplot roughly indicates Curie temperature.

All three as-built samples had similar magnetization curve, and their second-order phase transformation extended across approximately 15°C, though starting from different temperatures between 70°C and 80°C. The transformation was recorded for both the heating and cooling processes. The transition reversed during cooling down, and magnetization had slightly lower magnitude and shifted to the left. The magnetic properties of these samples were poor, the first-order structural transformation was not possible to identify due to the first half of the slope being too gentle and broad. The data also contain noticeable noises caused by possible internal stress from the L-PBF process, lack of long-range order, and small size of sample. These issues are well known and have been addressed in published article (Laitinen *et al.*, 2019).

Phase transition upon temperature change of heat-treated samples is shown in figure 32.

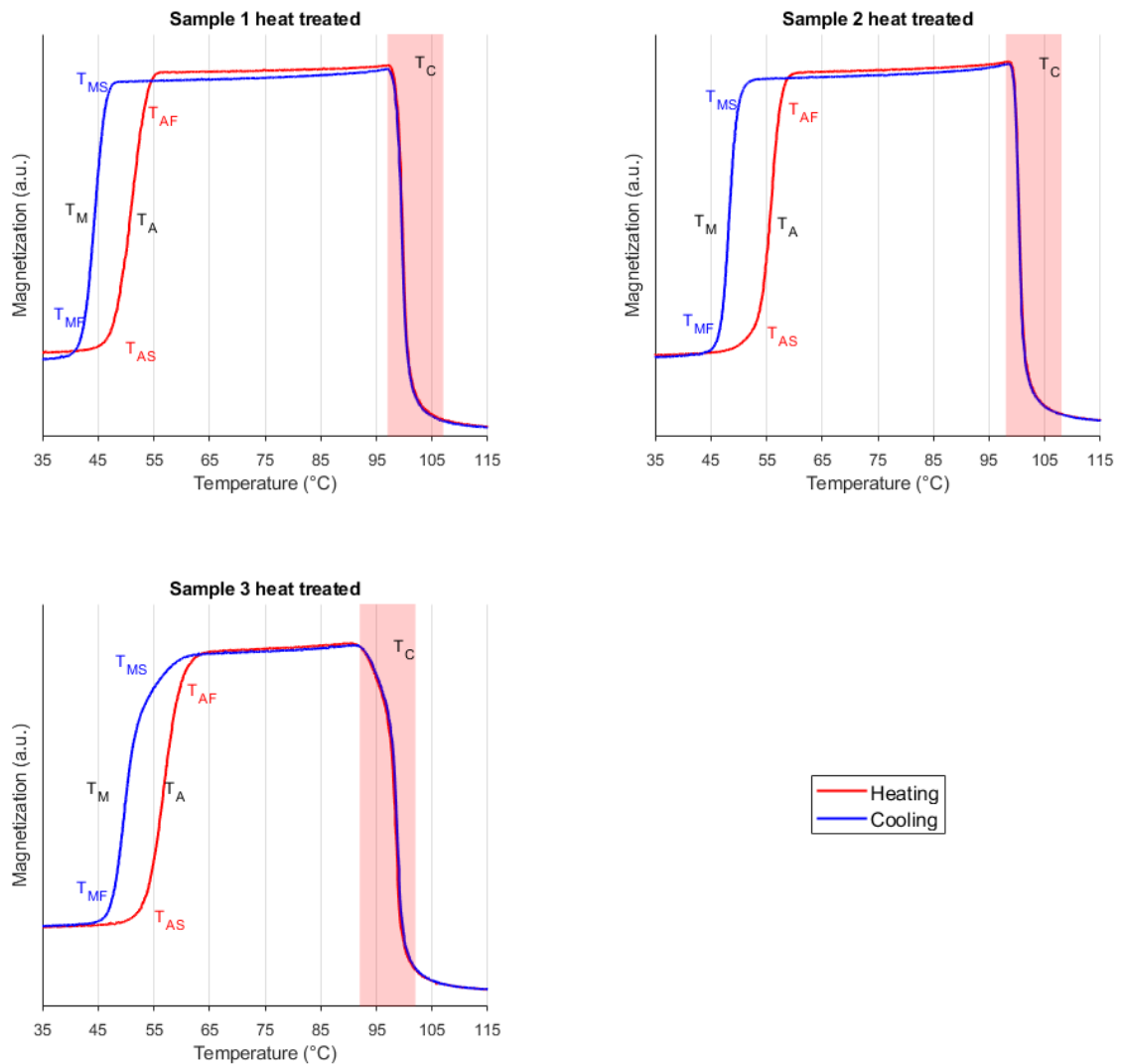


**Figure 32.** Magnetization plotted against temperature change for heat-treated samples. Red line represents heating up and blue line represents cooling down. In each subplot, red region roughly indicates Curie temperature  $T_C$ .  $T_{XX}$  is temperature point, in which M means martensite, A means austenite, S means start, and F means finish.

It could be seen clearly that the Curie temperatures have become much narrower, and the slope appeared steeper, ranging only within 5°C to 6°C. The starting point of the second-order phase transformation was higher, at around 95°C. The first-order structural transformation could be observed for these samples. The transition from austenite to martensite upon cooling happened at 5°C lower in reverse of the transition from martensite to austenite upon heating. These readings possessed less noise than of the as-built samples.

The minor difference among the samples' plots was the result of different processing parameters, which produce compositions of varied elements. The utilized LFMS measurement only provided qualitative results so the phase shift cannot be evaluated quantitatively, and the transformations of as-built and heat-treated variants of the same sample could not be plotted together for the comparison of magnetization magnitude.

### 7.3 XRD

The selected samples, before and after heat treatment, were examined in the X-ray diffractometer under the same setup at ambient temperature described in chapter 5.4. The reflected intensities between  $20^\circ$  and  $100^\circ$   $2\theta$  range were recorded and plotted in figure 33. The as-built and heat-treated versions of each sample were plotted on the same base line to demonstrate the difference in diffraction intensity, especially at the peaks, where heat treated versions express noticeably higher intensity while being narrower.  $2\theta$  angles were identified for the main peaks and used in calculations to determine the lattice parameters a, b, and c. The indexes of the peaks were marked according to the parent austenite unit cell coordinate system. Unlabeled peaks were modulated superstructures which appeared after the heat treatment process. The calculation template was provided, in which lattice parameters were modified until resulting peaks matched with acquired peaks from XRD patterns.

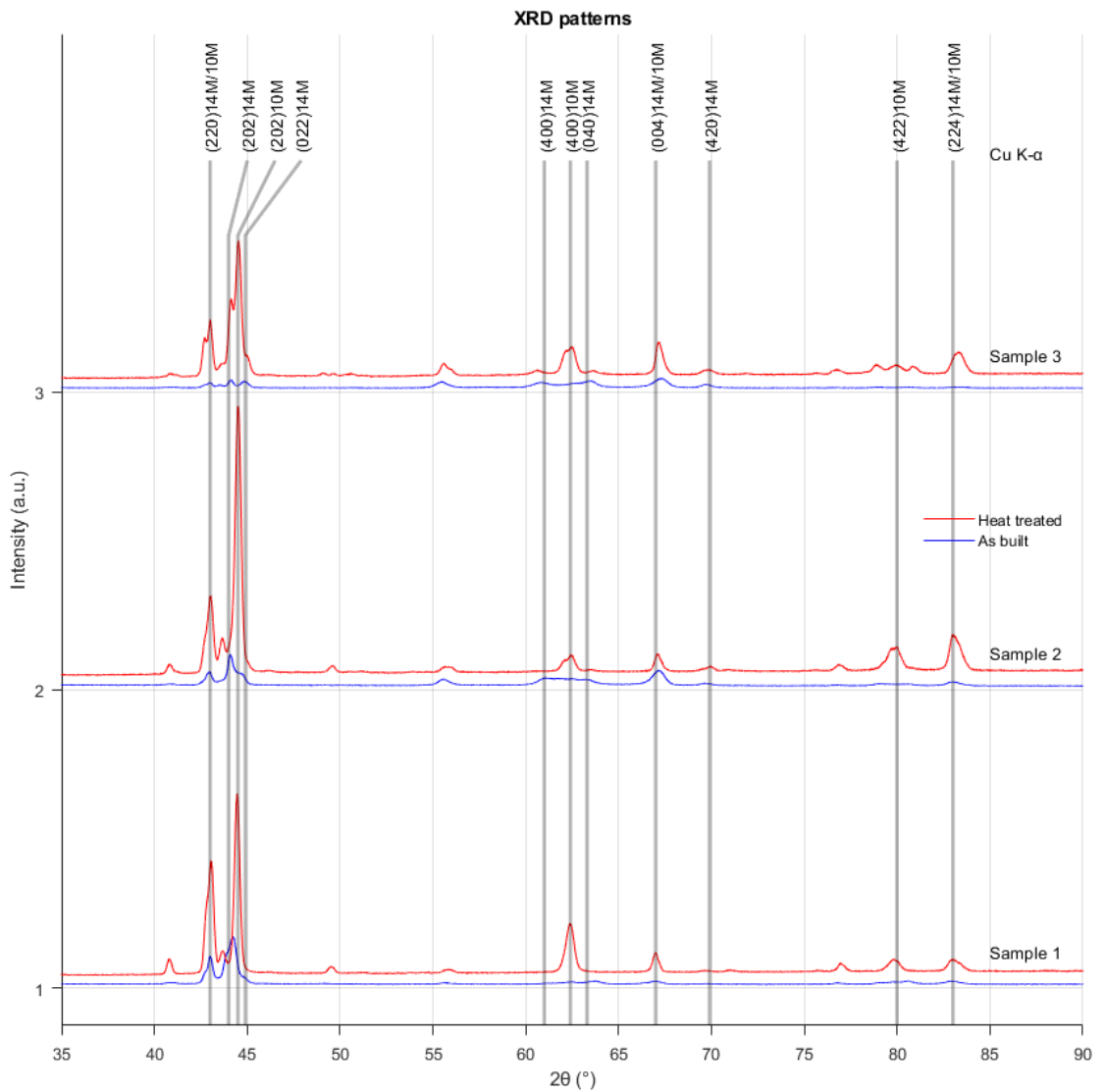


**Figure 33.** X-ray diffraction spectrums of three selected samples, as-built and heat treated. Gray vertical lines represent identified peaks and their corresponding indexes. Peaks without markings are results of modulated superstructure.

S1AB and S1HT exhibited crystal structure of 10M martensite, with their highest intensity peaks at approximately  $44.5^\circ$ . Other visible 10M peaks of S1HT were near  $43^\circ$ ,  $62.5^\circ$  and  $80^\circ$ , at which S1AB's 10M peaks could be seen as short bumps. S2AB and S3AB's structures were 14M martensite, demonstrated by peaks near  $44^\circ$  and close to  $67^\circ$ . S2HT had mainly 10M structure, with a possible mix of NM at small quantity, whose lattice parameters were not possible to estimate. Its notable peak also located near  $44.5^\circ$  and other intermediate

intensities peaked at 62.5° and 80°. Lastly, S3HT was a combination of 10M and 14M martensite structures, with more peaks than others though less intensive.

The peaks in the diffractograms of as-built samples were broad and their intensities were oddly low. It was difficult to identify correct  $2\theta$  angle corresponding to each peak for the lattice parameter calculation. These characteristics suggested that variations of lattice parameters appear locally in the as-built samples because of varied composition and internal stresses arose from the L-PBF process (Laitinen *et al.*, 2019). The X-ray diffraction quality of heat-treated samples has improved significantly, the peaks had high intensities and appeared narrow, from which  $2\theta$  angles were easily identified. The improvement in quality came from increased grain size toward single crystal and long-range order after the heat treatment process. The observable difference in the spectrums of as-built and heat-treated samples could be contributed by the homogenization and stabilization of chemical composition during heat treatment process, which eliminated some additional lattice parameters presented locally in the as-built samples. Oxides were not detected in the diffraction spectrums, suggesting that oxygen did not present with a significant measure in the samples. Table 4 summarizes the lattice parameters of the samples.

Table 4. Summarized martensite lattice parameters of as-built and heat-treated samples in the XRD measurements.

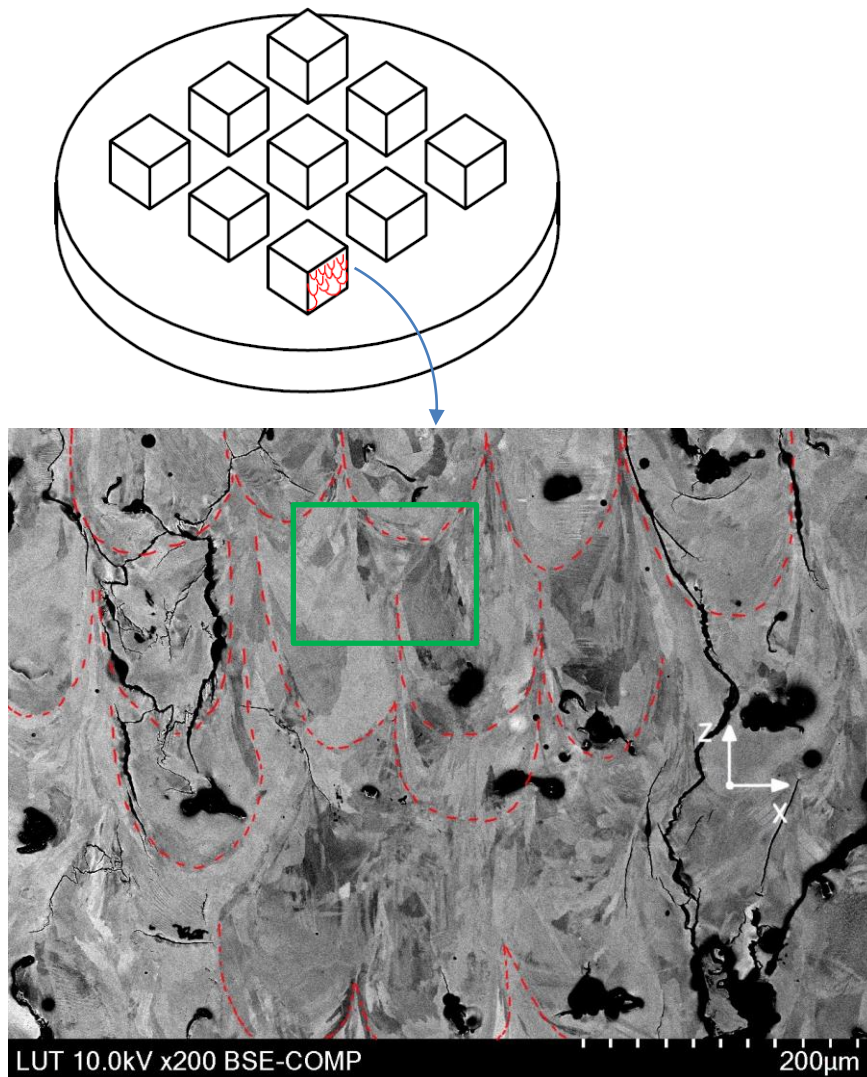
Parameter Sample	a (Å)	b (Å)	c (Å)	$\gamma$ (°)	c/a	Phase
S1AB	5.95	5.95	5.59	90.33	0.94	10M
S1HT	5.95	5.95	5.58	90.33	0.94	10M
S2AB	6.07	5.88	5.57	90.55	0.92	14M
S2HT	5.98	5.95	5.58	90.33	0.93	10M
S3AB	6.09	5.88	5.56	90.55	0.91	14M
S3HT	5.97	5.94	5.57	90.33	0.93	10M
	6.11	5.85	5.57	90.55	0.91	14M

All lattice parameters were shown with accuracy of approximately  $\pm 0.01\text{Å}$  and  $\pm 0.01^\circ$  in the austenite unit cell coordinate system. Non-experimental (constant) values of  $\gamma$  were employed, with  $90.33^\circ$  used for 10M structure and  $90.55^\circ$  for 14M structure. These values

have been identified as typical for these crystal structures. This approach facilitated simplification of the XRD analysis. Lattice parameters varied from sample to sample, due to different processing parameters resulting in various chemical compositions examined in XRF experiment.

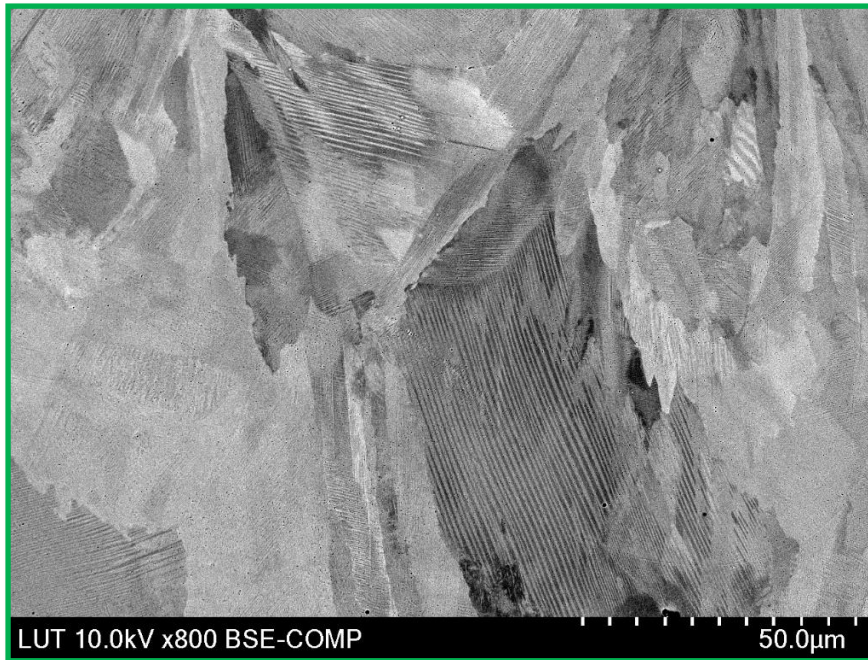
#### 7.4 SEM

Three as-built samples' and three heat-treated samples' microstructures were observed in SEM. All SEM images of six samples at different magnifications are attached in the appendices. Overall, the microscopic images of the surfaces are typical for Ni-Mn-Ga alloys fabricated by L-PBF. Few captures were selected to discuss in this chapter. Figure 34 shows the backscattered electron image of S1AB's surface perpendicular to the build platform at 200x magnification. Some separation of scanned tracks was observed and marked with red dash lines. During the electropolishing process, electrons have hit the edges of these cracks and pores, making them appear notably larger in SEM images. Large cracks dominate the as-built sample's captured surface, and in this view, some of them run along the boundaries of the laser melted tracks. In general, Ni-Mn-Ga alloys are brittle and thus susceptible to crack under internal stress, which built up by large thermal gradient during the L-PBF process due to sample size, or other material removal procedures such as cutting as grinding. Considerably thinner build, with thickness of merely 0.8mm, has reduced internal stress and subsequently demonstrated no crack (Laitinen *et al.*, 2022).



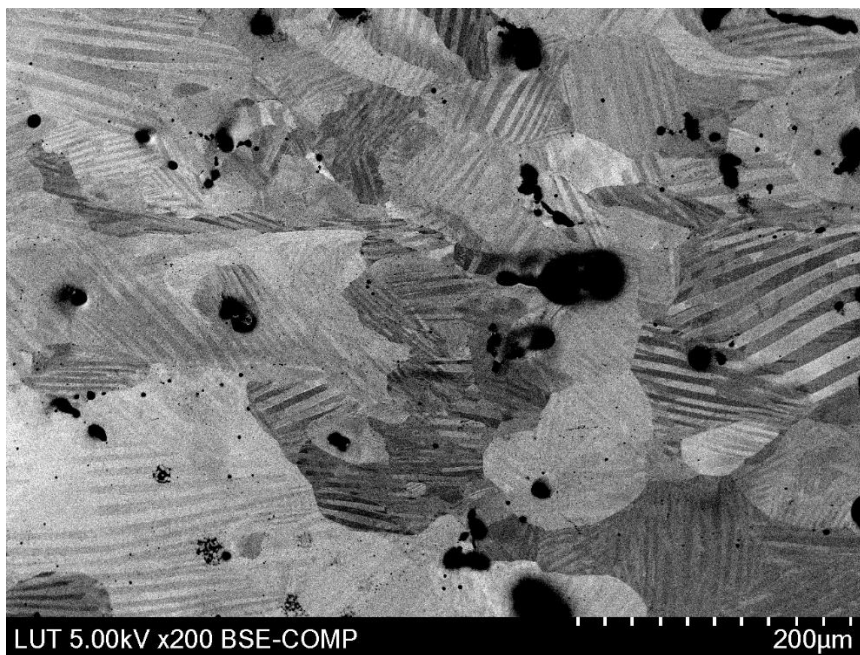
**Figure 34.** SEM image of S1AB at 200x magnification, showing boundaries of deposited hatches (red dash lines) along the build direction. View orientation is noted as xz plane, the coordination system remains the same as described earlier.

Figure 35 enlarges a section of the same view on S1AB, at 800x magnification. In the middle of the figure is a grain with martensitic twin variants in the form of sandwiched light and dark colored stripes. The twins presented with different sizes and in different orientations across grains. Smaller grains can be seen at the border of the scanned tracks. Tree-like dendrites did not appear in these pools even though they are usual crystal growing structure in solidifying materials. Instead, the grains grew in columnar form during cooling due to the typical thermal gradient induced by the L-PBF process.



**Figure 35.** SEM image of S1AB at 800x magnification, of the section marked with green boundary in previous figure.

After heat treatment, the grains became larger as well as twins, and cracks were eliminated. Grain growth was shown to be dependent on homogenization temperature and applied duration (Laitinen *et al.*, 2021). Figure 36 presents the surface of S1HT sample, at 200x magnification. Some nanoscale twins were even noticed within a twin (figure 37).



**Figure 36.** SEM image of S1HT at 200x magnification. No prominent crack was observed.

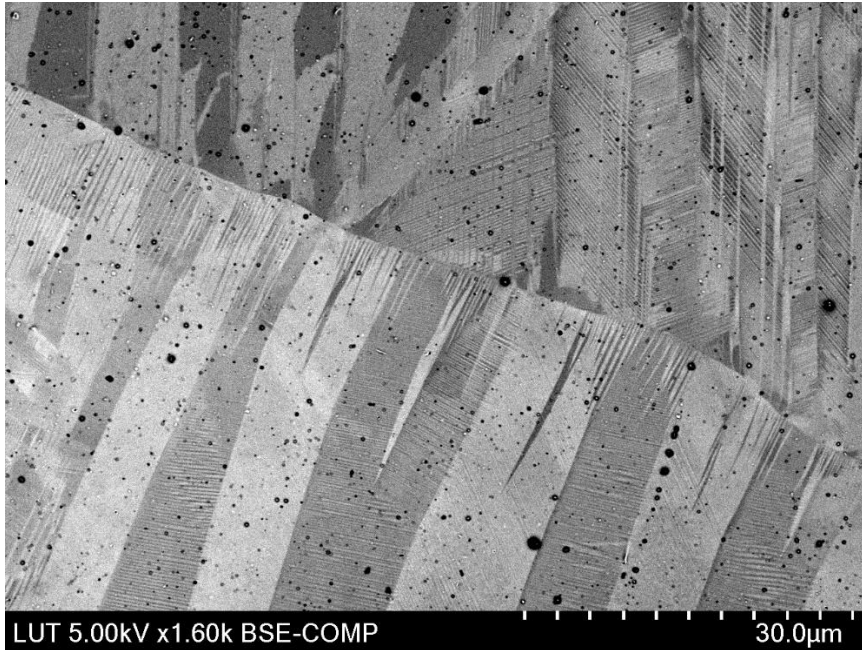


**Figure 37.** SEM image of S2HT at 1600x magnification. Thin twins can be seen within larger twins.

#### 7.5 EDS

During the SEM imaging sessions, EDS measurements were carried out for the same captured areas. EDS images of Ni, Mn, and Ga distributions on the sample surfaces are attached in the appendices. Figure 38 shows the elemental distributions on the same area of sample S1AB as in figure 34. Even though the SEM image presented multiple grains and large surface defects, the main elements Ni, Mn, and Ga spread moderately even, except for the deep crack at the lower right corner. O map indicates that large black spots seem to be MnO originated from the L-PBF manufacturing. A small patch of Si was registered, which remained on the surface after the polishing procedure. Similar observations were realized for other samples.

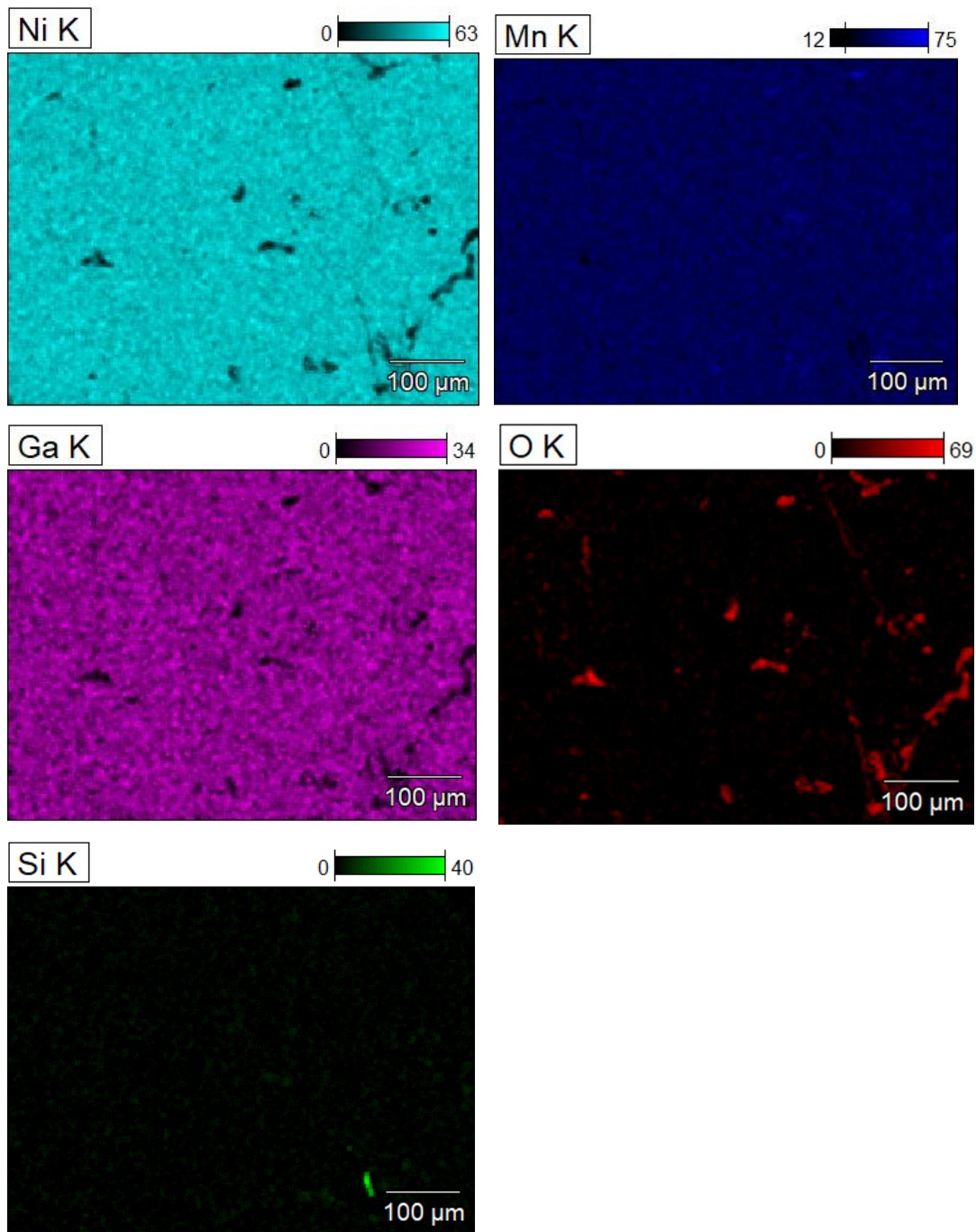


**Figure 38.** EDS images of the same area on S1AB captured in figure 34.

The samples were overall homogenous although some variation in the concentration of each element is visible across the sample surfaces in all EDS images. Some of the variation may relate to the inaccuracy of the measurement, differences in local quality of the prepared surface (pores, oxides, dirt), or small compositional gradients in the built material.

## 8 CONCLUSIONS

The purpose of the thesis was to research the properties of Ni-Mn-Ga samples manufactured by L-PBF by several characterization methods. Nine samples were built with three sets of processing parameters. XRF results showed that all nine fabricated samples were highly homogeneous, all three elemental proportions deviated within the  $\pm 0.3$  at.% accuracy of the spectrometer. One sample of each processing parameter group was selected for further measurements.

Half of each chosen one was homogenized by heat treatment and investigated by the same procedures as for as-built samples. LFMS diagrams presented that as-built samples possessed poor magnetic properties. Their Curie temperatures were broad, spanning across  $15^\circ$  in the range of  $73$  to  $95^\circ$ . Martensite – austenite transformation was not possible to recognize for as-built pieces. Heat-treated samples had the typical phase transformations: the first-order transformation could be identified between  $40^\circ$  and  $65^\circ$ , and the second-order transformation was narrower, in the span of approximately  $6^\circ$ .

XRD spectrums of six samples demonstrated diffraction quality improvement after heat treatment. It was implied that there existed local variations of lattice parameters in the as-built samples due to internal stresses and varied compositions. They were reduced by homogenization during heat treatment. Possible intensity peaks were indexed for all samples, all heat-treated peaks were notably more intense and distinct than their counterparts. Lattice parameters were estimated based on peak locations and the values were typical for Ni-Mn-Ga alloys manufactured by L-PBF.

SEM images revealed expected microstructures with few prominent cracks on as-built surfaces, which could be contributed by electropolishing. After heat treatment, grains became considerably larger while fewer cracks occurred. Micro- and nanoscale twins were observed on the SEM images. EDS images presented moderately even distribution of elements and no substantial fluctuation in composition before and after heat treatment was observed.

The calculation results are typical for these Ni-Mn-Ga alloys and plotted diagrams are as expected based on previous examination of similarly built pieces by (Laitinen, 2021). Heat treatment has been demonstrated to substantially improve the grain quality, magnetic properties and reduce internal stresses. The results obtained in this thesis work confirm that L-PBF is a reliable and repeatable process to manufacture Ni-Mn-Ga-based polycrystalline MSMA<sub>s</sub>.

## LIST OF REFERENCES

*3D Printing: The Internal Process and Development.* (2019) Available at: <https://liveroomlk.medium.com/3d-printing-the-internal-process-and-development-988ae9b24a6b> (Accessed: Nov 28, 2021).

*Laser Beam Powder Bed Fusion - AMPOWER Report.* (2019) Available at: <https://additive-manufacturing-report.com/additive-manufacturing-metal-technology/metal/laser-beam-powder-bed-fusion/> (Accessed: Nov 28, 2021).

*X-Ray Generator* (2017) .

'X-Ray diffractometer and its various component parts for X-Ray studies', (2016) *xrd.co*, - 06-11T10:26:10+00:00. Available at: <https://xrd.co/component-parts-x-ray-diffractometer/> (Accessed: Oct 28, 2021).

*Boise State Micro-Pump Aids Neurological Research.* (2014) Available at: <https://www.boisestate.edu/news/2014/09/24/micro-pump-developed-boise-state-aids-neurological-research-england/> (Accessed: Nov 28, 2021).

*Supports in 3D Printing: A technology overview.* Available at: <https://www.hubs.com/knowledge-base/supports-3d-printing-technology-overview/> (Accessed: Nov 28, 2021).

Aaltio, I., Söderberg, O., Friman, M., Glavatskyy, I., Ge, Y., Glavatska, N. and Hannula, S.-. (2009) *Determining the liquidus and ordering temperatures of the ternary NiMn-Ga and quaternary Ni-Mn-Ga-Fe/Cu alloys.* EDP Sciences, pp. 04001.

Aaltio, I., Sozinov, A., Ge, Y., Ullakko, K., Lindroos, V.K. and Hannula, S.-. (2016) 'Giant Magnetostrictive Materials'*Reference Module in Materials Science and Materials Engineering* Elsevier.

Aboulkhair, N.T., Everitt, N.M., Ashcroft, I. and Tuck, C. (2014) 'Reducing porosity in AlSi10Mg parts processed by selective laser melting', *Additive Manufacturing*, 1-4, pp. 77-86. doi: 10.1016/j.addma.2014.08.001.

Amato, K.N., Gaytan, S.M., Murr, L.E., Martinez, E., Shindo, P.W., Hernandez, J., Collins, S. and Medina, F. (2012) 'Microstructures and mechanical behavior of Inconel 718 fabricated by selective laser melting', *Acta Materialia*, 60(5), pp. 2229-2239. doi: 10.1016/j.actamat.2011.12.032.

Biffi, C., Fiocchi, J., Bassani, P. and Tuissi, A. (September 11, 2019) *MICROSTRUCTURE AND MARTENSITIC TRANSFORMATION OF SELECTIVE LASER MELTED NiTi SHAPE MEMORY ALLOY PARTS.*

- Caputo, M.P., Berkowitz, A.E., Armstrong, A., Müllner, P. and Solomon, C.V. (2018) '4D printing of net shape parts made from Ni-Mn-Ga magnetic shape-memory alloys', *Additive Manufacturing*, 21, pp. 579-588. doi: 10.1016/j.addma.2018.03.028.
- Caputo, M. and Solomon, C. (2017) 'Microstructure and Chemical Composition Analysis of Additive Manufactured Ni-Mn-Ga Parts Sintered in Different Conditions', *Microscopy and Microanalysis*, 23, pp. 2078-2079. doi: 10.1017/S1431927617011059.
- Chmielus, M., Zhang, X.X., Witherspoon, C., Dunand, D.C. and Müllner, P. (2009) 'Giant magnetic-field-induced strains in polycrystalline Ni-Mn-Ga foams', *Nature Materials*, 8(11), pp. 863-866. doi: 10.1038/nmat2527.
- Engdahl, G. (2000) *Handbook of Giant Magnetostrictive Materials*. 1st edn. Academic Press.
- Gaitzsch, U., Pötschke, M., Roth, S., Rellinghaus, B. and Schultz, L. (2007) 'Mechanical training of polycrystalline 7M Ni<sub>50</sub>Mn<sub>30</sub>Ga<sub>20</sub> magnetic shape memory alloy', *Scripta Materialia*, 57, pp. 493-495. doi: 10.1016/j.scriptamat.2007.05.026.
- Hobza, A., Patrick, C.L., Ullakko, K., Rafla, N., Lindquist, P. and Müllner, P. (2018) 'Sensing strain with Ni-Mn-Ga', *Sensors and Actuators A: Physical*, 269, pp. 137-144. doi: 10.1016/j.sna.2017.11.002.
- Houck, M.M. (2013) 'Microscopy (Electron)', in Siegel, J.A., Saukko, P.J. and Houck, M.M. (eds.) *Encyclopedia of Forensic Sciences (Second Edition)* Waltham: Academic Press, pp. 612-615.
- Jin, X., Marioni, M., Bono, D., Allen, S.M., O'Handley, R.C. and Hsu, T.Y. (2002) 'Empirical mapping of Ni-Mn-Ga properties with composition and valence electron concentration', *Journal of Applied Physics*, 91(10), pp. 8222-8224. doi: 10.1063/1.1453943.
- Karaman, I., Basaran, B., Karaca, H.E., Karsilayan, A.I. and Chumlyakov, Y.I. (2007) 'Energy harvesting using martensite variant reorientation mechanism in a NiMnGa magnetic shape memory alloy', *Applied Physics Letters*, 90(17), pp. 172505. doi: 10.1063/1.2721143.
- Kempen, K., Vrancken, B., Buls, S., Thijs, L., Humbeeck, J. and Kruth, J. (2014) 'Selective Laser Melting of Crack-Free High Density M2 High Speed Steel Parts by Baseplate Preheating', *Journal of Manufacturing Science and Engineering*, 136. doi: 10.1115/1.4028513.
- Kruth, J., Deckers, J., Yasa, E. and Wauthle, R. (2012) 'Assessing and comparing influencing factors of residual stresses in selective laser melting using a novel analysis method', *Proceedings of the Institution of Mechanical Engineers, Part B: Journal of Engineering Manufacture*, 226, pp. 980-991. doi: 10.1177/0954405412437085.
- Laitinen, V. (2021) *Laser powder bed fusion for the manufacture of Ni-Mn-Ga magnetic shape memory alloy actuators*. Lappeenranta-Lahti University of Technology LUT.

- Laitinen, V., Merabtene, M., Stevens, E., Chmielus, M., Humbeeck, J. and Ullakko, K. (2020) 'Additive Manufacturing from the Point of View of Materials Research', pp. 43-83.
- Laitinen, V., Salminen, A. and Ullakko, K. (2019) 'First investigation on processing parameters for laser powder bed fusion of Ni-Mn-Ga magnetic shape memory alloy', *Journal of Laser Applications*, 31, pp. 022303. doi: 10.2351/1.5096108.
- Laitinen, V., Saren, A., Sozinov, A. and Ullakko, K. (2022) 'Giant 5.8% magnetic-field-induced strain in additive manufactured Ni-Mn-Ga magnetic shape memory alloy', *Scripta Materialia*, 208, pp. 114324. doi: 10.1016/j.scriptamat.2021.114324.
- Laitinen, V., Sozinov, A., Saren, A., Chmielus, M. and Ullakko, K. (2021) 'Characterization of as-built and heat-treated Ni-Mn-Ga magnetic shape memory alloy manufactured via laser powder bed fusion', *Additive Manufacturing*, 39, pp. 101854. doi: 10.1016/j.addma.2021.101854.
- Laitinen, V., Sozinov, A., Saren, A., Salminen, A. and Ullakko, K. (2019) 'Laser powder bed fusion of Ni-Mn-Ga magnetic shape memory alloy', *Additive Manufacturing*, 30, pp. 100891. doi: 10.1016/j.addma.2019.100891.
- Lanska, N., Söderberg, O., Sozinov, A., Ge, Y., Ullakko, K. and Lindroos, V.K. (2004) 'Composition and temperature dependence of the crystal structure of Ni-Mn-Ga alloys', *Journal of Applied Physics*, 95(12), pp. 8074-8078. doi: 10.1063/1.1748860.
- Li, C., Liu, J.F. and Guo, Y.B. (2016) 'Prediction of Residual Stress and Part Distortion in Selective Laser Melting', *Procedia CIRP*, 45, pp. 171-174. doi: 10.1016/j.procir.2016.02.058.
- Likhachev, A.A. and Ullakko, K. (2000) 'Quantitative Model of Large Magnetostrain Effect in Ferromagnetic Shape Memory Alloys', *EPJ direct*, 1(1), pp. 1-9. doi: 10.1007/s1010599b0002.
- Lloyd-Jones Graham (2016) *Basics of X-ray Physics - X-ray production*. Available at: [https://www.radiologymasterclass.co.uk/tutorials/physics/x-ray\\_physics\\_production#top\\_2nd\\_img](https://www.radiologymasterclass.co.uk/tutorials/physics/x-ray_physics_production#top_2nd_img) (Accessed: October 2021).
- Louvis, E., Fox, P. and Sutcliffe, C.J. (2011) 'Selective laser melting of aluminium components', *Journal of Materials Processing Technology*, 211(2), pp. 275-284. doi: 10.1016/j.jmatprotec.2010.09.019.
- Luke, K. and Silva, A. (January 1, 2013) *Advances in Particle Characterization - Benefits and Applications*. pp. 1.
- Martynov, V.V. (1995) 'X-ray diffraction study of thermally and stress-induced phase transformations in single crystalline Ni-Mn-Ga alloys', *Journal de Physique 4*, 5(8), pp. 91-99.

- Martynov, V.V. and Kokorin, V.V. (1992) 'The crystal structure of thermally- and stress-induced Martensites in Ni<sub>2</sub>MnGa single crystals', *Journal de Physique III*, 2(5), pp. 739-749. doi: 10.1051/jp3:1992155.
- Mayer Daniel. (2007) *Crystal structures* [0]. Available at: (Accessed: Nov 2021)
- Mercelis, P. and Kruth, J. (2006) 'Residual stresses in selective laser sintering and selective laser melting', *Rapid Prototyping Journal*, 12. doi: 10.1108/13552540610707013.
- Mostafaei, A., Kimes, K., Stevens, E., Toman, J., Krimer, Y., Ullakko, K. and Chmielus, M. (2017) 'Microstructural evolution and magnetic properties of binder jet additive manufactured Ni-Mn-Ga magnetic shape memory alloy foam', *Acta Materialia*, 131. doi: 10.1016/j.actamat.2017.04.010.
- Murray, S.J., Marioni, M., Allen, S.M., O'Handley, R.C. and Lograsso, T.A. (2000) '6% magnetic-field-induced strain by twin-boundary motion in ferromagnetic Ni-Mn-Ga', *Applied Physics Letters*, 77(6), pp. 886-888. doi: 10.1063/1.1306635.
- Nasrazadani, S. and Hassani, S. (2016) 'Chapter 2 - Modern analytical techniques in failure analysis of aerospace, chemical, and oil and gas industries', in Makhoulouf, A.S.H. and Aliofkhaezraei, M. (eds.) *Handbook of Materials Failure Analysis with Case Studies from the Oil and Gas Industry* Butterworth-Heinemann, pp. 39-54.
- Overholser, R.W., Wuttig, M. and Neumann, D.A. (1999) 'Chemical ordering in Ni-Mn-Ga Heusler alloys', *Scripta Materialia*, 40(10), pp. 1095-1102. doi: 10.1016/S1359-6462(99)00080-9.
- Pons, J., Chernenko, V.A., Santamarta, R. and Cesari, E. (2000) 'Crystal structure of martensitic phases in Ni-Mn-Ga shape memory alloys', *Acta Materialia*, 48(12), pp. 3027-3038. doi: 10.1016/S1359-6454(00)00130-0.
- Pötschke, M., Gaitzsch, U., Roth, S., Rellinghaus, B. and Schultz, L. (2007) 'Preparation of melt textured Ni-Mn-Ga', *Journal of Magnetism and Magnetic Materials*, 316, pp. 383-385. doi: 10.1016/j.jmmm.2007.03.032.
- Qiu, C., Adkins, N.J.E. and Attallah, M.M. (2013) 'Microstructure and tensile properties of selectively laser-melted and of HIPed laser-melted Ti-6Al-4V', *Materials Science & Engineering A*, 578(Complete), pp. 230-239. doi: 10.1016/j.msea.2013.04.099.
- Ripoll Martín Martínez *Scattering and diffraction. The Bragg's Law*. Available at: [https://www.xtal.iqfr.csic.es/Cristalografia/parte\\_05\\_5-en.html](https://www.xtal.iqfr.csic.es/Cristalografia/parte_05_5-en.html) (Accessed: October 2021).
- Roberts, I.A., Wang, C.J., Esterlein, R., Stanford, M. and Mynors, D.J. (2009) 'A three-dimensional finite element analysis of the temperature field during laser melting of metal powders in additive layer manufacturing', *International Journal of Machine Tools and Manufacture*, 49(12), pp. 916-923. doi: 10.1016/j.ijmachtools.2009.07.004.
- Saren, A., Musiienko, D., Smith, A.R. and Ullakko, K. (2016) 'Pulsed magnetic field-induced single twin boundary motion in Ni-Mn-Ga 5M martensite: A laser vibrometry

characterization', *Scripta Materialia*, 113, pp. 154-157. doi: 10.1016/j.scriptamat.2015.10.020.

Saren, A., Musiienko, D., Smith, A., Tellinen, J. and Ullakko, K. (2015) 'Modeling and design of a vibration energy harvester using the magnetic shape memory effect', *Smart Materials and Structures*, 24. doi: 10.1088/0964-1726/24/9/095002.

Schlagel, D.L., Wu, Y.L., Zhang, W. and Lograsso, T.A. (2000) 'Chemical segregation during bulk single crystal preparation of Ni–Mn–Ga ferromagnetic shape memory alloys', *Journal of Alloys and Compounds*, 312(1), pp. 77-85. doi: 10.1016/S0925-8388(00)01161-0.

Söderberg, O., Ge, Y., Sozinov, A., Hannula, S. and Lindroos, V. (2005) 'Recent Breakthrough Development of the Magnetic Shape Memory Effect in Ni–Mn–Ga Alloys', *Smart Materials and Structures*, 14, pp. S223. doi: 10.1088/0964-1726/14/5/009.

Sonawane, A., Roux, G., Blandin, J., Despres, A. and Martin, G. (2021) 'Cracking mechanism and its sensitivity to processing conditions during laser powder bed fusion of a structural aluminum alloy', *Materialia*, 15, pp. 100976. doi: 10.1016/j.mtla.2020.100976.

Sozinov, A., Likhachev, A.A., Lanska, N. and Ullakko, K. (2002) 'Giant magnetic-field-induced strain in NiMnGa seven-layered martensitic phase', *Applied Physics Letters*, 80(10), pp. 1746-1748. doi: 10.1063/1.1458075.

Stephan, J.M., Pagounis, E., Laufenberg, M., Paul, O. and Ruther, P. (2011) 'A Novel Concept for Strain Sensing Based on the Ferromagnetic Shape Memory Alloy NiMnGa', *IEEE Sensors Journal*, 11(11), pp. 2683-2689. doi: 10.1109/JSEN.2011.2157489.

Stevens, E., Toman, J., Kimes, K., Chernenko, V., Wójcik, A., Maziarz, W. and Chmielus, M. (2016) 'Microstructural Evaluation of Magnetocaloric Ni-Co-Mn-Sn Produced by Directed Energy Deposition', *Microscopy and Microanalysis*, 22, pp. 1774-1775. doi: 10.1017/S1431927616009715.

Straka, L., Heczko, O., Seiner, H., Lanska, N., Drahokoupil, J., Soroka, A., Fähler, S., Hänninen, H. and Sozinov, A. (2011) 'Highly mobile twinned interface in 10M modulated Ni–Mn–Ga martensite: Analysis beyond the tetragonal approximation of lattice', *Acta Materialia*, 59(20), pp. 7450-7463. doi: 10.1016/j.actamat.2011.09.020.

Suorsa, I., Tellinen, J., Ullakko, K. and Pagounis, E. (2004) 'Voltage generation induced by mechanical straining in magnetic shape memory materials', *Journal of Applied Physics*, 95(12), pp. 8054-8058. doi: 10.1063/1.1711181.

Taylor, S., Shah, R. and Dunand, D. (2017) 'Ni-Mn-Ga Micro-trusses via Sintering of 3D-printed Inks Containing Elemental Powders', *Acta Materialia*, 143. doi: 10.1016/j.actamat.2017.10.002.

Tellinen, J., Suorsa, I., Jääskeläinen, A., Aaltio, I., Ullakko, K. and Ltd, A. (2002) 'Basic properties of magnetic shape memory actuators', *Proc. of 8th Int. Conf. on Actuator*, .

Thijs, L., Vrancken, B., Kruth, J.P. and Humbeeck, J.V. (2013) *Materials Science and Technology Conference and Exhibition 2013, MS and T*.

Ullakko, K. (1996) 'Magnetically controlled shape memory alloys: A new class of actuator materials', *Journal of Materials Engineering and Performance*, 5(3), pp. 405-409. doi: 10.1007/BF02649344.

Ullakko, K., Ezer, Y., Sozinov, A., Kimmel, G., Yakovenko, P. and Lindroos, V. (2001) 'Magnetic-field-induced strains in polycrystalline Ni-Mn-Ga at room temperature', *Scripta Materialia - SCRIPTA MATER*, 44, pp. 475-480. doi: 10.1016/S1359-6462(00)00610-2.

Ullakko, K., Huang, J.K., Kantner, C., O'Handley, R.C. and Kokorin, V.V. (1996) 'Large magnetic-field-induced strains in Ni<sub>2</sub>MnGa single crystals', *Applied Physics Letters*, 69(13), pp. 1966-1968. doi: 10.1063/1.117637.

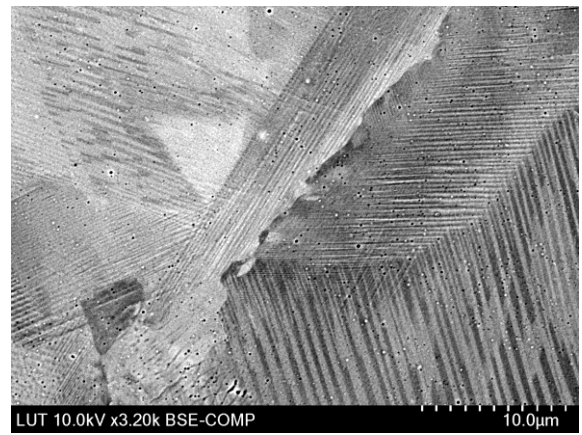
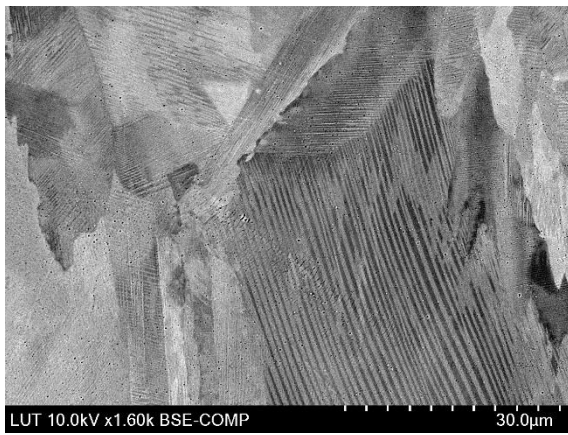
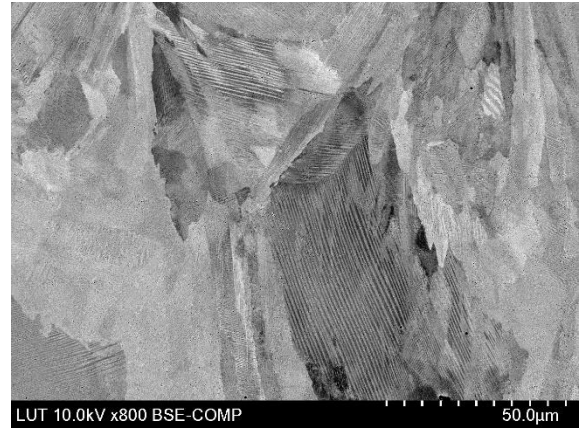
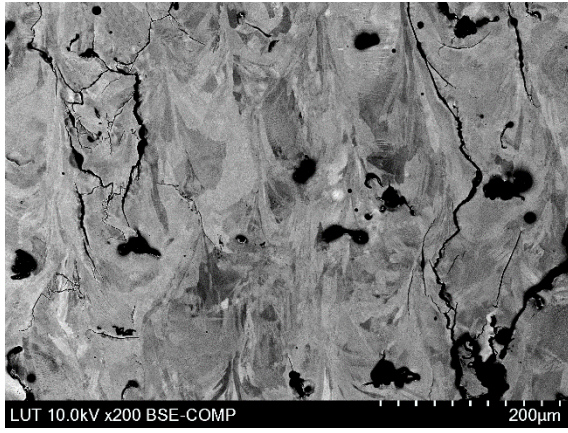
Vasil'ev, A., Bozhko, A., Khovailo, V., Dikshtein, I., Shavrov, V., Seletskii, S. and Buchelnikov, V. (1999) 'Structural and magnetic phase transitions in shape memory alloys Ni<sub>2</sub> + XMn<sub>1-x</sub>Ga', *Journal of Magnetism and Magnetic Materials*, 196-197, pp. 837-839. doi: 10.1016/S0304-8853(98)00964-0.

Vecchiato, F.L., de Winton, H., Hooper, P.A. and Wenman, M.R. (2020) 'Melt pool microstructure and morphology from single exposures in laser powder bed fusion of 316L stainless steel', *Additive Manufacturing*, 36, pp. 101401. doi: 10.1016/j.addma.2020.101401.

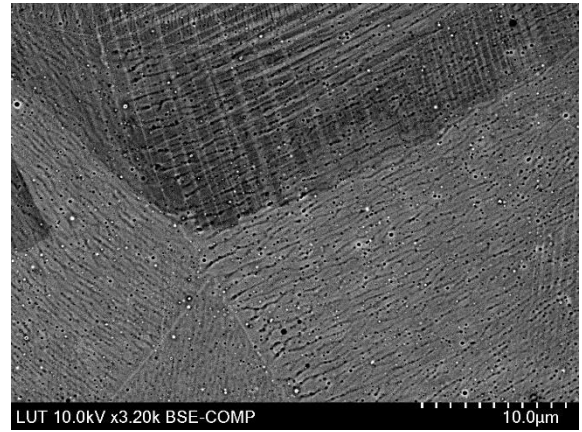
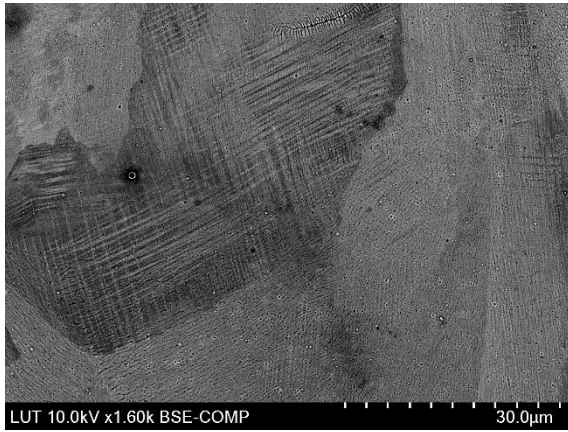
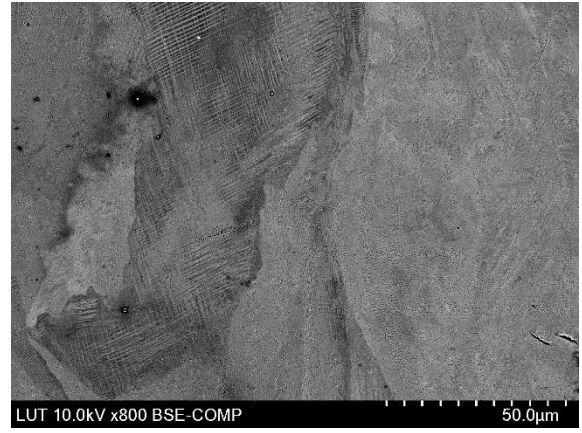
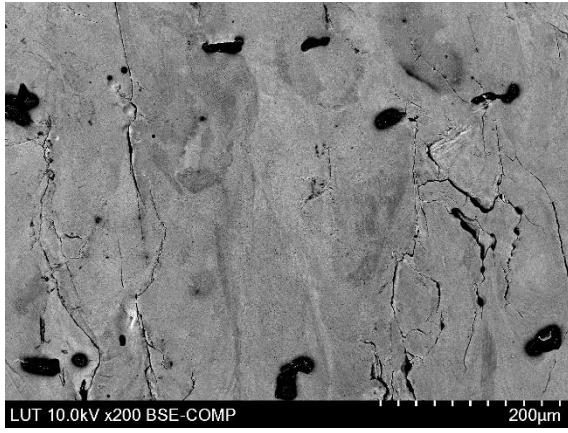
Vrancken, B., Cain, V., Knutsen, R. and Van Humbeeck, J. (2014) 'Residual stress via the contour method in compact tension specimens produced via selective laser melting', *Scripta Materialia*, 87, pp. 29-32. doi: 10.1016/j.scriptamat.2014.05.016.

Webster, P.J., Ziebeck, K.R.A., Town, S.L. and Peak, M.S. (1984) 'Magnetic order and phase transformation in Ni<sub>2</sub>MnGa', *Philosophical Magazine B*, 49(3), pp. 295-310. doi: 10.1080/13642817408246515.

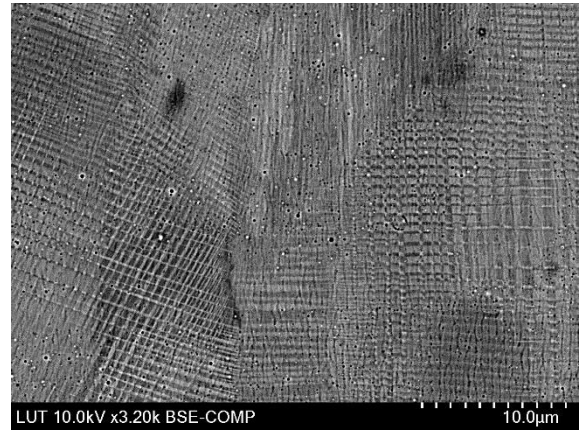
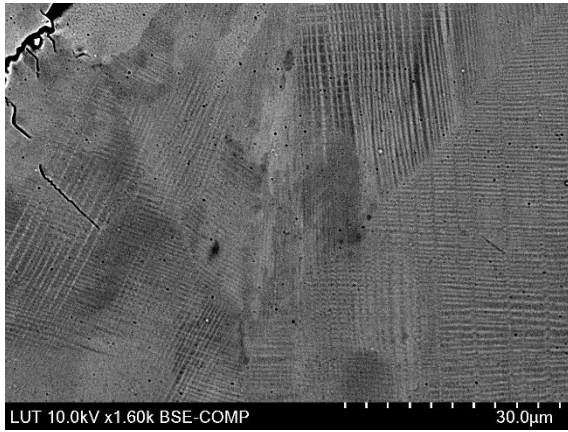
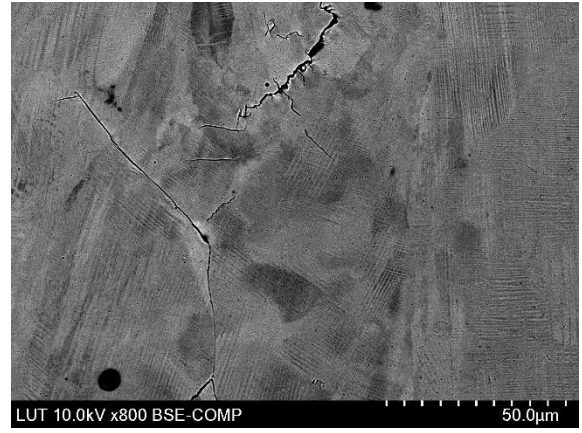
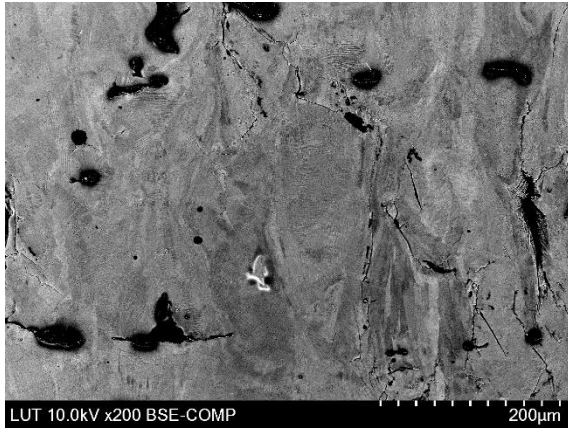
APPENDIX I, 1  
SEM images  
S1AB



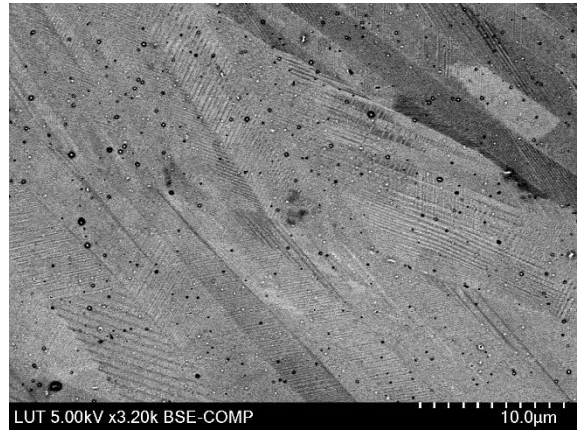
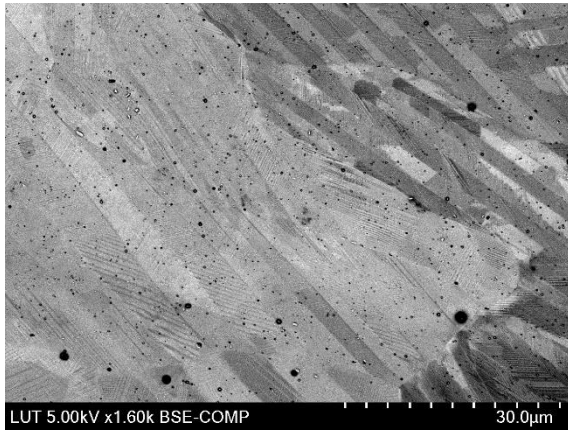
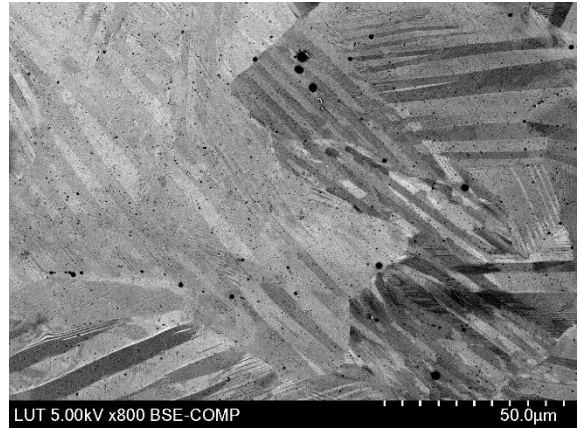
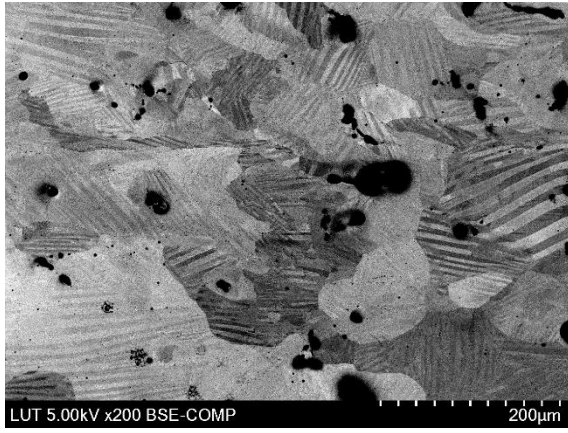
APPENDIX I, 2  
SEM images  
S2AB



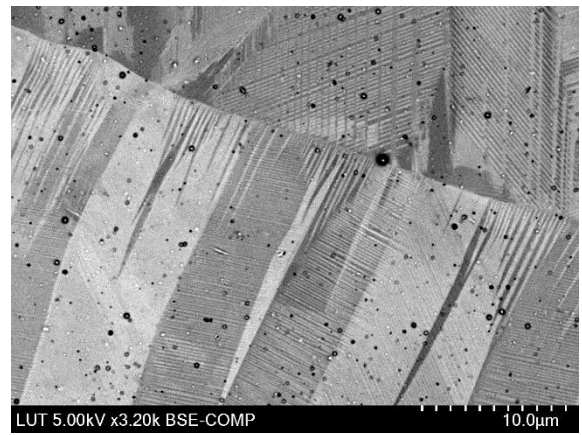
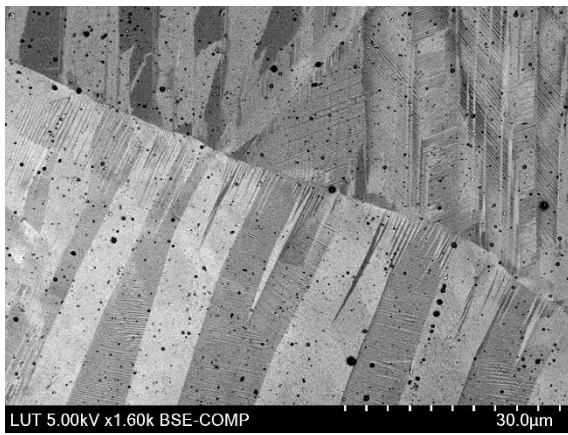
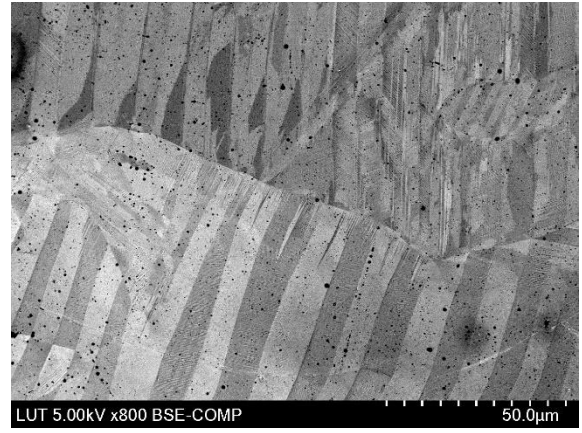
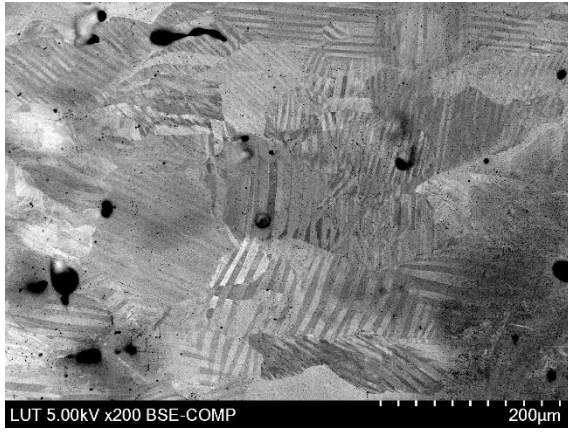
APPENDIX I, 3  
SEM images  
S3AB



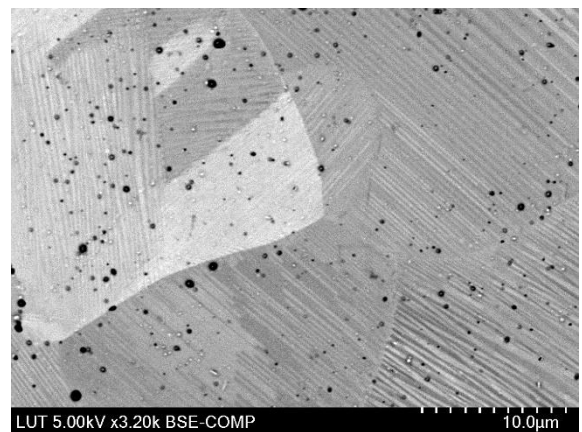
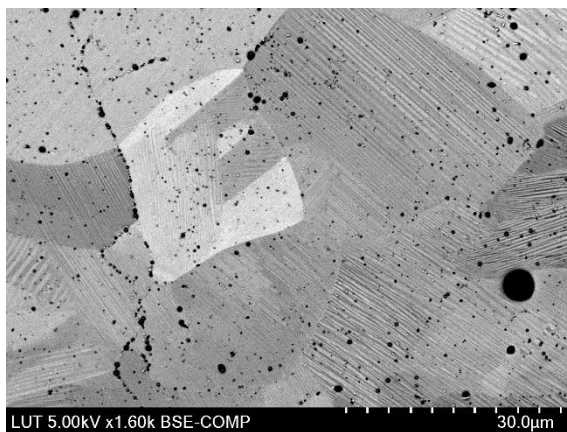
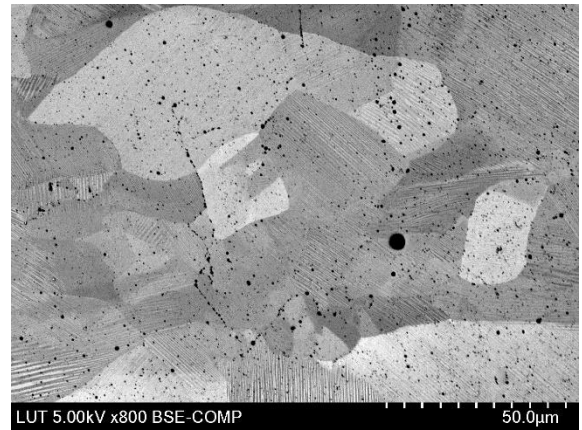
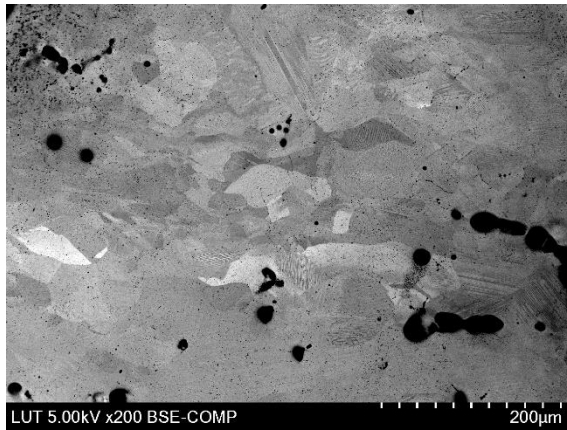
APPENDIX I, 4  
SEM images  
S1HT



APPENDIX I, 5  
SEM images  
S2HT

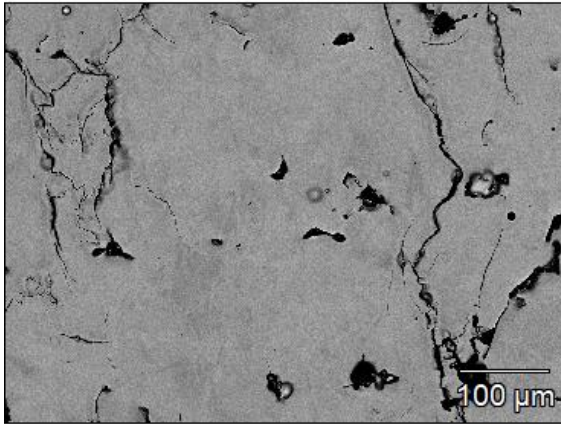


APPENDIX I, 6  
SEM images  
S3HT

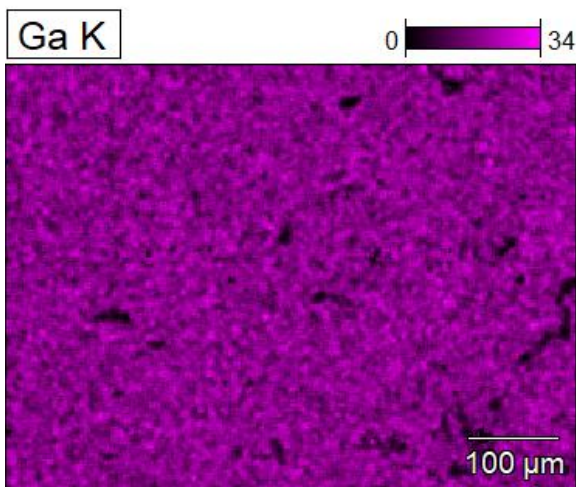
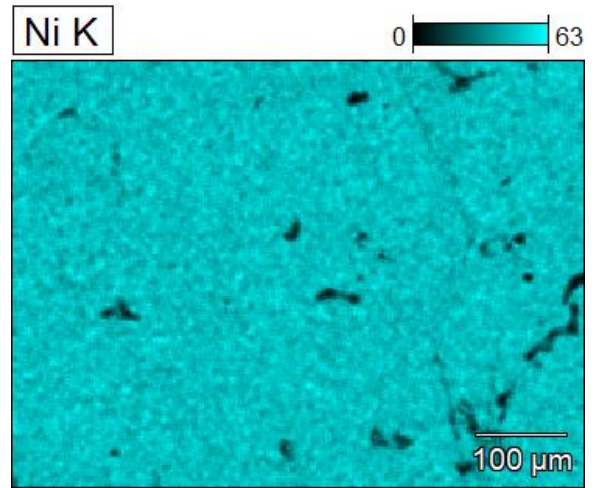
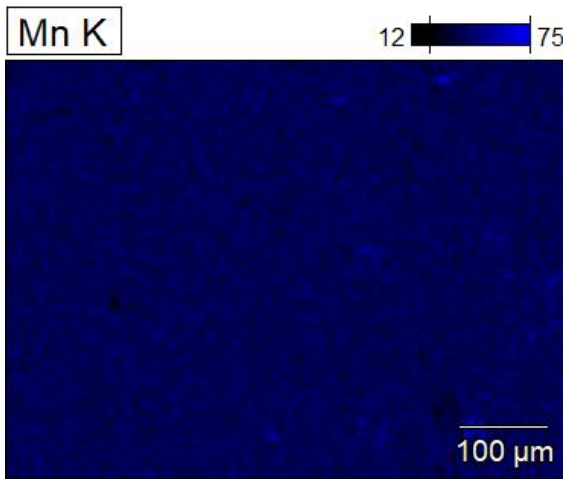


APPENDIX II, 1  
EDS images  
S1AB at 200x magnification

S1(1)

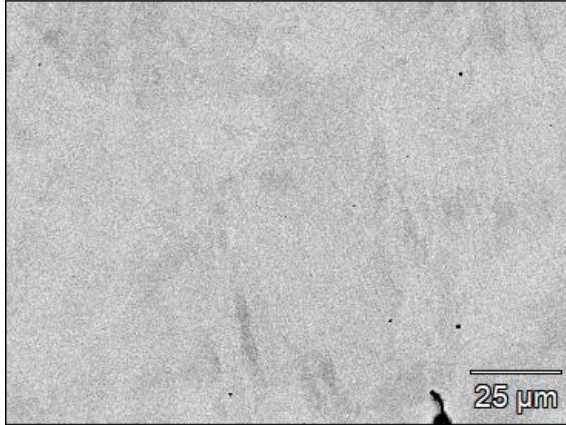


Data Type:	Atomic %
Image Resolution:	1024 by 768
Image Pixel Size:	0.62 μm
Map Resolution:	256 by 192
Map Pixel Size:	2.47 μm
Acc. Voltage:	20.0 kV
Magnification:	200

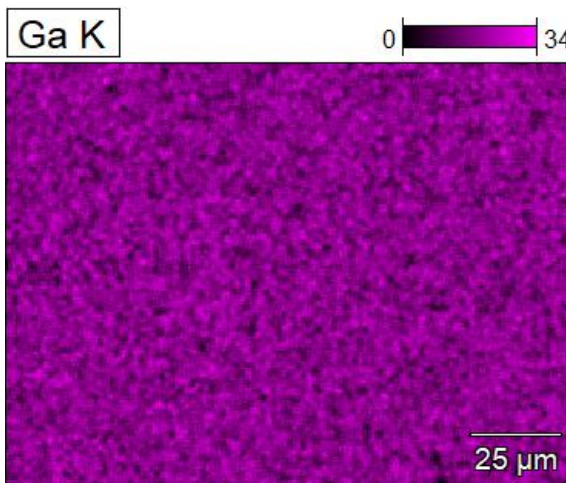
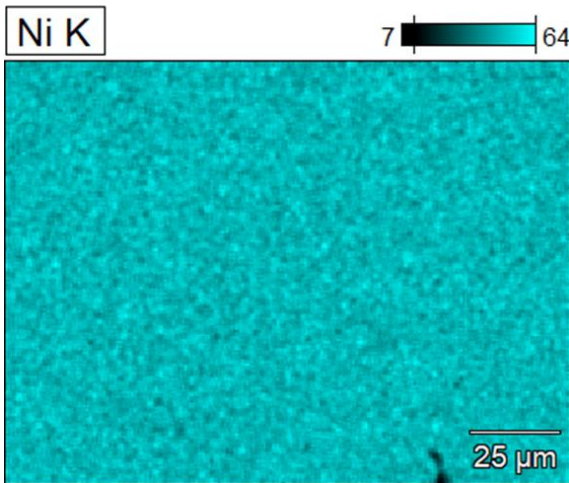
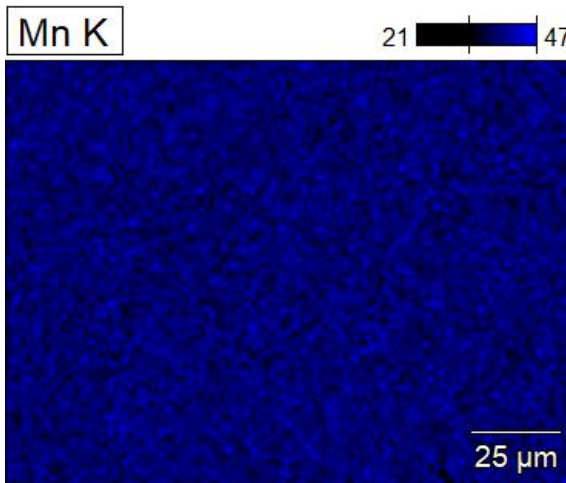


APPENDIX II, 2  
EDS images  
S1AB at 800x magnification

S1(2)

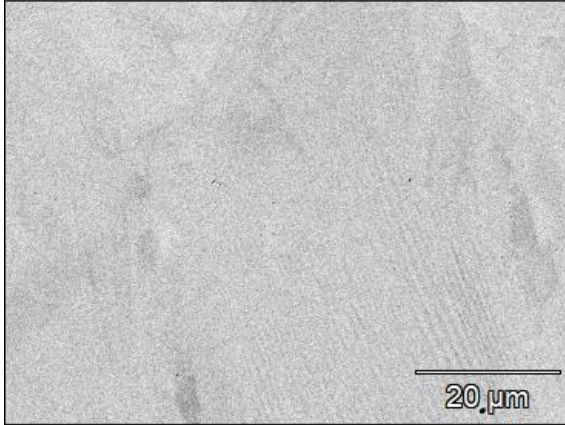


Data Type:	Atomic %
Image Resolution:	1024 by 768
Image Pixel Size:	0.15 μm
Map Resolution:	256 by 192
Map Pixel Size:	0.62 μm
Acc. Voltage:	20.0 kV
Magnification:	800

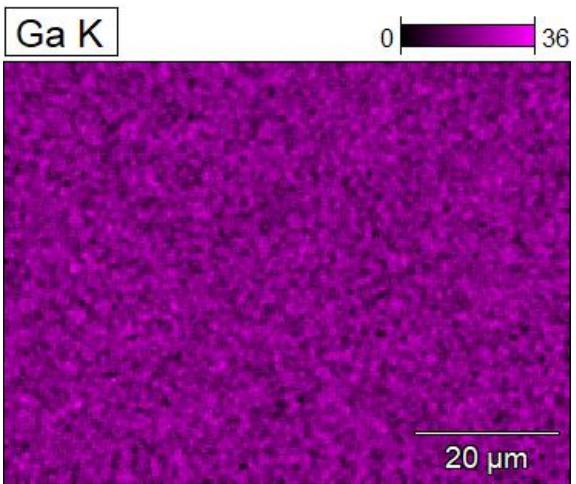
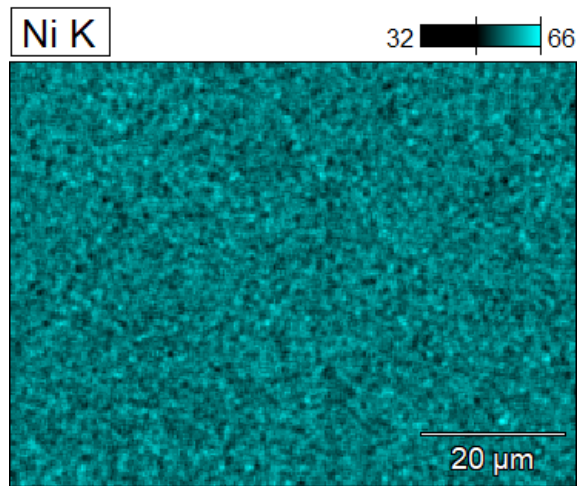
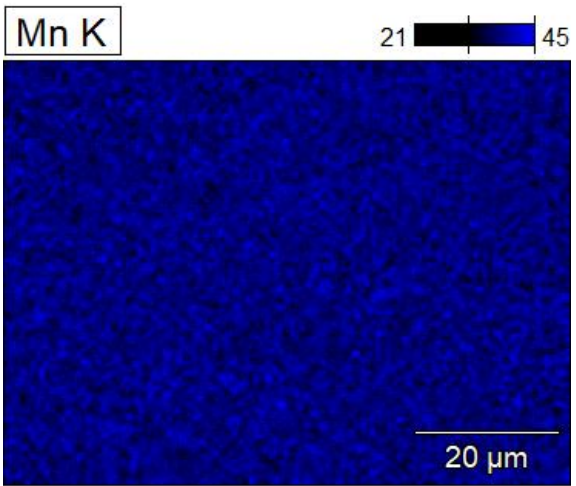


APPENDIX II, 3  
EDS images  
S1AB at 1600x magnification

S1(3)

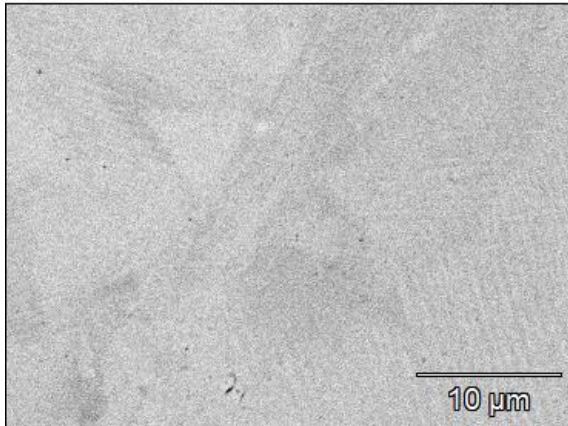


Data Type:	Atomic %
Image Resolution:	1024 by 768
Image Pixel Size:	0.08 μm
Map Resolution:	256 by 192
Map Pixel Size:	0.31 μm
Acc. Voltage:	20.0 kV
Magnification:	1600

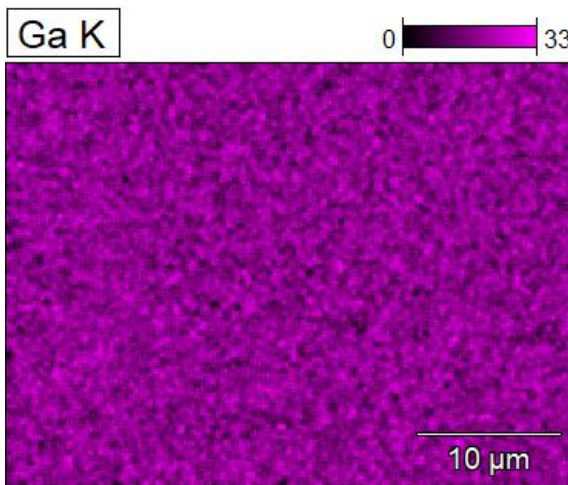
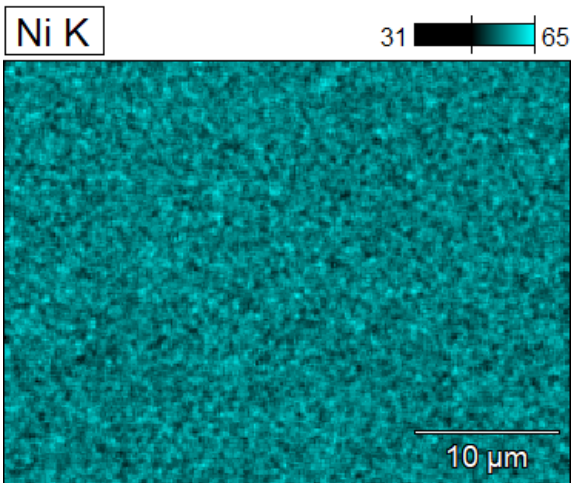
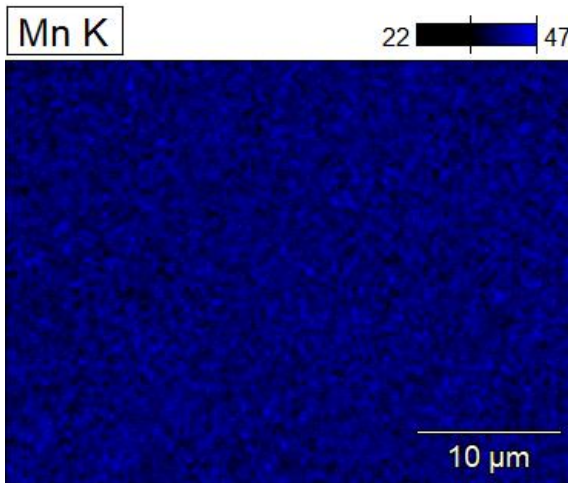


APPENDIX II, 4  
EDS images  
S1AB at 3200x magnification

S1(4)

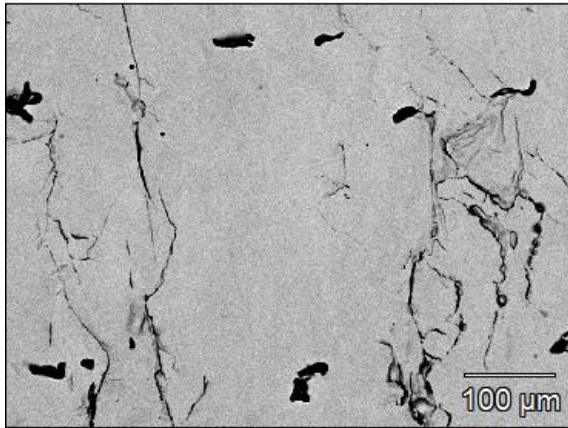


Data Type:	Atomic %
Image Resolution:	1024 by 768
Image Pixel Size:	0.04 μm
Map Resolution:	256 by 192
Map Pixel Size:	0.15 μm
Acc. Voltage:	20.0 kV
Magnification:	3200

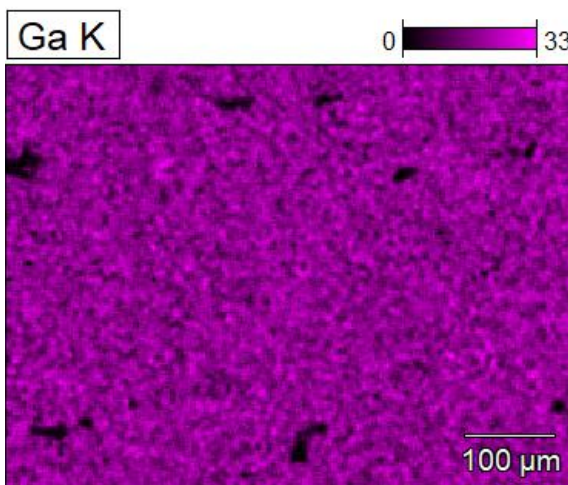
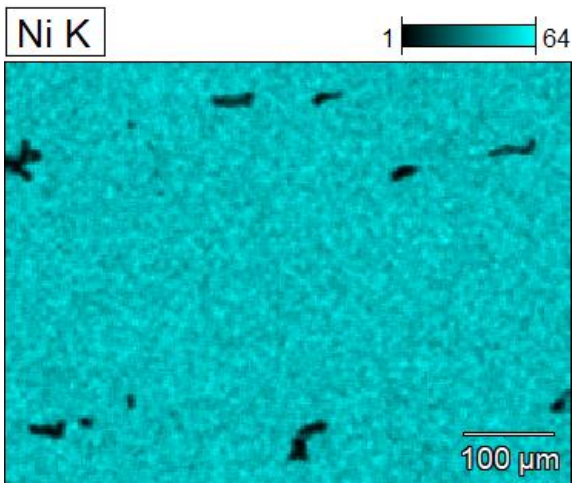
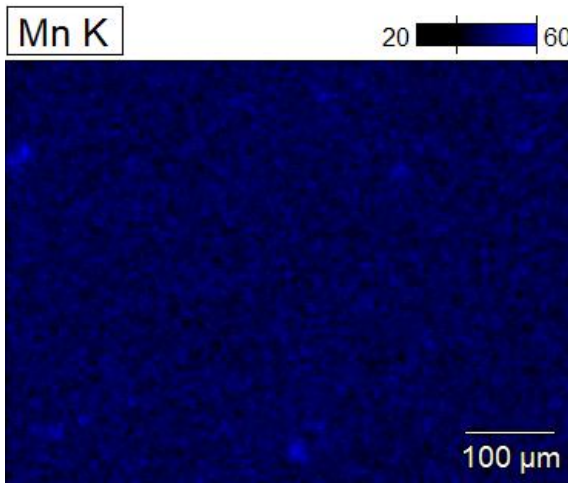


APPENDIX II, 5  
EDS images  
S2AB at 200x magnification

S2(1)

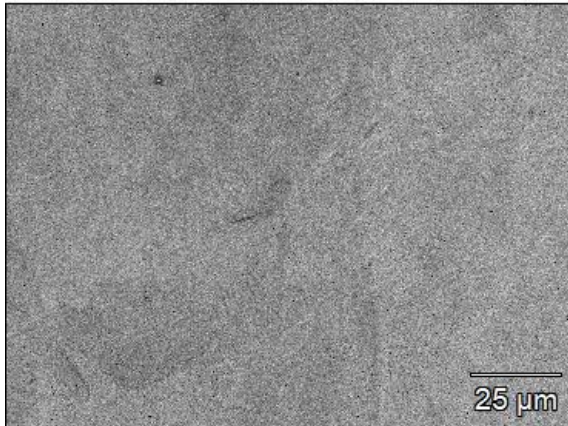


Data Type:	Atomic %
Image Resolution:	1024 by 768
Image Pixel Size:	0.62 μm
Map Resolution:	256 by 192
Map Pixel Size:	2.47 μm
Acc. Voltage:	20.0 kV
Magnification:	200

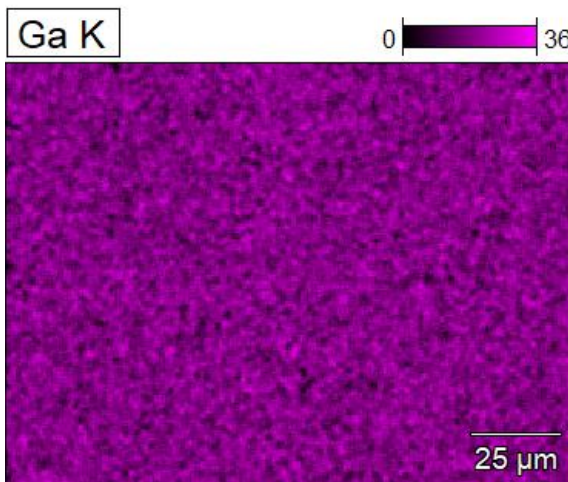
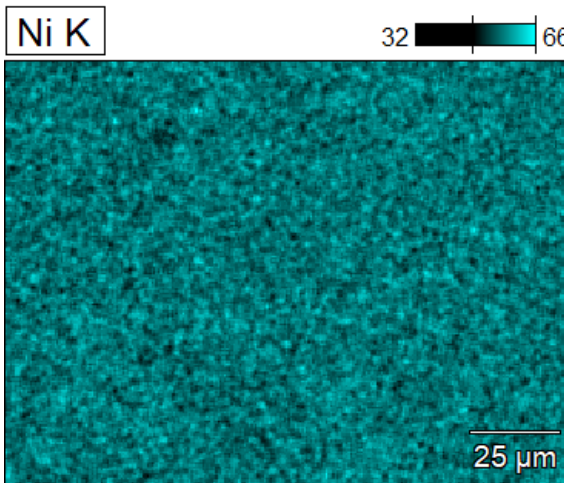
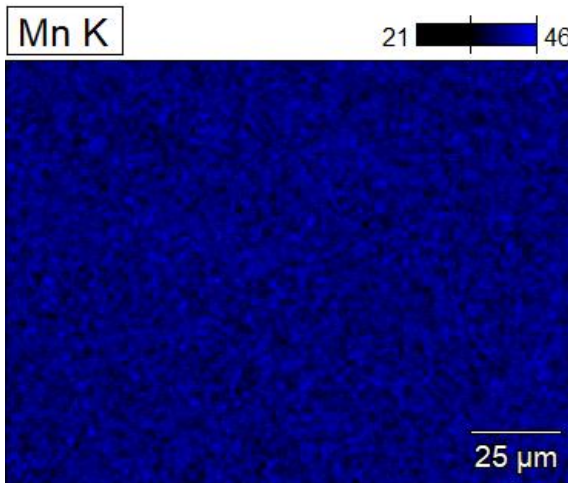


APPENDIX II, 6  
EDS images  
S2AB at 800x magnification

S2(2)

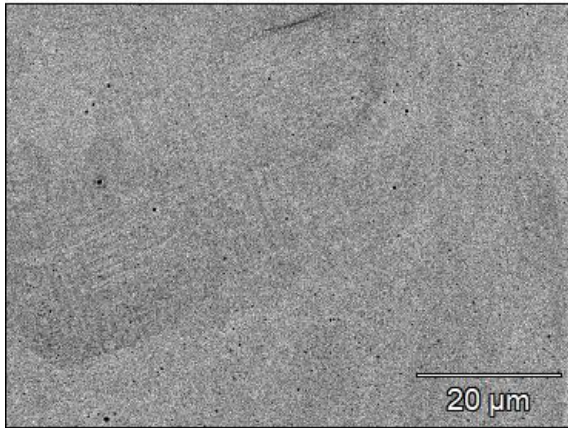


Data Type:	Atomic %
Image Resolution:	1024 by 768
Image Pixel Size:	0.15 μm
Map Resolution:	256 by 192
Map Pixel Size:	0.62 μm
Acc. Voltage:	20.0 kV
Magnification:	800

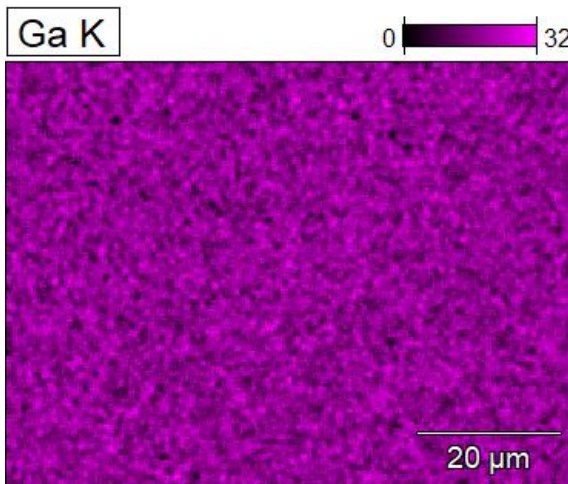
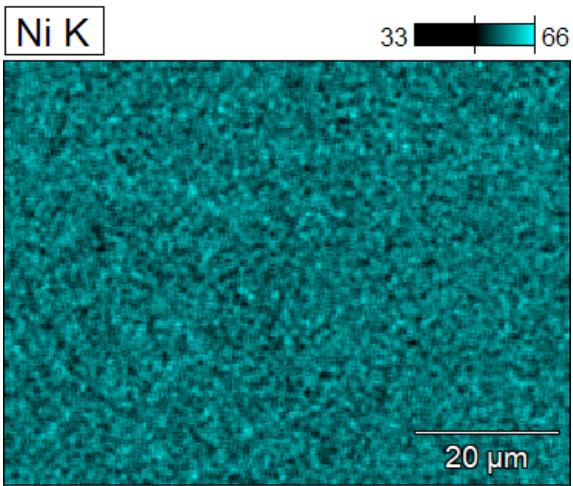
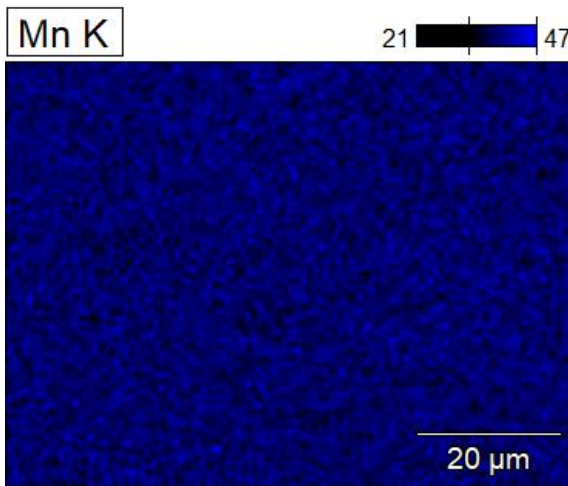


APPENDIX II, 7  
EDS images  
S2AB at 1600x magnification

S2(3)

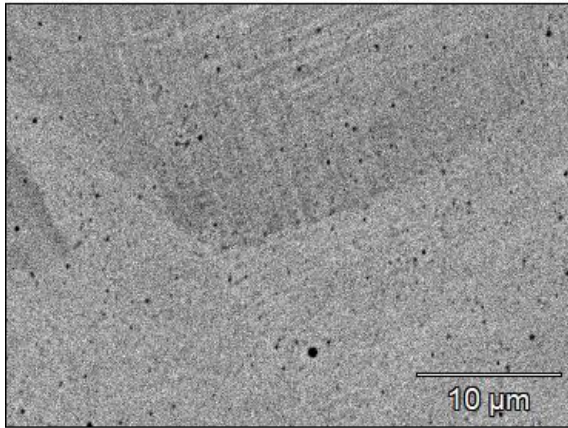


Data Type:	Atomic %
Image Resolution:	1024 by 768
Image Pixel Size:	0.08 μm
Map Resolution:	256 by 192
Map Pixel Size:	0.31 μm
Acc. Voltage:	20.0 kV
Magnification:	1600

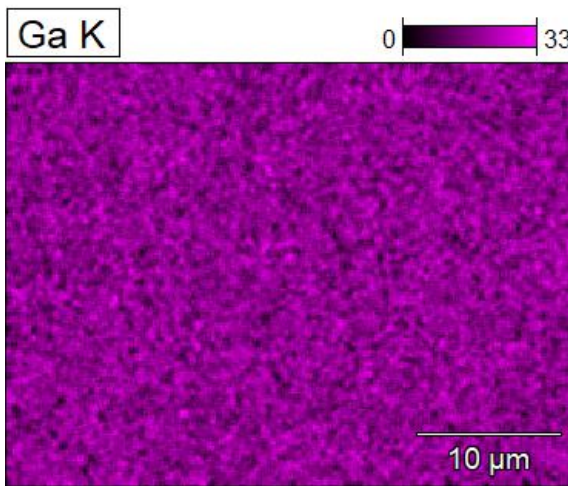
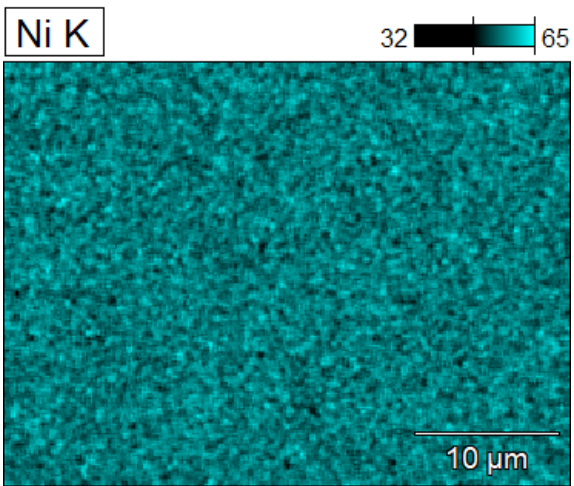
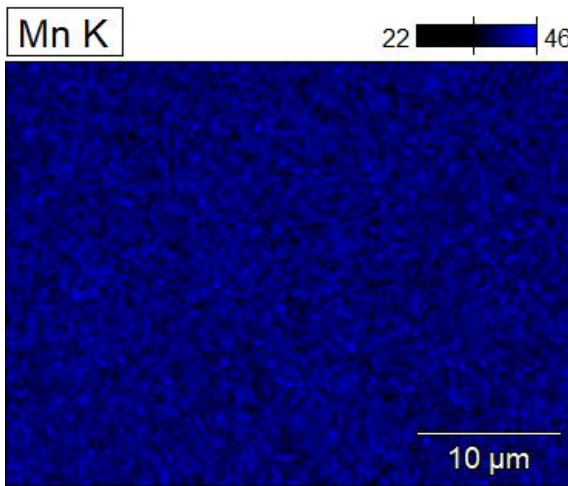


APPENDIX II, 8  
EDS images  
S2AB at 3200x magnification

S2(5)

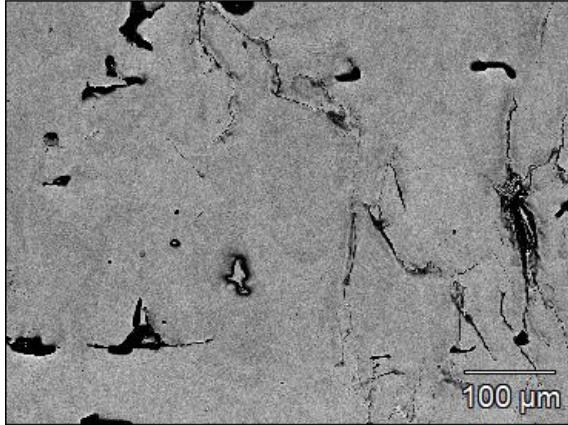


Data Type:	Atomic %
Image Resolution:	1024 by 768
Image Pixel Size:	0.04 μm
Map Resolution:	256 by 192
Map Pixel Size:	0.15 μm
Acc. Voltage:	20.0 kV
Magnification:	3200

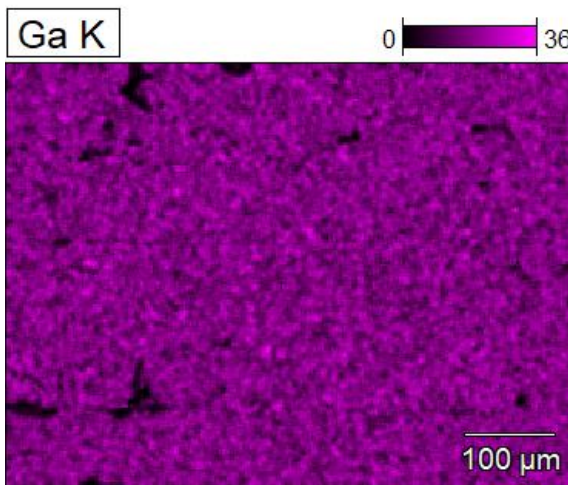
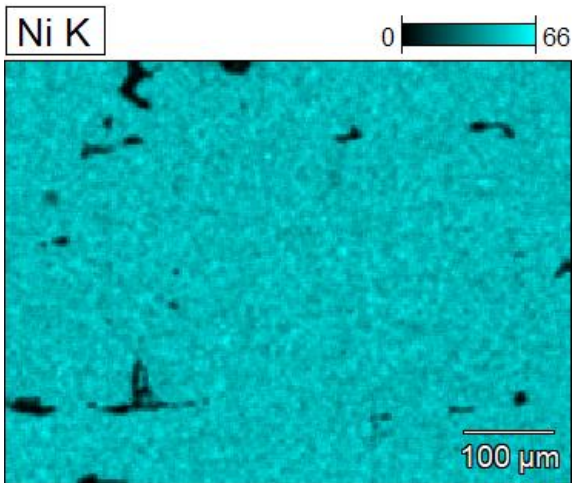
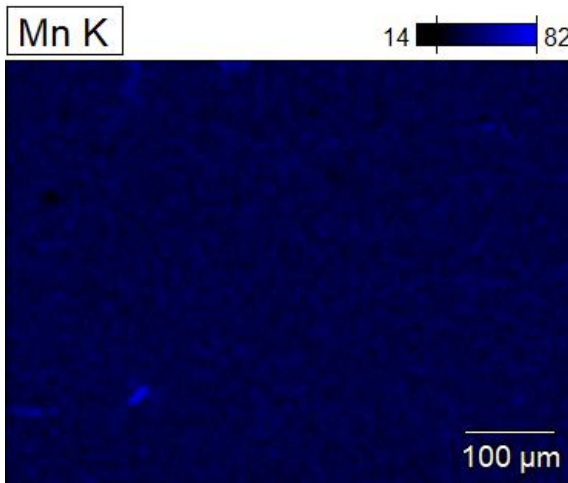


APPENDIX II, 9  
EDS images  
S3AB at 200x magnification

S3(1)

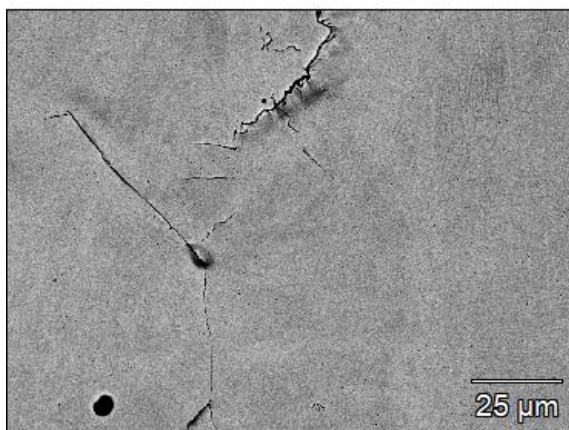


Data Type:	Atomic %
Image Resolution:	1024 by 768
Image Pixel Size:	0.62 μm
Map Resolution:	256 by 192
Map Pixel Size:	2.47 μm
Acc. Voltage:	20.0 kV
Magnification:	200

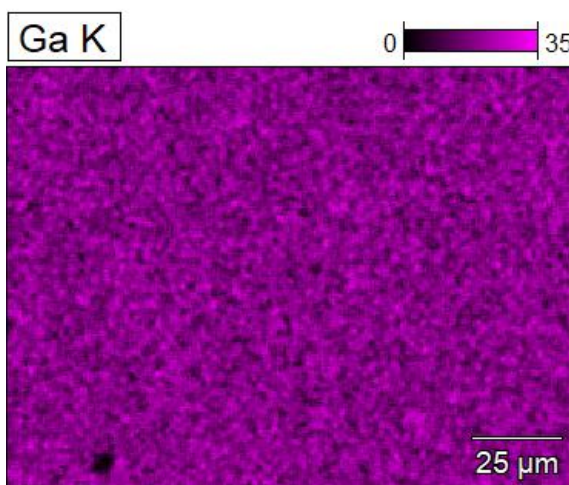
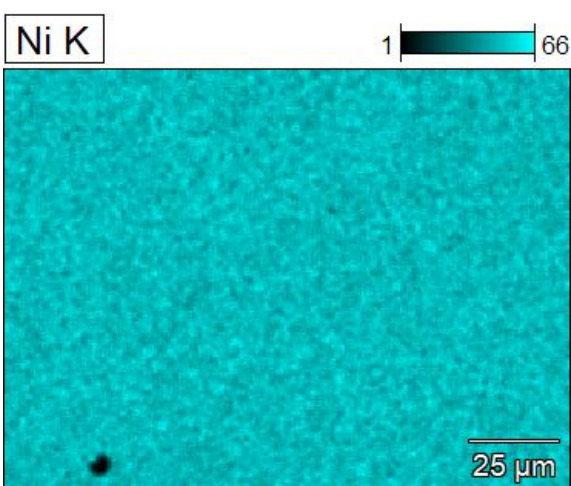
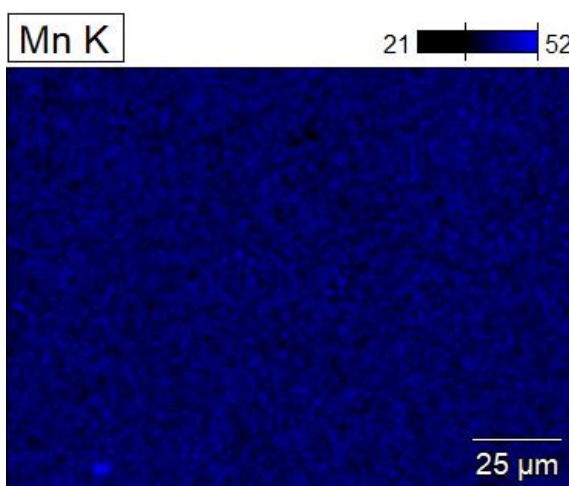


APPENDIX II, 10  
EDS images  
S3AB at 800x magnification

S3(2)

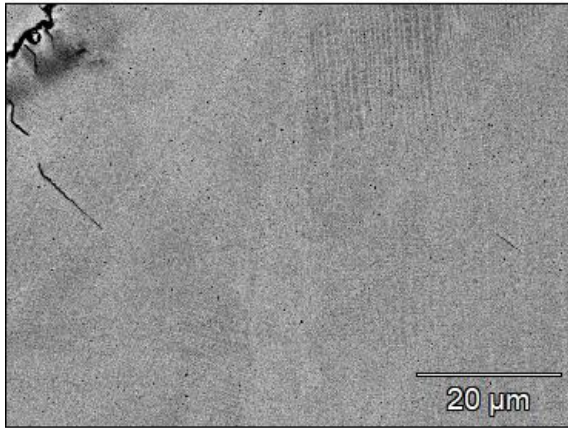


Data Type: Atomic %  
Image Resolution: 1024 by 768  
Image Pixel Size: 0.15 μm  
Map Resolution: 256 by 192  
Map Pixel Size: 0.62 μm  
Acc. Voltage: 20.0 kV  
Magnification: 800

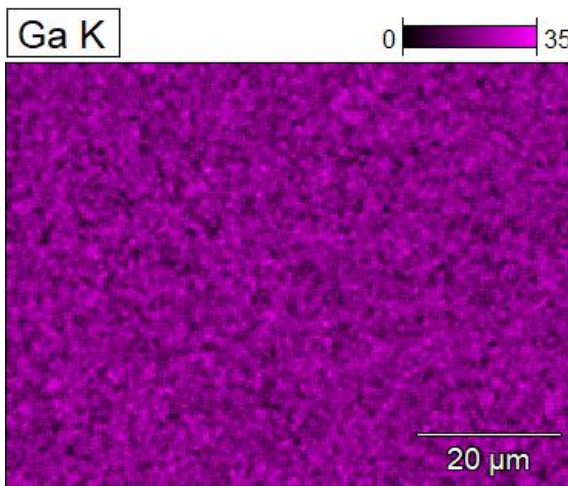
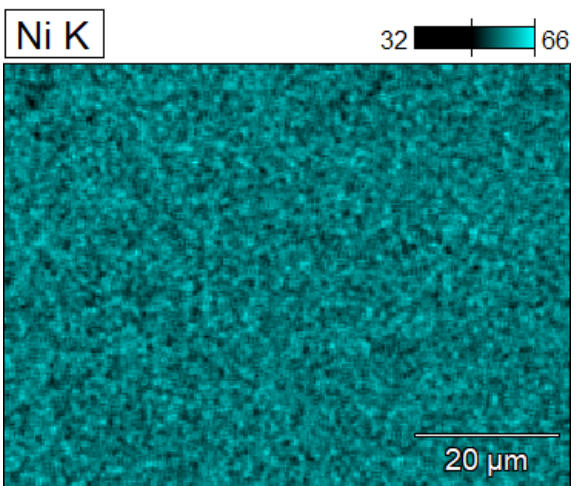
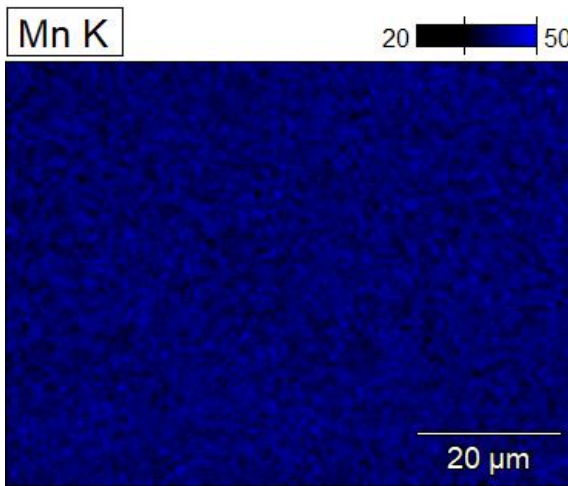


APPENDIX II, 11  
EDS images  
S3AB at 1600x magnification

S3(3)

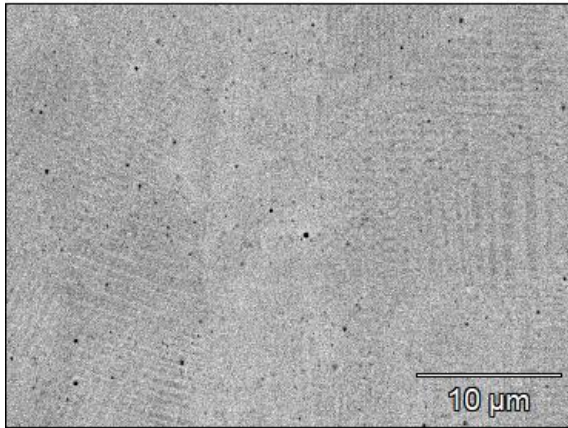


Data Type:	Atomic %
Image Resolution:	1024 by 768
Image Pixel Size:	0.08 μm
Map Resolution:	256 by 192
Map Pixel Size:	0.31 μm
Acc. Voltage:	20.0 kV
Magnification:	1600

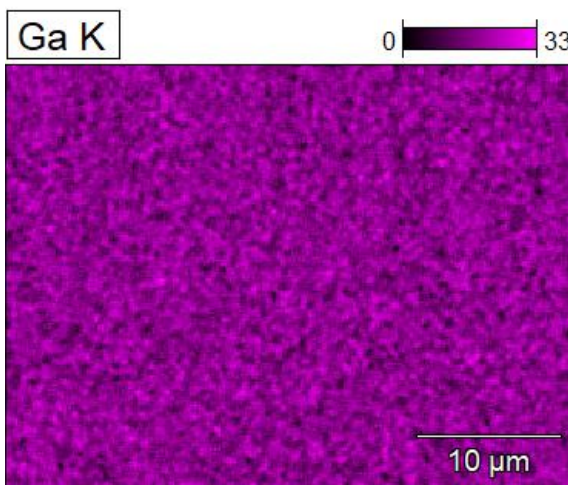
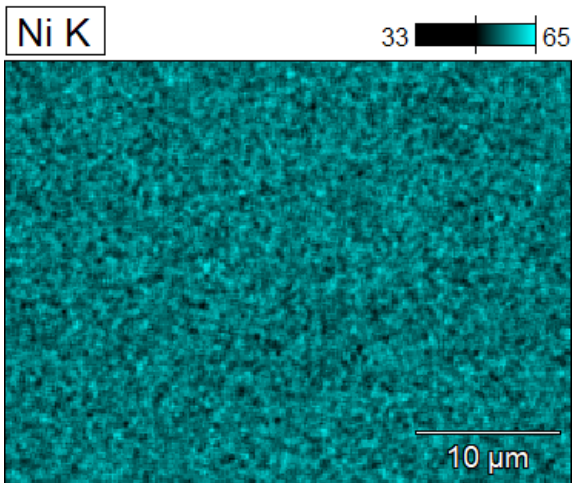
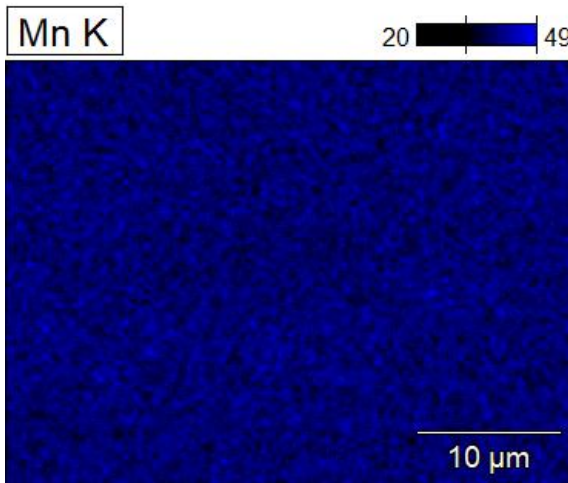


APPENDIX II, 12  
EDS images  
S3AB at 3200x magnification

S3(4)

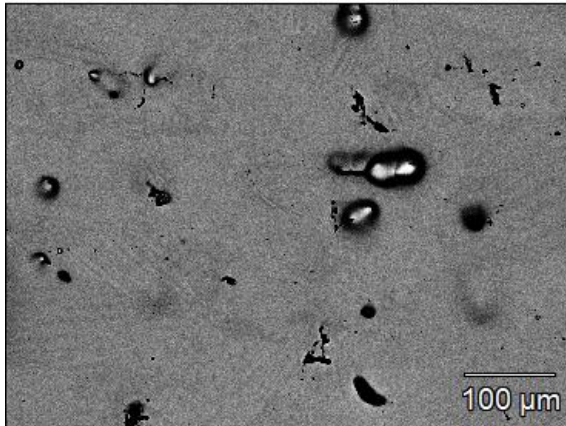


Data Type: Atomic %  
Image Resolution: 1024 by 768  
Image Pixel Size: 0.04 μm  
Map Resolution: 256 by 192  
Map Pixel Size: 0.15 μm  
Acc. Voltage: 20.0 kV  
Magnification: 3200

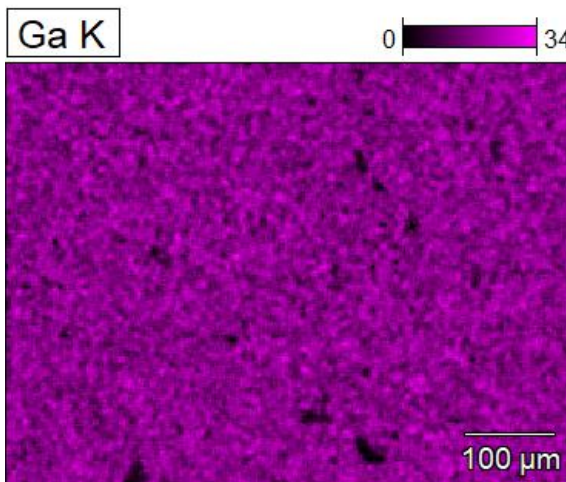
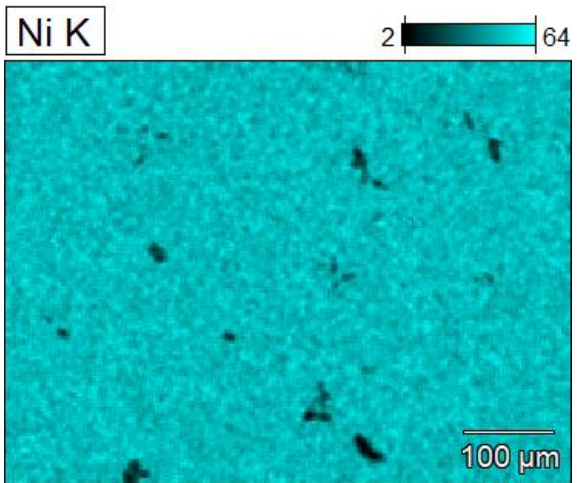
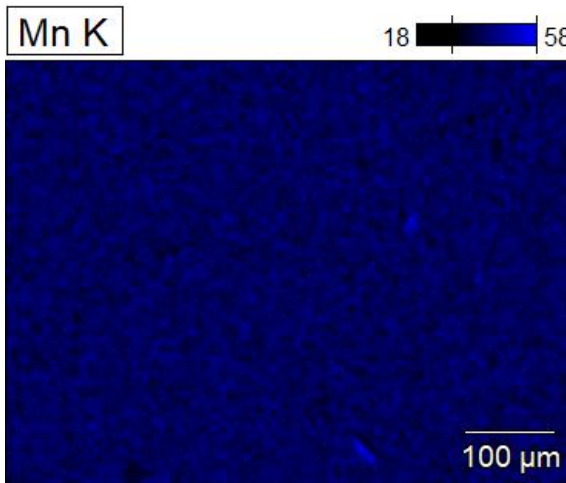


APPENDIX II, 13  
EDS images  
S1HT at 200x magnification

Sample-s1ht(2)

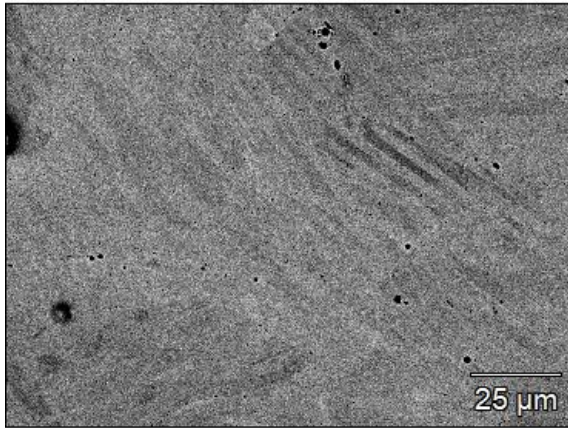


Data Type:	Atomic %
Image Resolution:	1024 by 768
Image Pixel Size:	0.62 μm
Map Resolution:	256 by 192
Map Pixel Size:	2.47 μm
Acc. Voltage:	20.0 kV
Magnification:	200

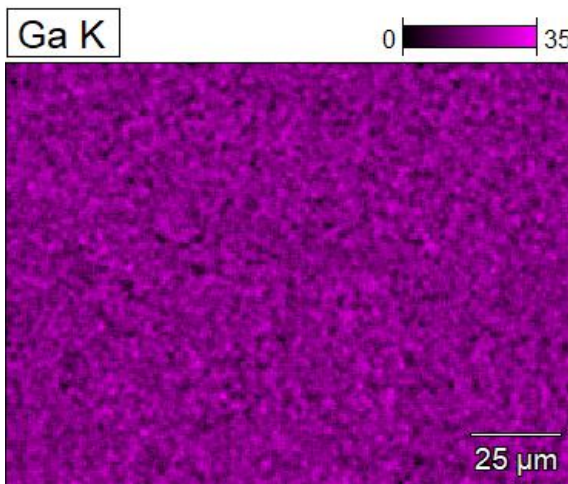
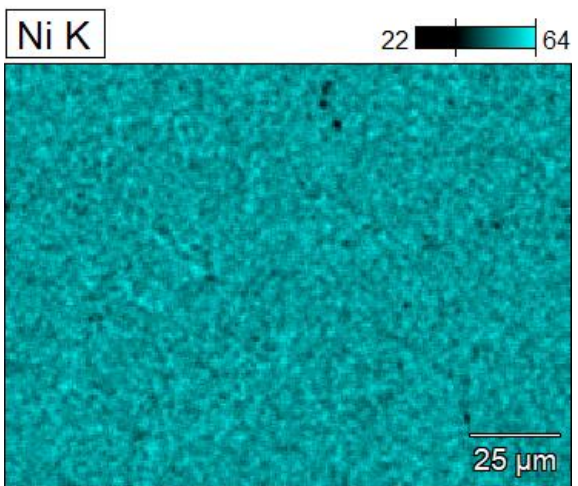
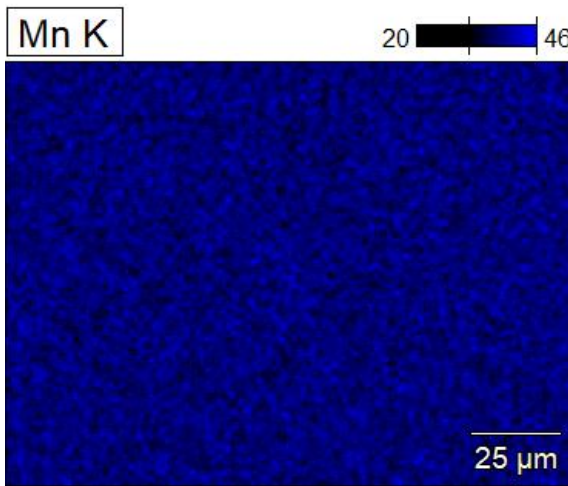


APPENDIX II, 14  
EDS images  
S1HT at 800x magnification

Sample-s1ht(3)

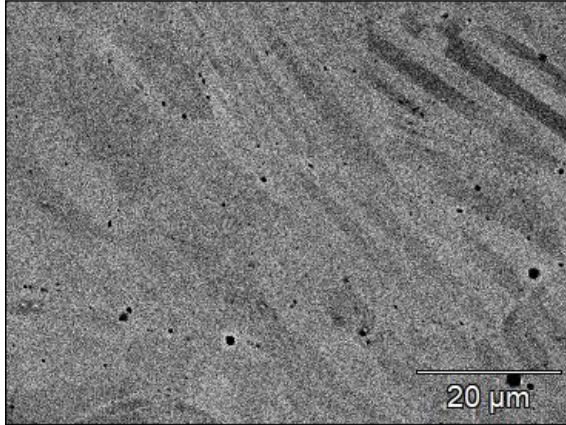


Data Type:	Atomic %
Image Resolution:	1024 by 768
Image Pixel Size:	0.15 μm
Map Resolution:	256 by 192
Map Pixel Size:	0.62 μm
Acc. Voltage:	20.0 kV
Magnification:	800

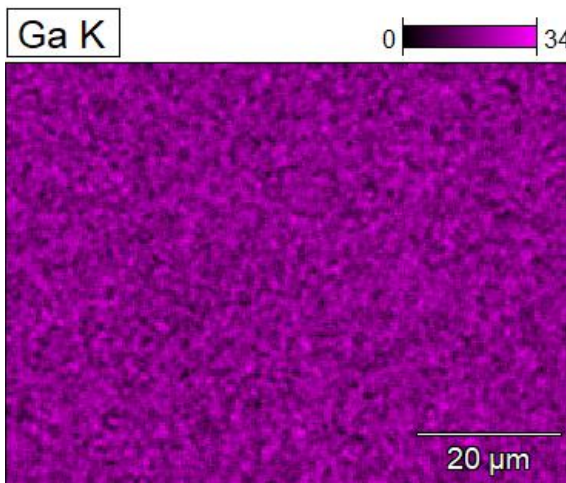
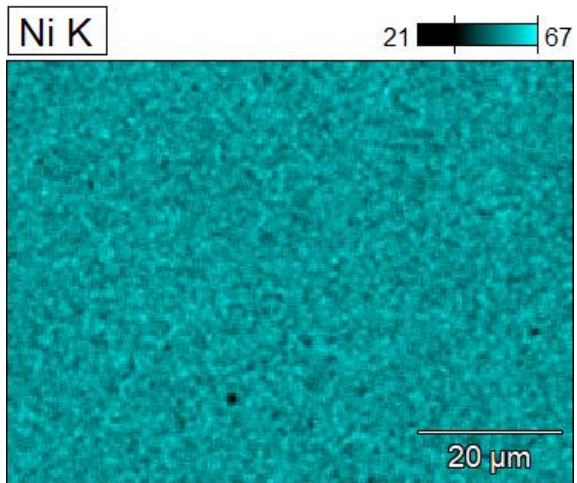
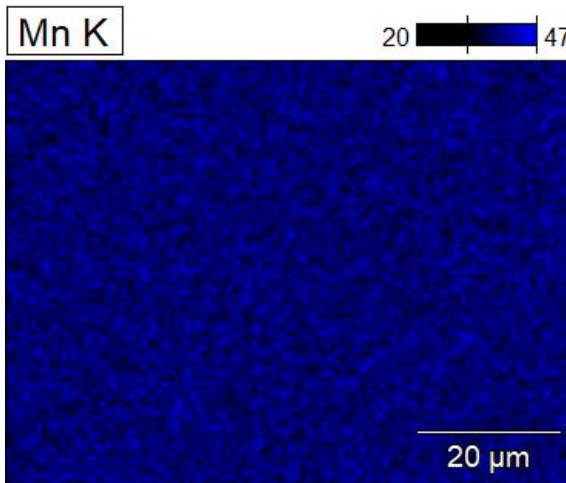


APPENDIX II, 15  
EDS images  
S1HT at 1600x magnification

Sample-s1ht(4)

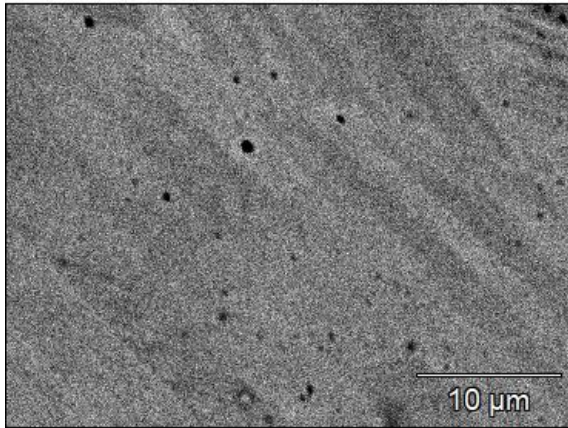


Data Type:	Atomic %
Image Resolution:	1024 by 768
Image Pixel Size:	0.08 μm
Map Resolution:	256 by 192
Map Pixel Size:	0.31 μm
Acc. Voltage:	20.0 kV
Magnification:	1600

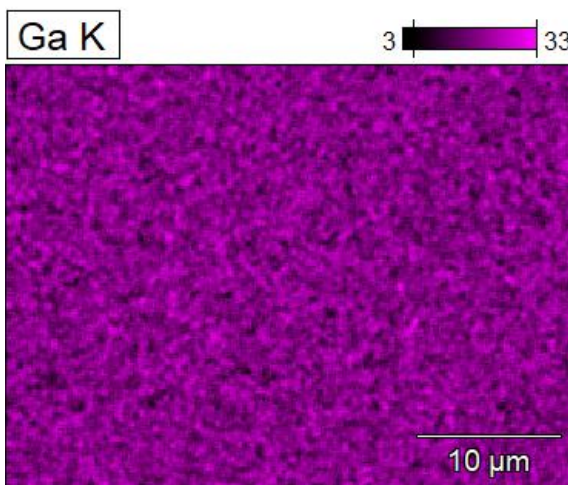
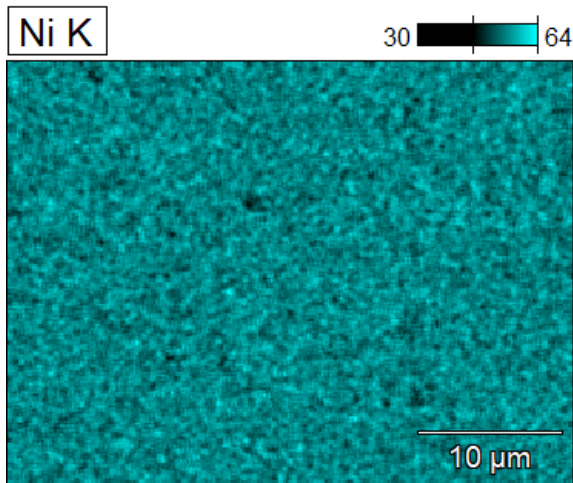
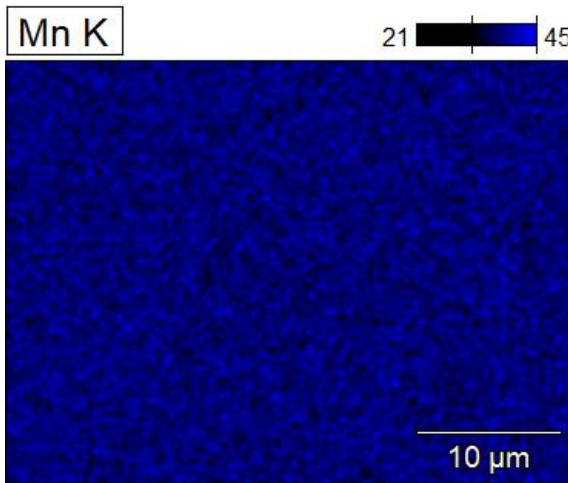


APPENDIX II, 16  
EDS images  
S1HT at 3200x magnification

Sample-s1ht(5)

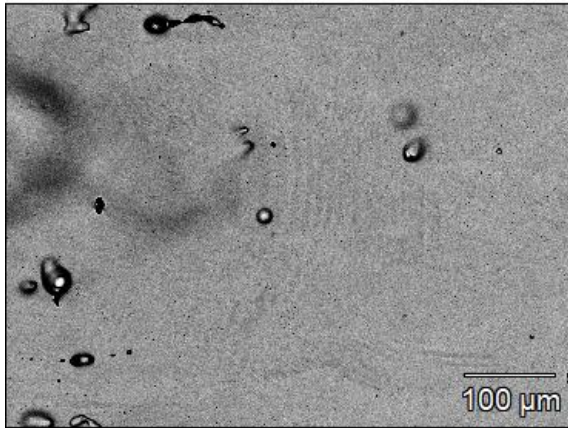


Data Type:	Atomic %
Image Resolution:	1024 by 768
Image Pixel Size:	0.04 µm
Map Resolution:	256 by 192
Map Pixel Size:	0.15 µm
Acc. Voltage:	20.0 kV
Magnification:	3200

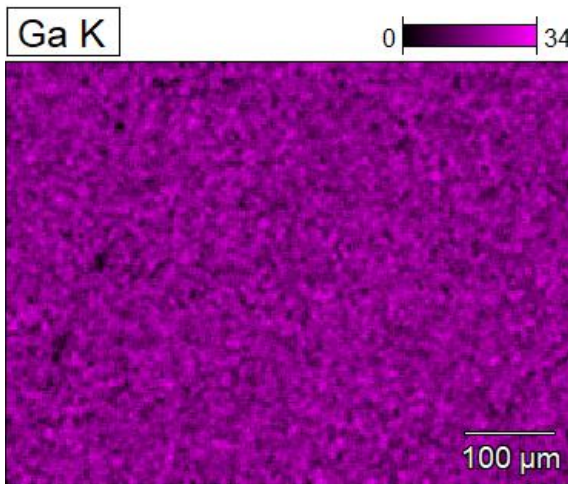
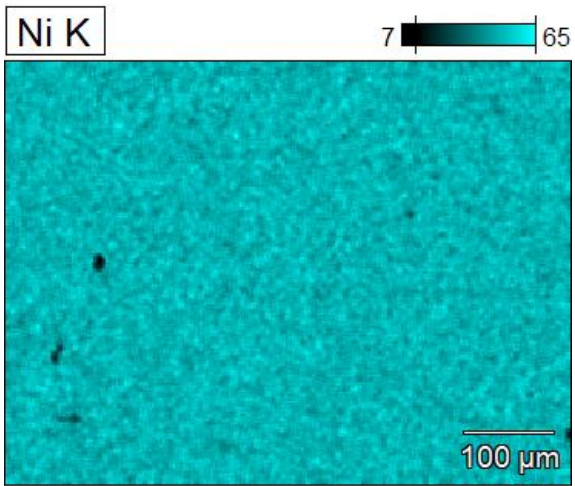
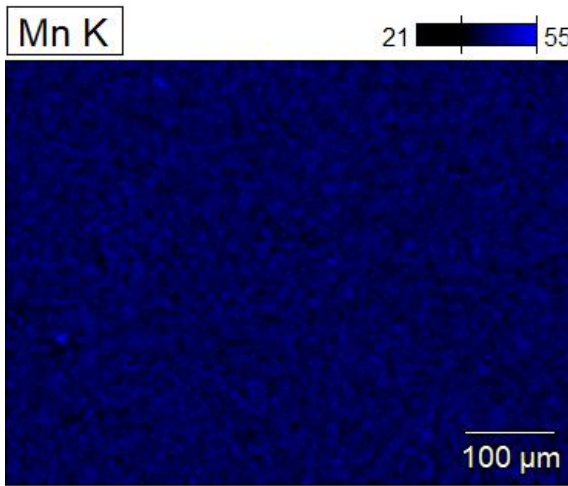


APPENDIX II, 17  
EDS images  
S2HT at 200x magnification

Sample-s2ht(1)

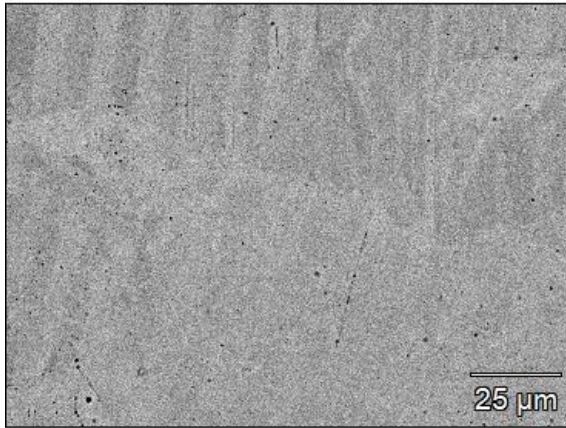


Data Type:	Atomic %
Image Resolution:	1024 by 768
Image Pixel Size:	0.62 μm
Map Resolution:	256 by 192
Map Pixel Size:	2.47 μm
Acc. Voltage:	20.0 kV
Magnification:	200

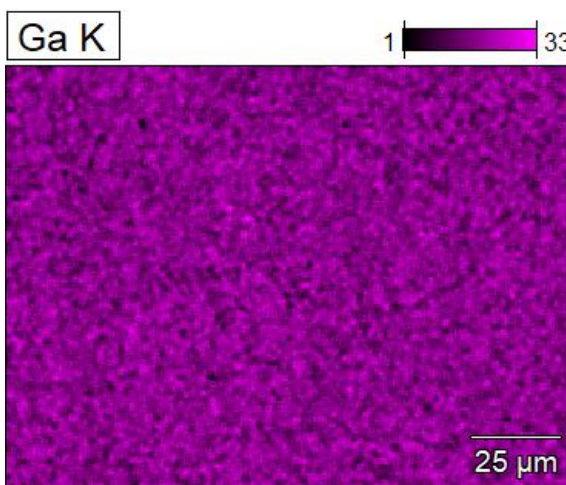
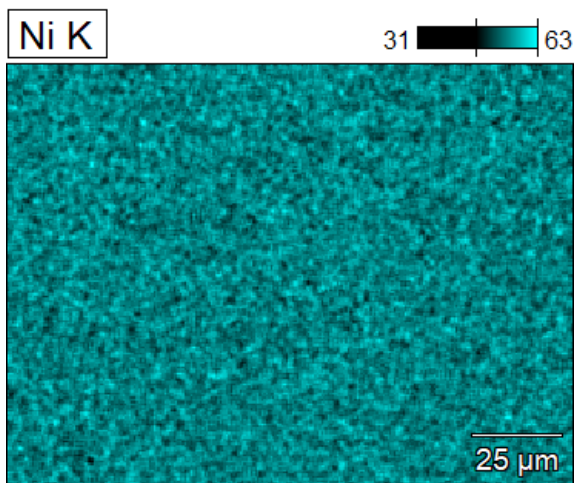
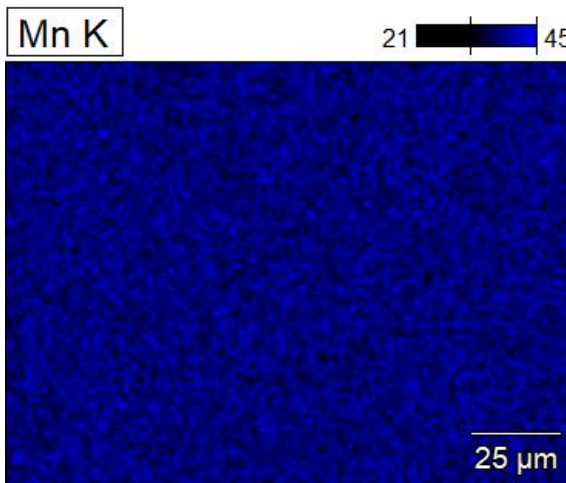


APPENDIX II, 18  
EDS images  
S2HT at 800x magnification

Sample-s2ht(2)

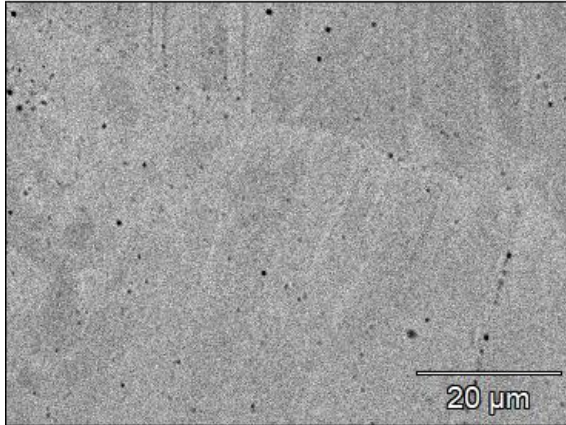


Data Type:	Atomic %
Image Resolution:	1024 by 768
Image Pixel Size:	0.15 μm
Map Resolution:	256 by 192
Map Pixel Size:	0.62 μm
Acc. Voltage:	20.0 kV
Magnification:	800

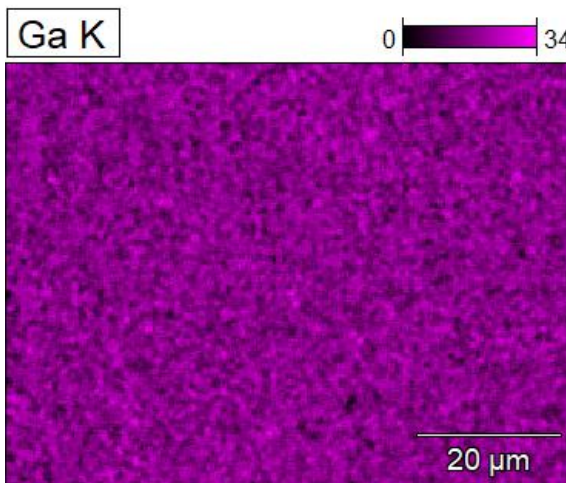
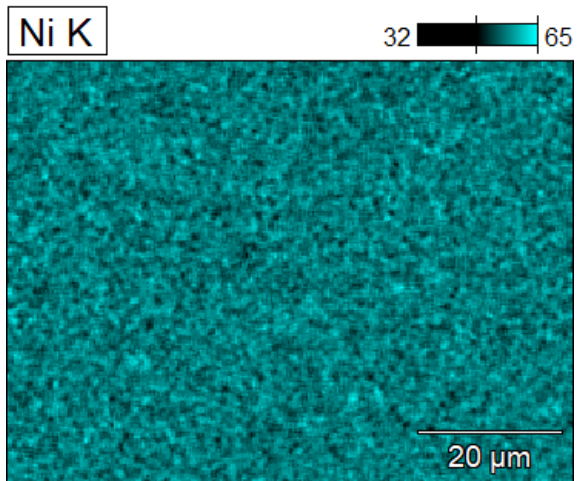
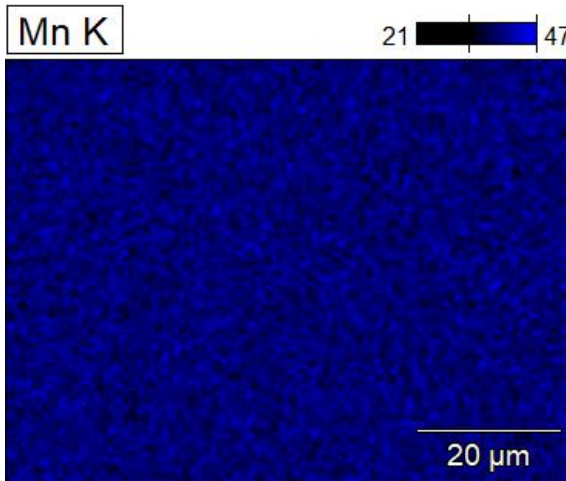


APPENDIX II, 19  
EDS images  
S2HT at 1600x magnification

Sample-s2ht(3)

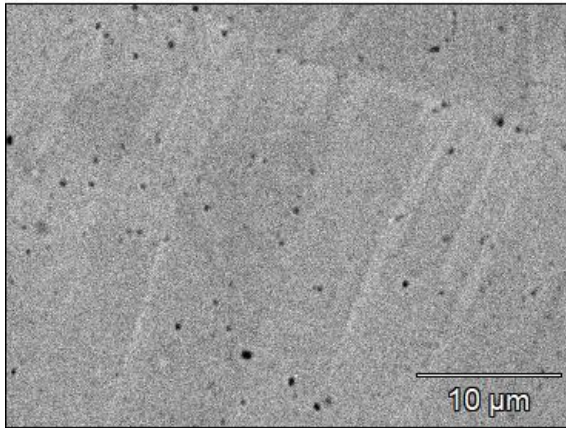


Data Type:	Atomic %
Image Resolution:	1024 by 768
Image Pixel Size:	0.08 µm
Map Resolution:	256 by 192
Map Pixel Size:	0.31 µm
Acc. Voltage:	20.0 kV
Magnification:	1600

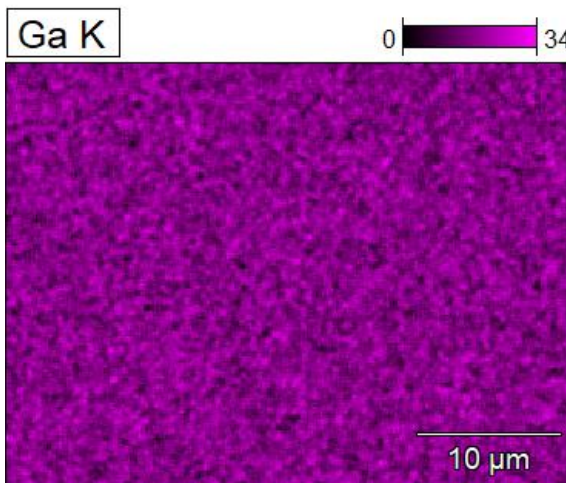
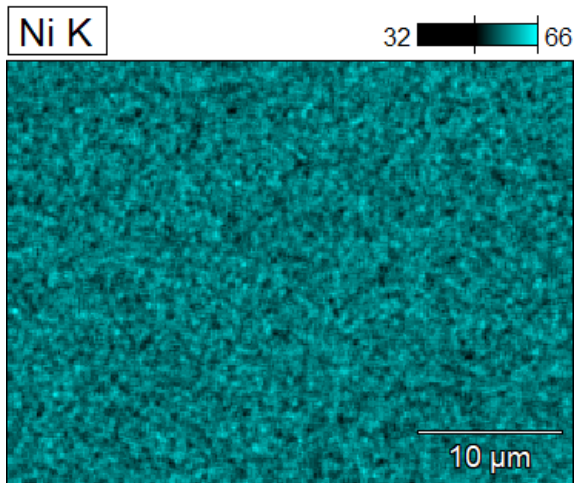
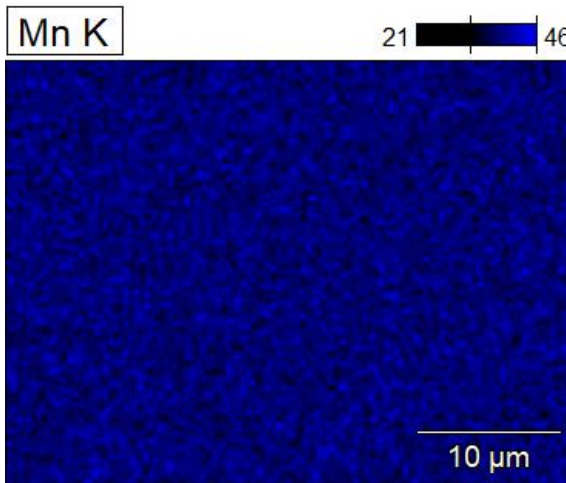


APPENDIX II, 20  
EDS images  
S2HT at 3200x magnification

Sample-s2ht(4)

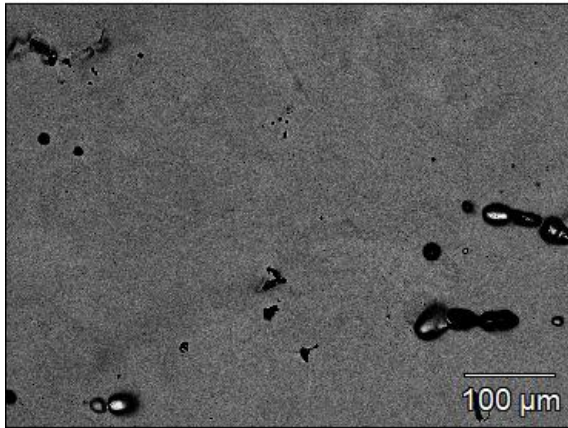


Data Type:	Atomic %
Image Resolution:	1024 by 768
Image Pixel Size:	0.04 μm
Map Resolution:	256 by 192
Map Pixel Size:	0.15 μm
Acc. Voltage:	20.0 kV
Magnification:	3200

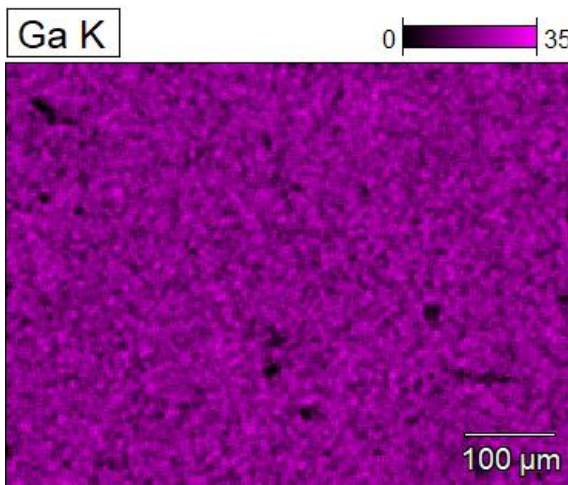
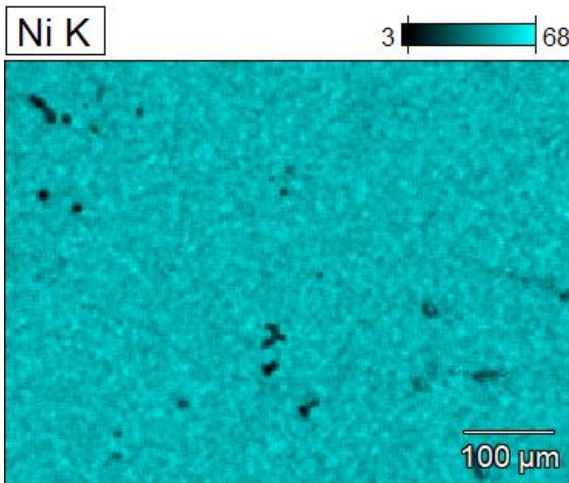
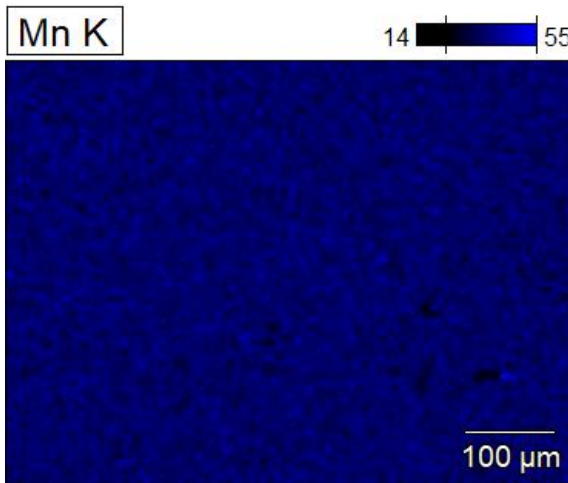


APPENDIX II, 21  
EDS images  
S3HT at 200x magnification

Sample-s3ht(1)

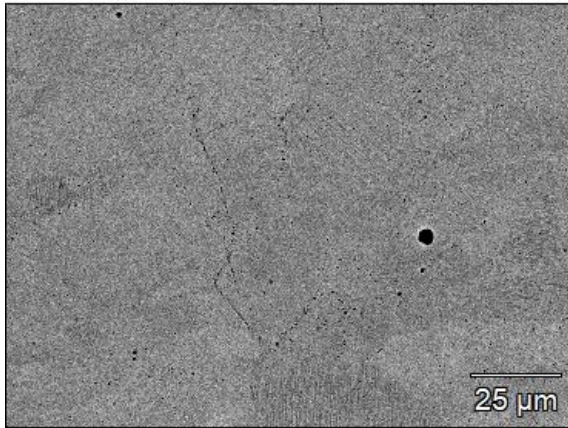


Data Type:	Atomic %
Image Resolution:	1024 by 768
Image Pixel Size:	0.62 μm
Map Resolution:	256 by 192
Map Pixel Size:	2.47 μm
Acc. Voltage:	20.0 kV
Magnification:	200

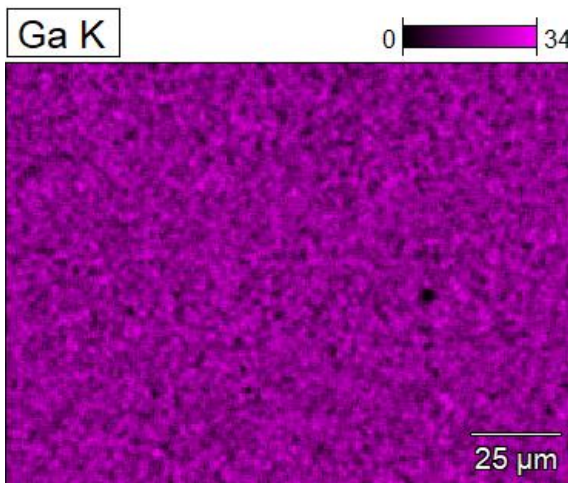
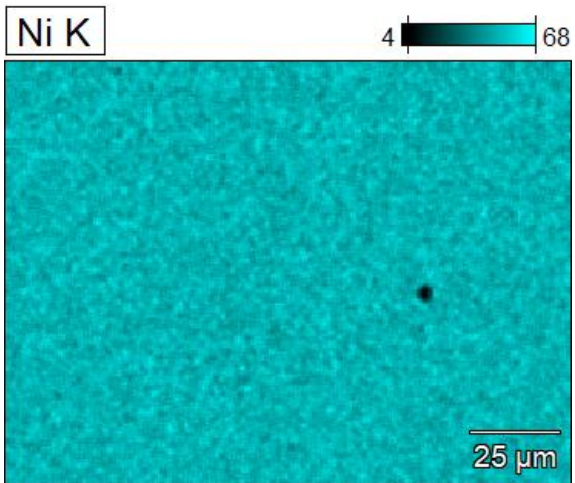
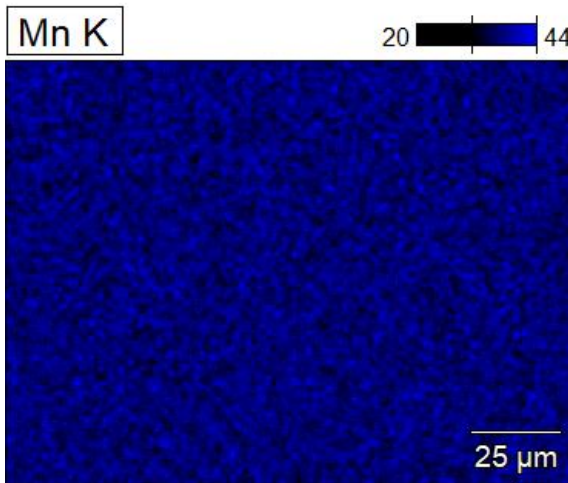


APPENDIX II, 22  
EDS images  
S3HT at 800x magnification

Sample-s3ht(2)

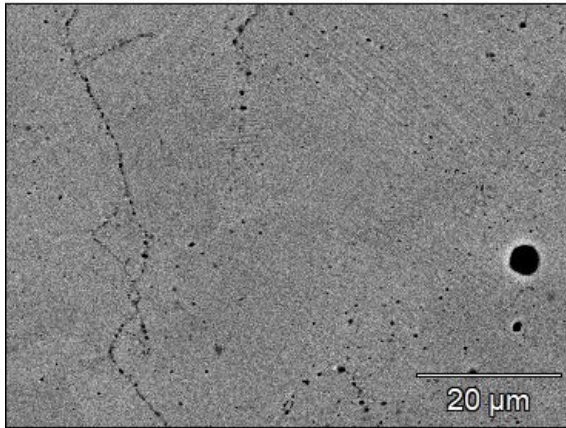


Data Type:	Atomic %
Image Resolution:	1024 by 768
Image Pixel Size:	0.15 μm
Map Resolution:	256 by 192
Map Pixel Size:	0.62 μm
Acc. Voltage:	20.0 kV
Magnification:	800

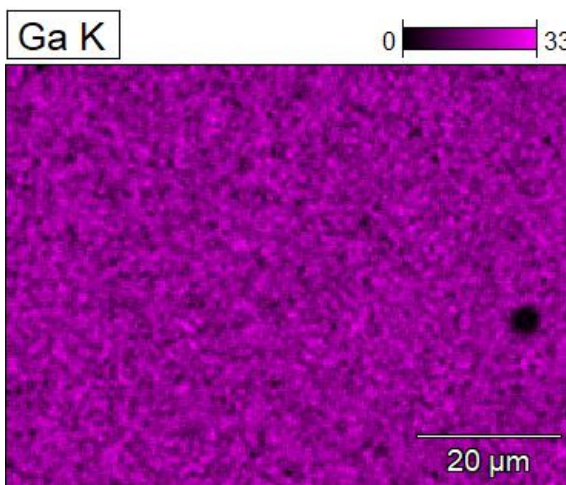
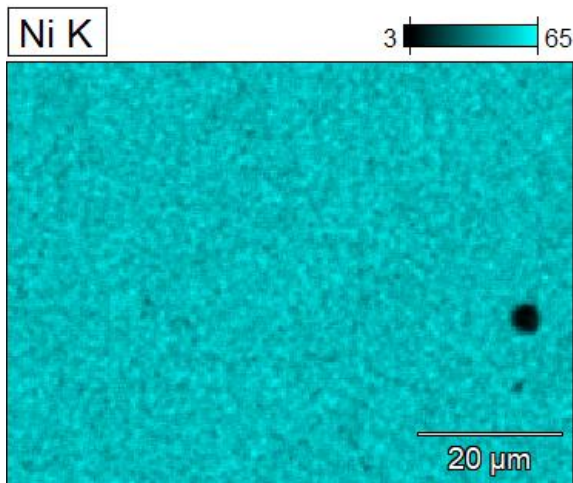
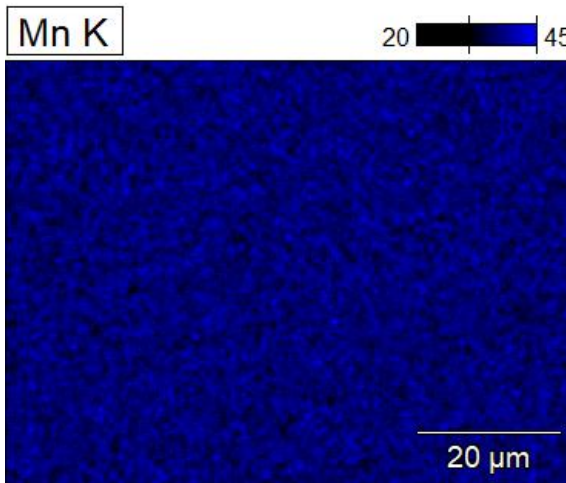


APPENDIX II, 23  
EDS images  
S3HT at 1600x magnification

Sample-s3ht(3)

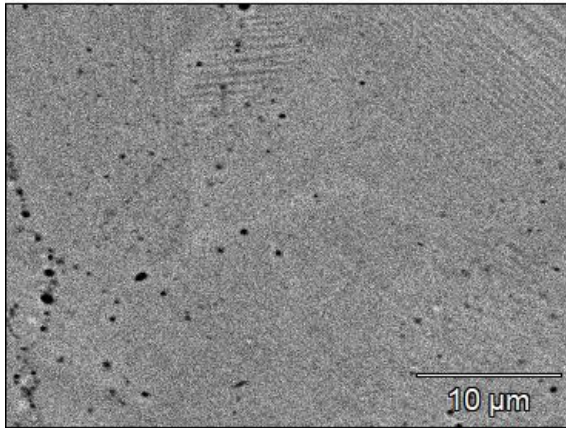


Data Type:	Atomic %
Image Resolution:	1024 by 768
Image Pixel Size:	0.08 μm
Map Resolution:	256 by 192
Map Pixel Size:	0.31 μm
Acc. Voltage:	20.0 kV
Magnification:	1600



APPENDIX II, 24  
EDS images  
S3HT at 3200x magnification

Sample-s3ht(4)



Data Type:	Atomic %
Image Resolution:	1024 by 768
Image Pixel Size:	0.04 μm
Map Resolution:	256 by 192
Map Pixel Size:	0.15 μm
Acc. Voltage:	20.0 kV
Magnification:	3200

